



Advanced Load Alleviation for Wind Turbines using Adaptive Trailing Edge Flaps: Sensing and Control

Andersen, Peter Bjørn; Gaunaa, Mac; Bak, Christian; Buhl, Thomas; Poulsen, Niels Kjølstad

Publication date:
2010

Document Version
Publisher's PDF, also known as Version of record

[Link back to DTU Orbit](#)

Citation (APA):

Andersen, P. B., Gaunaa, M., Bak, C., Buhl, T., & Poulsen, N. K. (2010). Advanced Load Alleviation for Wind Turbines using Adaptive Trailing Edge Flaps: Sensing and Control. Roskilde: Risø National Laboratory for Sustainable Energy. (Risø-PhD; No. 61(EN)).

DTU Library Technical Information Center of Denmark

General rights

Copyright and moral rights for the publications made accessible in the public portal are retained by the authors and/or other copyright owners and it is a condition of accessing publications that users recognise and abide by the legal requirements associated with these rights.

- Users may download and print one copy of any publication from the public portal for the purpose of private study or research.
- You may not further distribute the material or use it for any profit-making activity or commercial gain
- You may freely distribute the URL identifying the publication in the public portal

If you believe that this document breaches copyright please contact us providing details, and we will remove access to the work immediately and investigate your claim.

Advanced Load Alleviation for Wind Turbines using Adaptive Trailing Edge Flaps: Sensing and Control

Risø-PhD-Report

Peter Bjørn Andersen
Risø-PhD-61(EN)
February 2010

Risø DTU
National Laboratory for Sustainable Energy



Author: Peter Bjørn Andersen
Title: Advanced Load Alleviation for Wind Turbines using Adaptive Trailing Edge Flaps: Sensoring and Control
Division: Wind Energy Division

This thesis is submitted in partial fulfillment of the requirements for the Ph.D. degree at The Technical University of Denmark

Abstract (max. 2000 char.):

The purpose of wind turbines and their predecessors the windmill, is to convert the energy in the wind to usable energy forms. Whereas windmills of the past focused on the conversion of wind power to torque for grinding, pumping and winching, modern wind turbines convert the wind energy into electric power. They do so through incorporation of generators, which convert mechanical torque into electricity. Wind turbines are designed to keep the overall cost per produced Kilo Watt hour as low as possible. One way of improving the performance and lifetime of the wind turbine is through active flow control. Active control is often considered costly but if the lifespan of the components can be increased it could be justifiable. This thesis covers various aspects of 'smart control' such as control theory, sensoring, optimization, experiments and numerical modeling.

Risø-PhD-61(EN)
February 2010

ISBN 978-87-550-3824-0

Contract no.:

Group's own reg. no.:
(Føniks PSP-element)

Sponsorship:

Cover :

Pages: 132
Tables:
References:

Information Service Department
Risø National Laboratory for
Sustainable Energy
Technical University of Denmark
P.O.Box 49
DK-4000 Roskilde
Denmark
Telephone +45 46774005
bibl@risoe.dtu.dk
Fax +45 46774013
www.risoe.dtu.dk

ADVANCED LOAD ALLEVIATION FOR WIND TURBINES USING ADAPTIVE TRAILING EDGE FLAPS: SENSING AND CONTROL

PETER BJØRN ANDERSEN

Ph.D. thesis, case number: 274-05-0398

SUPERVISORS: NIELS KJØLSTAD POULSEN^[1], CHRISTIAN BAK^[2], MAC GAUNAA^[3] & THOMAS BUHL^[4]

^[1] ASSOCIATE PROFESSOR @ DTU IMM, MAIN SUPERVISOR

^[2] SENIOR RESEARCHER @ RISØ DTU, WIND ENERGY DIVISION



FEBRUARY 2010

PREFACE

I wish to thank supervisors and censors for review and comments and the Danish Council for Independent Research | Technology and Production Sciences for partly funding my work through the ADAPWING II project. The first ADAPWING I project was sponsored by the Danish Research Council.

The objective of the two ADAPWING projects was through numerical and experimental studies to investigate the potential of using adaptive trailing edge geometries on wind turbine blades for fatigue load alleviation.

Considerable work went into this 2nd edition of the thesis. I wish to thank for all the support and help I got from Christian, Thomas and Mac.

Thank you!

CONTENTS

Preface	ii
Symbol list	vi

CHAPTER 1

1.1 Introduction	1
1.1.1 project goals	1
1.1.2 control of wind turbines	2
1.1.3 organization	4

PART I - THEORY

CHAPTER 2

2.1 A dynamic stall model for trailing edge flaps	7
2.1.1 the inviscid part of the dynamic stall model	7
2.1.2 extending the steady viscous part with a trailing edge flap	10
2.1.3 the dynamic viscous part of the dynamic stall model	12
2.1.4 results and discussion	14
2.1.5 conclusions of the dynamic stall model	16
2.2 Wake modelling	17
2.2.1 near wake model	18
2.2.2 far wake model	24
2.2.3 a note on shed vorticity	27
2.2.4 computational fluid dynamics	27
2.2.5 results wake modelling	28
2.2.6 conclusions wake modelling	32

CHAPTER 3

3.1 Model background	35
3.1.1 the deformable trailing edge flap	35
3.1.2 defining fatigue	35

3.2 Control based on strain measurements.....	36
3.2.1 model.....	36
3.2.2 setup of cases.....	38
3.2.3 results and discussion.....	39
3.2.4 conclusion.....	47
3.3 Control based on inflow measurements	47
3.3.1 model.....	48
3.3.2 setup of cases.....	50
3.3.3 results and discussion.....	50
3.3.4 conclusion.....	54
3.4 Control based on combined sensors.....	54
3.4.1 model.....	55
3.4.2 setup of cases.....	57
3.4.3 results and discussion.....	58
3.4.4 conclusion.....	62
3.5 Using trailing edge flaps to alleviate effects of meandering wakes.....	63
3.5.1 meandering wake model.....	63
3.5.2 setup of cases.....	64
3.5.2.1 controllers.....	64
3.5.2.2 control authority.....	65
3.5.2.3 wind farm topology	66
3.5.2.4 ambient turbulence.....	67
3.5.2.5 flap and sensors.....	67
3.5.3 results and discussion.....	68
3.5.4 conclusion.....	71
3.6 Chapter endnote	72

PART II - EXPERIMENTS

CHAPTER 4

4.1 Pre-described flap motion experiment.....	77
4.1.1 electric model.....	78
4.1.2 testing the electric model	80
4.1.3 wind tunnel turbulence	82
4.1.4 conclusions of the re-examination of the first experiment	83
4.2 Closed loop experiment	84
4.2.1 experimental design	84
4.2.2 pitot tube sensors for control input	87
4.2.3 airfoil pressure tap sensor for control input.....	90
4.2.4 active closed-loop flap control results.....	91
4.2.4.1 the signal filter	92
4.2.4.2 comparison of controllers using different sensor input	94
4.2.4.3 control performance at different incidences	96
4.2.4.4 variable frequency pitch motion	97
4.2.4.5 phase lags in the loop.....	98
4.2.5 conclusions of the second experiment	100

CHAPTER 5

5.1 Conclusion and recommendations	102
Appendix.....	105
A: Gaunaa's shape integrals	106
B: C_M comparison	108
C: Wind tunnel setup drawings and photos	109
D: Strain gauge sensor placement on airfoil.....	112
Bibliography	113
PhD Thesis Summary:.....	120

SYMBOL LIST

Chapter 2.1	Unit	Description
a	-	Non-dimensional position of elastic axis. $a = 2\frac{x_a}{c} - 1$
A_i	-	Profile specific constants for unit response
α	rad	Steady and geometric incidence angle
$\hat{\alpha}$	rad	Contribution from the trailing edge flap to the geometric incidence $\hat{\alpha} = \alpha - \alpha_0(\beta)\hat{f}$
$\acute{\alpha}$	rad	Effective incidence scaled with the unsteady trailing edge separation function \hat{f} in an effort to diminish the flap effect on the induced drag $\acute{\alpha} = \hat{\alpha} - \hat{\alpha}_0(\hat{\beta})\hat{f}$
α_0	rad	Steady geometric zero lift incidence (sum of α_β, α_0^c)
$\hat{\alpha}$	rad	Effective or dynamic incidence including the effect of shed vorticity
α_β	rad	Change in zero-lift incidence angle due to flap deflection
$\hat{\alpha}_0$	rad	Effective or dynamic change in zero-lift incidence angle due to flap deflection
α_0^c	rad	Constant shift at zero lift due to the un-deformed camberline shape
b	m	Half chord length
b_i	-	Profile specific constants for unit response
β	rad	Deformation angle for the deformable trailing edge flap
$\hat{\beta}$	rad	Effective or dynamic deformation angle for the deformable trailing edge flap including the effect of shed vorticity
c	m	Chord length
C_D	-	Drag coefficient
$C_{D,flat_plate}$	-	Pressure drag on a flat plate in a potential Kirchoff flow
$C_{D,dyn}$	-	The dynamic and viscous drag coefficients
$C_{D,ind}$	-	Induced drag coefficient
$C_{D,sep}$	-	Unsteady drag coefficient contribution
C_L	-	Lift coefficient
\tilde{C}_L	-	Steady and fully separated lift coefficient
\hat{C}_L	-	The circulatory part of the effective inviscid lift
$C_{L,dyn}$	-	The dynamic and viscous lift coefficients
C_M	-	Steady viscous moment coefficient
$C_{M,dyn}$	-	The dynamic and viscous moment coefficients
$C_{M,sep}$	-	Unsteady moment coefficient contribution
ΔC_L^*	-	Quasi steady change in the lift coefficient caused by the flap deflection
ΔC_M^*	-	Change in the moment coefficient caused by the flap deflection using a single modeshape
ε	-	Non-dimensional chord position
f	-	Non-dimensional equivalent steady airfoil trailing edge separation point
\hat{f}	-	Dynamic non-dimensional trailing edge separation variable
F_{dydx}		Deformation mode shape integrals, see the work of Gaunaa [29]
F_y		Deformation mode shape integrals, see the work of Gaunaa [29]
G_{dydx}		Deformation mode shape integrals, see the work of Gaunaa [29]
G_y		Deformation mode shape integrals, see the work of Gaunaa [29]

H_{dydx}		Deformation mode shape integrals, see the work of Gaunaa [29]
H_y		Deformation mode shape integrals, see the work of Gaunaa [29]
k	-	Reduced frequency $k=\omega c/(2U)$
o	m	Pressure center moment arm
t	s	Time
t^*	-	Non-dimensional time variable, used for low pass filtering
τ_b	s	Low pass filter time constant used to simulate boundary layer dynamics
τ_p	s	Low pass filter time constant used to simulate a postulated time lag between pressure distribution and lift
U	m/s	The relative velocity free-stream airfoil motion
x	m	Dimensional chord position
x_a	m	Position of elastic axis from LE
y	-	Flap modeshape which is a function of the non-dimensional chord length
$z_{\alpha,i}$	rad	Incidence state variables for the unsteady aerodynamics
$z_{\beta,i}$	rad	Flap deflection state variables for the unsteady aerodynamics
$z_{0,i}$	rad	Incidence shift state variables for the unsteady aerodynamics
ω	rad/s	Actual frequency of the harmonic flap motion

Chapter 2.2 Unit

Description

a	-	Axial induction factor – part of far wake model
a	m	Vortex blade radial evaluation point
A_n	-	Mixing coefficients for the indicial functions – part of far wake model
b_k	-	Indicial function coefficients used to approximate Beddoes equation
B	m	Vortex blade radial trailed point B
c	m	Chord length
c_k	-	Indicial function coefficients used to approximate Beddoes equation
C_L	-	Lift coefficient
c_N	-	Normal force coefficient
C_T	-	Thrust coefficient
$C_{T,fw}$	-	Local thrust coefficient for an annular blade element – part of far wake model
D_w	m/s	Axial downwash contribution
D'_w	m/s	Tangential downwash contribution from the currently generated vortex element
ds	m	Vortex element length
dw	m/s	Induced velocity contribution at point A
dw_0	m/s	Initial downwash value
F	-	Prandtl's blade tip correction factor – part of far wake model
φ	degree	Tilting angle between trailed vorticity plane and rotor plane
Φ	-	Non-dimensional helping variable
Γ	m ² /s	Vortex circulation strength
γ	degree	Angle between the direction normal to the rotor plane and the free stream velocity
h	m	Distance between vortex evaluation point A and vortex trailed point B
k_1, k_2, k_3, k_4	-	Coefficient used to determine the steady axial induction factor – part of far wake model
k_{fw}	-	Far wake load scaling coefficient

$k_{n,0}, k_{n,1}, k_{n,2}$	s	Second order polynomial constants used to calculate the wake time constants for the dynamic far wake model
$l_{1..q}$	-	Coefficients used to approximating the k_{fw} coefficient based on λ and C_T values
λ	-	Tip speed ratio factor
ω	rad/s	Angular velocity of the rotor
Ω	rad	Azimuth angle of blade
r	m	Blade radial coordinate
R	m	Total blade length
τ_n	s	Time constants used to calculate the dynamic far wake
u_B	m/s	Tangential velocities at point B
V_r	m/s	Relative wind velocity at a given radial blade position
V_∞	m/s	Free stream velocity
w	m/s	Dynamic axial downwash from one circular arc element
w'	m/s	Total dynamic tangential induction at a given radial position on the blade
w_B	m/s	Axial velocities at point B
w_{BEM}	m/s	Induced velocity from the far wake model or traditional blade element moment momentum method scaled using the k_{fw} coefficient
w_{NW}	m/s	Induced velocity from the near wake model
Z_k	m/s	State variable used to find dynamic axial downwash for an vortex arc element
Z'_k	m/s	State variable used to find dynamic tangential downwash for an vortex arc element
z_n^k	-	Wake state variables – part of far wake model

Chapter 3.2 Unit

Description

A	m ²	Cross sectional area
A, b	-	Constants used to formulate the system of constraints
β	degree	Trailing edge flap deflection
ε	-	Flapwise blade deflection strain at radial position r_s
ε'	-	First order filtered strain
E	N/m ²	Elastic modulus
EI	Nm ⁴	Bending stiffness
ψ	-	First flapwise deflection shape
h	m	Perpendicular distance to the neutral axis
K_p	degree	Proportional gain for flap control
\tilde{l}_f	-	Normalized flap length
M	Nm	Blade bending moment
M_x^*	Mn	Equivalent blade root moment fatigue load
N	N/m	Normal force at a given blade section
ω	rad/s	Rotor speed
ω_b	Hz	First flapwise eigenfrequency for a blade clamped at the blade root
ω_f	rad/s	Low passed rotor speed
ω_0	rad/s	Rated rotor speed
R	m	Total blade length
\tilde{r}	-	Non-dimensional radial position
r_f	m	Radial blade position of trailing edge flap

r_s	m	Radial blade position of sensor used to control trailing edge flap
σ	N/m ²	Bending stress
τ	s	Time constant for low pass filter
τ_ω	s	Low pass filter time constant for rotor speed signal
x	-	Optimization variable vector
z	-	State function used for low pass filter

Chapter 3.3 Unit

	Unit	Description
α	rad	Incidence angle in flowwise direction
α_0	rad	Constant incidence shift
$\tilde{\alpha}$	rad	Reference incidence angle and point of linearization
β_1	rad	Flap deflection from f_1 controller
β_2	rad	Flap deflection from f_2 controller
c	m	Chord
C_L	-	Lift coefficient, typically for a section of a blade given as $L = 0.5\rho c C_L V^2$
f_1	m ² /s ²	Governing equation for controller 1 based on inflow measurements
f_2	m ² /s ²	Governing equation for controller 2 based on inflow measurements and rotor speed
L	N	Aerodynamic lift force
ρ	Kg/m ³	Density of air
ω	rad/s	Rotor speed
ω_0	rad/s	Rated rotational speed of the rotor
$\tilde{\omega}$	rad/s	Reference rotor speed and point of linearization
r_f	M	Radial position of the center of the flap
τ_i	s	Time constants for w_i ,
V	m/s	Relative measured wind speed
\tilde{V}	m/s	Reference wind speed and point of linearization
w_i	-	First order filtered sensor values; incidence angle, wind speed, rotational speed

Chapter 3.4 Unit

	Unit	Description
C_D	-	Drag coefficient
C_L	-	Lift coefficient
K_α	-	Power optimization coefficient used to track maximum power extraction at constant tip-speed ratio
M	KNm	Blade root moment sensor
ω	rad/s	Rotor rotational speed
ω_{ref}	rad/s	Reference rotational speed

Chapter 4.1		Unit	Description
β	degree		Quasi steady flap deflection
C	mF		Capacitance
E	V/N		Aerodynamic feedback
k_{amp}	A		Amplification factor used by the power amplifier for the trailing edge flaps
K_p	degree/volt		proportional constant
L	Ω/q		Inductance
N	N		Normal force aerodynamic load
q	q		Electric charge
R	Ω		Resistance
U	m/s		Free wind speed in wind tunnel
V_{AMP}	V		Voltage out from amplifier
V_C	V		Capacitor voltage drop
V_{IN}	V		Control voltage

Chapter 4.2		Unit	Description
α	rad		Incidence angle
α_i	rad		Airfoil eigenmotion
c	m		Chord length
C_L	-		Lift coefficient
ϕ	degree		Phase angle
k	-		Reduced frequency
K_P	-		Proportional gain
l	m		Distance from pitch axis to tip of pitot tube
ω	rad/s		Angular frequency
P_∞	Pa		Undisturbed pressure
P_θ	Pa		Pressure at angle θ
ρ	Kg/m^3		Air density
θ	degree		Pitot pressure angle
U	m/s		Wind speed near pitot sensor
V	m/s		Free wind speed

CHAPTER 1

INTRODUCTION AND BACKGROUND

1.1 INTRODUCTION

The purpose of wind turbines and their predecessors the windmill, is to convert the energy in the wind to usable energy forms. Whereas windmills of the past focused on the conversion of wind power to torque for grinding, pumping and winching, modern wind turbines convert the wind energy into electric power. They do so through incorporation of generators, which convert mechanical torque into electricity. Wind turbines are designed to keep the overall cost per produced Kilo Watt hour as low as possible. One way of improving the performance and lifetime of the wind turbine is through active flow control. Active control is often considered costly but if the lifespan of the components can be increased it could be justifiable. This thesis covers various aspects of 'smart control' such as control theory, sensing, optimization, experiments and numerical modeling.

1.1.1 PROJECT GOALS

The overall goal is to investigate the fatigue load reduction potential of the deformable trailing edge flaps on wind turbine blades. The goal is reached through three milestones.

Milestone one aims at enhancing the aerodynamic models to include steady and unsteady flow and viscous effects of the trailing edge flap. In Part I, Chapter 2, a dynamic stall model for trailing edge flaps is described along with a near wake model.

Milestone two contains the formulation of various control strategies for the trailing edge flaps using a range of sensors. In Part I, Chapter 3 several different parameter studies and constrained optimizations are conducted primarily using the five Mega Watt reference turbine also used in the UpWind project¹.

Milestone three is about the conduction of a wind tunnel experiment. In Part II, Chapter 4 the wind tunnel experiments are described and results are presented.

The three milestones should not be regarded separately. The work conducted in each milestone links with the others and has numerous relations to previous work conducted in the field of active control of wind turbines.

¹ SIXTH FRAMEWORK PROGRAMME (FP6), 2009.
Available from Internet <http://www.upwind.eu/> Accessed 17 September 2009.

1.1.2 CONTROL OF WIND TURBINES

All wind turbines are subject to unsteady loads. During normal operation the wind turbine blades will experience fluctuating loads because of the turbulent wind field or the meandering wake deficit from upstream turbines. Alleviating the contribution from unsteady loads can increase component lifetime and maintenance required for the wind turbine.

Recent work has shown that active load reduction using pitch control for Mega Watt size wind turbines can alleviate load increments from yaw errors, wind shear and gusts considerably [1]. The load reduction is realized either by pitching the blades independently (individual pitch) or equally for each blade but with a phase shift between each blade (cyclic pitch). According to Larsen et al [2] a comparison to collective pitch, where all blades are pitched equally, shows that cyclic pitch can reduce the blade flap fatigue loads at the hub 21%, while it can be reduced 25% when using individual pitch. Also extreme load on the turbine can be reduced with up to 3% when using cyclic pitch and 6% when using individual pitch for the blade flap at the hub. This means that there is a significant potential in using advanced pitch control for load reduction. However, as wind turbine blades become larger and more flexible there is an increased need for locally distributed control surfaces which will reduce the requirement for the pitch bearings and reduce the time from actuations to load change. Different devices can be used for local active control.

SIGNIFICANT CONTRIBUTIONS FOR SMART ROTORS

This brings us to the scope of this thesis, which is an investigation into the field of the so called **smart rotors**. The smart rotor concept can refer to many types of active devices such as synthetic jets [3] which are used to reattach a separated boundary layer, microtabs [4] effectively altering the airfoil camber. Both tabs and flaps were investigated at **U.C. Davis** [5].

Ailerons were used by the American National Renewable Energy Laboratory, **NREL**, on a full scale turbine for aerodynamic breaking and load control [6]. By using the ailerons it was possible give the wind turbine smoother loads and power output curves. An experiment with microflaps, which is a rigid trailing edge that can rotate 90° in both directions, was carried out [7].

Other types of actuators have been tested like the active vortex generators which were mounted on airfoil surfaces to mix and mitigate the separation of the boundary layer [8]. Plasma actuators have been used to delay stall [9].

The use of deformable trailing edge flaps was chosen at **Risø-DTU** because of performance and the reason of low noise emissions. In fact, Risø-DTU has investigated the adaptive trailing edge flap concept since 2003 as means for reducing fatigue loads on wind turbines. A 2D potential-flow solver was modified to investigate the aeroelastic response of an elastically hinged airfoil undergoing unsteady movement in a turbulent flow field [10] and CFD computations [11] was used in the study of a Risø-B1-18 airfoil equipped with differently shaped adaptive trailing edge devices. Piezoelectric benders were experimentally investigated for a Risø-B1-18 airfoil section [12]. The first detailed evaluations of the load reduction capability were conducted through aeroelastic simulations using a 2D

aero-spring-damper-elastic setup described in the work of Buhl et al [13]. New concepts, models and experiments were developed through the ADAPWING¹ & 2 projects [14]. A new collaborative project involving Risø DTU, DTU and Vestas Wind Systems A/S with support from the Danish National Advanced Technology Foundation³ has recently been started. The aim of this project is to demonstrate the feasibility of flaps implemented on full scale wind turbine blades. A Vestas V27 turbine equipped with sensors will as part of that project be the first full scale turbine with deformable trailing edge flaps based on piezoelectric benders. Risø-DTU has developed and performed experiments with a rubber trailing edge flap which deflects when hydraulic/pneumatic pressure is applied [15]. This concept offers a range of solution to practical problems such as robustness, economies and control authority.

Delft University of Technology also focuses on smart rotor designs for wind turbines. In the work of Barlas & Kuik [16] results from a closed loop experiment using the piezoelectric benders shows fatigue load reductions well above 80% in some cases. Also an individual pitch control has been compared to the use of deformable trailing edge flaps in the work of Lackner & Kuik [17]. And extreme loads have been investigated in the work by Matthew & Kuik [18]. Subspace identification of multiple input multiple output linear systems has been proposed by Wingerden [19]. Furthermore, wind tunnel experiments using a down scaled wind turbine equipped with trailing edge flaps was carried out by Delft.

National Technical University of Athens, **NTUA**, has investigated the aeroelastic effect of a trailing edge flaps using an inviscid panel method coupled with a vortex particle approximation of the wake while adding viscous effects through integral boundary layer equations by Voutsinas & Riziotis [20].

THE DEFORMABLE TRAILING EDGE FLAP

From all of the types of smart controllers mentioned in this section the deformable trailing edge flap will be used. The history of the flap dates back many years. Flaps on a modern airplane wing are typically located near the main fuselage. During landing, flaps are extended allowing more lift with the penalty of additional drag. This allows for slower speeds without stalling. Drag is generally speaking undesirable for wind turbines as it diminishes the power production. The time it takes to deploy 'a flap' on an airplane wing is typically too long for alleviating unsteady loads caused by turbulence and periodic excitation on a wind turbine. The 'aileron' on an airplane wing is more related to the 'flap' on the wind turbine. The term 'deformable trailing edge flap' is used throughout this work in an effort to avoid confusion with the 'flap' on an airplane wing. The deformable trailing edge flap deviates from the airplane flap in many ways. E.g. not being rigid and having edges which have been designed for low noise emission.

² ADAPWING. ADAPtive WING geometry for reduction of wind turbine loads.

³ in Danish; Højteknologifonden

1.1.3 ORGANIZATION

The thesis is organized around a model theory Part I and an experimental Part II. There are five chapters starting with this introduction and each chapter and the appendix contains a number of sections. Part I consists of Chapter 2 and 3. Part II is Chapter 4.

Chapter 2.1 introduces extracts of a **dynamic stall model** for the flap otherwise to be found in the journal paper by Andersen et al [21]. Chapter 2.2 introduces a **near wake model** to be presented at the European Wind Energy Conference and Exhibits (EWEC) 2010 in April in Poland.

Chapter 3.2 introduces extract of a **closed loop controller** for the flaps otherwise described in the journal paper by Andersen et al [22].

Chapter 4.1 reuses the **wind tunnel experiment** described by Bak et al [12]. Chapter 4.2 presents results from the closed loop wind tunnel experiment otherwise described in detail by Andersen et al [23].

Chapter 5 presents the conclusion and final remarks.

PART I - THEORY

CHAPTER 2

AERODYNAMIC MODELS

Numerous models for wind turbines exist. Large systems can be broken into a number of sub-models, where each sub-model has a specific task to do. Some models only correct data. Like the model which corrects 2D airfoil characteristics measured in wind tunnel tests by Bak et al [24]. The accuracy is low on the inboard part of the rotor if 2D airfoil data is applied as the inboard part of the blade is subject to a strong radial flow due to centrifugal pumping of the flow in the stalled regions. One of the main effects of this is that it lowers the pressure in these zones resulting in increased lift and drag. The shape of the airfoil is part of the 3D correction and is used to correct the difference in pressures from 2D to 3D.

The overall goal of this thesis is to investigate the fatigue load reduction potential when applying the deformable trailing edge flap to wind turbines. When using the flap the local pressure distribution will be altered, as shown in Figure 1, sub-models combined with aeroservoelastic tools will capture these effects. Two different aerodynamic models will be described in this chapter. The aeroservoelastic tool HAWC2 [25] is extended with these two models.

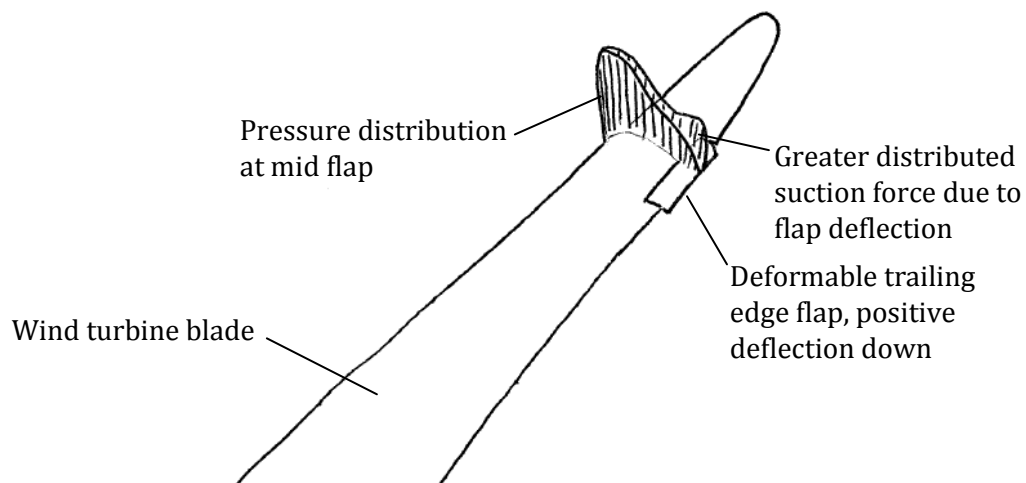


FIGURE 1 ILLUSTRATION OF THE PRESSURE DISTRIBUTION AFFECTED BY A POSITIVE DEFLECTED DEFORMABLE TRAILING EDGE FLAP.

Section 2.1 describes a dynamic stall model by Andersen et al [21]. The primary purpose of the dynamic stall model is to model the 2D unsteady aerodynamic effects of a deformable trailing edge flap.

Section 2.2 describes a Near Wake model by Andersen et al [26]. The near wake model takes into account 3D dynamic effects. The Near Wake model can also be used to investigate dynamic effects not related to a deformable trailing edge flap.

2.1 A DYNAMIC STALL MODEL FOR TRAILING EDGE FLAPS

Unsteady airfoil aerodynamics has been studied experimentally and theoretically from the dawn of flight. An unsteady aerodynamic model is used to describe the unsteady aerodynamic forces on an airfoil undergoing motion in a steady or unsteady flow. Theodorsen's [27] potential flow approximation to the unsteady lift and pitching moment formed the basis for flutter and unsteady airload analysis for fixed wing aircraft operating below stall in the attached flow region. It is important to mention that the theory of classical unsteady airfoil aerodynamics is not the full story. Other factors like viscous effects, surface contamination [28] are also important. All previous work investigating active load reduction using deformable trailing edge flaps carried out at Risø National Laboratory prior to 2005 employed the aerodynamic model of Gaunaa [29], which is an inviscid model, following the tradition of thin airfoil theory but with enhancements like modal expanded and deformable camberlines, drag, flowwise motion, generalized force representations. Gaunaa's work can be considered a generalized version of Theodorsen's theory. Therefore, the investigation was confined to angles of attack in the linear region, where the effect of stall is not present. Due to the great load reduction potential revealed previously, further investigations closer to and somewhat into the stalled region was needed. The dynamic stall model for trailing edge flaps presented here can be considered a modified version of the dynamic stall model of Hansen et al [30] with the static and dynamic effect of deformable trailing edge flap added. This type of dynamic stall model was originally proposed by Beddoes & Leishman [31]. The model predicts the unsteady aerodynamic forces and moments on an airfoil section undergoing arbitrary motion in heave, lead-lag, pitch and trailing edge flapping, and includes the effect of shed vorticity from the trailing edge and the effect of an instationary trailing edge separation point. In the linear region, the model reduces to the inviscid model of Gaunaa. Therefore, the proposed model can be considered a crossover between the work of Gaunaa for the attached flow region and Hansen et al for the separated flow region and will make the aerodynamic forces a function of angle of attack and deflection of the flap. The model was compared with the Velux wind tunnel measurements by Bak et al [12].

The dynamic stall model consists of two parts; an inviscid and a viscous part.

2.1.1 THE INVISCID PART OF THE DYNAMIC STALL MODEL

The usual 2D potential-flow assumption of incompressible, irrotational, inviscid fluid is in effect in this part of the model. Physically this corresponds to very high Reynolds numbers, low mach-numbers and small angles of attack in real life. In this work the usual thin-airfoil approach is adopted. This means that the airfoil is represented by its camberline only, and the thickness of the airfoil is neglected. In the work of Theodorsen [27] and Gaunaa [29] the forces are split between forces caused by position and motion of the airfoil and forces from the velocity induced by the unsteady wake or simply 'non-circulatory' and 'circulatory' terms, respectively. Some of these terms will be described in the following with special focus on the effect of the trailing edge flap.

The unsteady effect of vortex shedding due to changes in circulation on the airfoil is derived analytically by assuming that the airfoil is represented by its camberline only, and that the vortex wake travels with the free-stream velocity in a straight line behind the airfoil.

Deflecting the deformable trailing edge flap an angle β will cause an increase in lift, which can be converted to a mathematical term which can be considered an equivalent flat plate geometric incidence α_β . From classic theory the quasi steady change in the lift coefficient ΔC_L^* caused by the flap deflection can be written up in the following form

$$\Delta C_L^* = 2\pi\alpha_\beta \quad (1)$$

The unsteady trailing edge flap deflection shape can be expressed through a series camberline modeshapes which, when superposed, gives the unsteady shape of the thin airfoil. The piezoelectric bender used in the experiments, Chapter 4, can be modeled using a single modeshape, shown in the lower part of Figure 2.

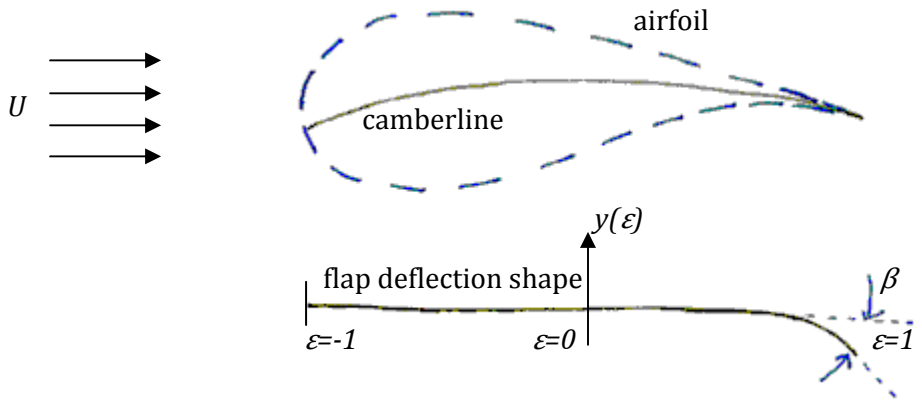


FIGURE 2 (UP) FIRST MODESHAPE: THE CHORDLINE. THE OUTER AIRFOIL SHAPE IS ALSO ILLUSTRATED (DOWN) SECOND MODESHAPE: THE TRAILING EDGE FLAP DEFLECTION SHAPE.

U is free stream velocity. The flap modeshape y is a function of the non-dimensional chord length ε . The change in lift can be rewritten as

$$2\pi\alpha_\beta = 2 \int_{-1}^1 \frac{\partial y}{\partial x} \frac{\sqrt{1-\varepsilon^2}}{\varepsilon-1} d\varepsilon \beta + 2 \int_{-1}^1 \frac{y\sqrt{1-\varepsilon^2}}{\varepsilon-1} d\varepsilon \frac{1}{U} \frac{\partial \beta}{\partial t} = -H_{dydx}\beta - H_y \frac{1}{U} \frac{\partial \beta}{\partial t} \quad (2)$$

please refer to the work of Gaunaa [29] for more detail. The unsteady aerodynamics caused by shedding of eddies into the wake from the airfoil, sometimes referred to as shed vorticity, can be approximated using the superposition principle of Duhamel described by Karman & Sears [32] for series of linear first order step responses. The term effective incidence evaluated in the $\frac{3}{4}$ chord point $\hat{\alpha}$ is used when the physical phenomenon of shed vorticity is expressed mathematically, where the hat $\hat{\ }^$ indicate the dynamic or effective counterpart to the geometric variable without the hat.

$$\begin{bmatrix} \hat{\alpha} \\ \hat{\beta} \\ \hat{\alpha}_0 \end{bmatrix} = \begin{bmatrix} \alpha \\ \beta \\ -\alpha_\beta \end{bmatrix} \left(1 - \sum_i A_i \right) + \sum_i \begin{bmatrix} z_{\alpha,i} \\ z_{\beta,i} \\ z_{0,i} \end{bmatrix} + \begin{bmatrix} 0 \\ 0 \\ \alpha_0^c \end{bmatrix} \quad (3)$$

The lagged flap deflection variable $\hat{\beta}$ should be regarded as a helping variable used when performing table lookups. The last term α_0^c represents the constant zero lift angle due to the camberline shape of the un-deformed airfoil. Deflecting the deformable trailing edge flap alters the airfoil camberline, see Figure 5. The unsteady camberline is expressed through a series of mode shapes and the effective zero lift incidence shift variable is $\hat{\alpha}_0$. The zero lift incidence is

$$\alpha_0 = -\alpha_\beta + \alpha_0^c \quad (4)$$

The z_α , z_β and z_0 are each represented by i state variables for the unsteady aerodynamics. Each of these state variables can be regarded as first order low frequency pass filters using a cutoff corner frequency expressed through the non-dimensional time variable t^*

$$\frac{t^*}{b_i} \begin{bmatrix} \frac{\partial z_{\alpha,i}}{\partial t} \\ \frac{\partial z_{\beta,i}}{\partial t} \\ \frac{\partial z_{0,i}}{\partial t} \end{bmatrix} + \begin{bmatrix} z_{\alpha,i} \\ z_{\beta,i} \\ z_{0,i} \end{bmatrix} = A_i \begin{bmatrix} \alpha \\ \beta \\ -\alpha_\beta \end{bmatrix} \quad (5)$$

$$t^* = \frac{c}{2 \int_0^t U dt} \quad (6)$$

The constants A_i and b_i are profile specific constants, common practice is to use the flat plate response approximation of Jones [33]. The circulatory effective and inviscid lift \hat{C}_L can now be found as

$$\hat{C}_L = 2\pi(\hat{\alpha} - \hat{\alpha}_0) \quad (7)$$

where the contribution from the trailing edge flap is part of the dynamic zero lift incidence offset. Combining the circulatory and non-circulatory lift terms, while maintaining the local blade coordinate system yields

$$C_L = \hat{C}_L + 2\pi \frac{c}{4} \frac{\partial \alpha}{\partial t} \quad (8)$$

higher order terms are neglected and the chord length is c . The induction from the shed wake the unsteady lift angle, here referred to as the effective incidence shifts away from the geometrical incidence at unsteady conditions. This bias in incidences is used to formulate the unsteady lift. However, for the unsteady drag the difference in geometric and effective incidence causes what is known as induced drag. The induced drag is therefore an unsteady phenomenon only. Assuming small angles the induced drag is given by

$$C_{D,ind} = (\alpha - \alpha_0 - \hat{\alpha} + \hat{\alpha}_0)\hat{C}_L \quad (9)$$

A series of user-defined deflection shape integrals are used to calculate the non-circulatory terms, they depend on the shape of the camberline and the flap and they can be calculated prior to the simulation for faster performance. The change in the moment coefficient ΔC_M^* caused by the flap deflection using a single modeshape can be written up in the following form

$$\Delta C_M^* = \beta q_0 + \frac{\partial \beta}{\partial t} q_1 + \frac{\partial^2 \beta}{\partial t^2} q_2 \quad (10)$$

$$q_0 = \frac{1}{2} \left(\frac{F_{dydx}}{\pi} + \frac{H_{dydx}}{2} \right) \quad (11)$$

$$q_1 = \frac{-b}{2\pi U} \left(G_{dydx} + \frac{F_{dydx}}{2} \right) + \frac{1}{2U} \left(\frac{F_y}{\pi} + \frac{H_y}{2} \right) \quad (12)$$

$$q_2 = \frac{b}{\pi U^2} \left(-G_y - \frac{F_y}{2} \right) \quad (13)$$

Please refer to Appendix A for definitions of F , H and G deformation shape integrals. Equation (10) differs from the original work by Andersen et al [21]. The original equation contained more terms some of which were incorrect and some which could easily be neglected. It should however be noted that the change in the moment coefficient was underestimated when using the original formulation of Equation (10) together with the original deformation shape integrals, see Figure B.1 in Appendix B. It should also be noted that the results presented in this thesis never used the original shape integrals as they were scaled to fit the experimental results from the Velux wind tunnel, see Figure B.2 in Appendix B.

2.1.2 EXTENDING THE STEADY VISCOUS PART WITH A TRAILING EDGE FLAP

The 2π lift slope from Equation (2) is replaced by $\partial C_L / \partial \alpha$ and how much the lift change when deflecting the trailing edge flap $-H_{dydx} = \partial C_L / \partial \beta$

$$\alpha_0 = -\alpha_\beta + \alpha_0^c = -\frac{\frac{\partial C_L}{\partial \beta}}{\frac{\partial C_L}{\partial \alpha} \Big|_{\beta=0}} \beta + \frac{H_y}{U} \frac{1}{\partial t} \frac{\partial \beta}{\partial t} + \alpha_0^c \quad (14)$$

Equation (8) expressed in terms of profile specific slopes

$$C_L = \left. \frac{\partial C_L}{\partial \alpha} \right|_{\beta=0} (\hat{\alpha} - \hat{\alpha}_0) + \pi \frac{c}{2} \frac{\partial \alpha}{U} \quad (15)$$

where the 2π from Equation (7) is replaced by the attached flow lift gradient and the unsteady zero lift incidence $\hat{\alpha}_0$ is a function of the flap deflection angle and time.

The viscous flow effects are dominant when the flow around the airfoil starts separating. The static flat plate lift [34] is extended to include the effect of a deformable trailing edge flap.

$$C_L(\alpha, \beta) = \left. \frac{\partial C_L}{\partial \alpha} \right|_{\beta=0} \left(\frac{1 + \sqrt{f(\alpha, \beta)}}{2} \right)^2 [\alpha - \alpha_0] \quad (16)$$

The extended Kirchoff's flow equation has an equivalent steady airfoil trailing edge separation point f , which is a function of the incidence and the trailing edge flap deflection, the left side of the equation containing the stationary viscous $C_L(\alpha, \beta)$ is no longer a line but a surface. The traditional Beddoes-Leishman step-by-step procedure is still valid for estimating lift and separation functions

- 1) Obtain the steady viscous C_L surface from measurements or computational fluid dynamics
- 2) Calculate the fully attached lift slope by locating the linear part of the viscous $C_L(\alpha, \beta=0)$
- 3) Calculate the steady trailing edge separation f surface
- 4) Calculate the steady \tilde{C}_L fully separated surface (using the two next equations)

$$\tilde{C}_L(\alpha, \beta) = \frac{C_L(\alpha, \beta) - \left. \frac{\partial C_L}{\partial \alpha} \right|_{\beta=0} (\alpha - \alpha_0(\beta)) f(\alpha, \beta)}{1 - f(\alpha, \beta)}, \quad f \neq 1 \quad (17)$$

$$\tilde{C}_L(\alpha, \beta) = \frac{C_L(\alpha, \beta)}{2}, \quad f = 1 \quad (18)$$

The separation function f will be used to interpolate between the fully separated and attached lift in order to find the unsteady and sometimes partially separated lift, for more information please refer to Andersen et al [21]. A typical separated lift slope is illustrated in Figure 3 along with the separation function and fully attached lift slope all function of the trailing edge deformation angle β .

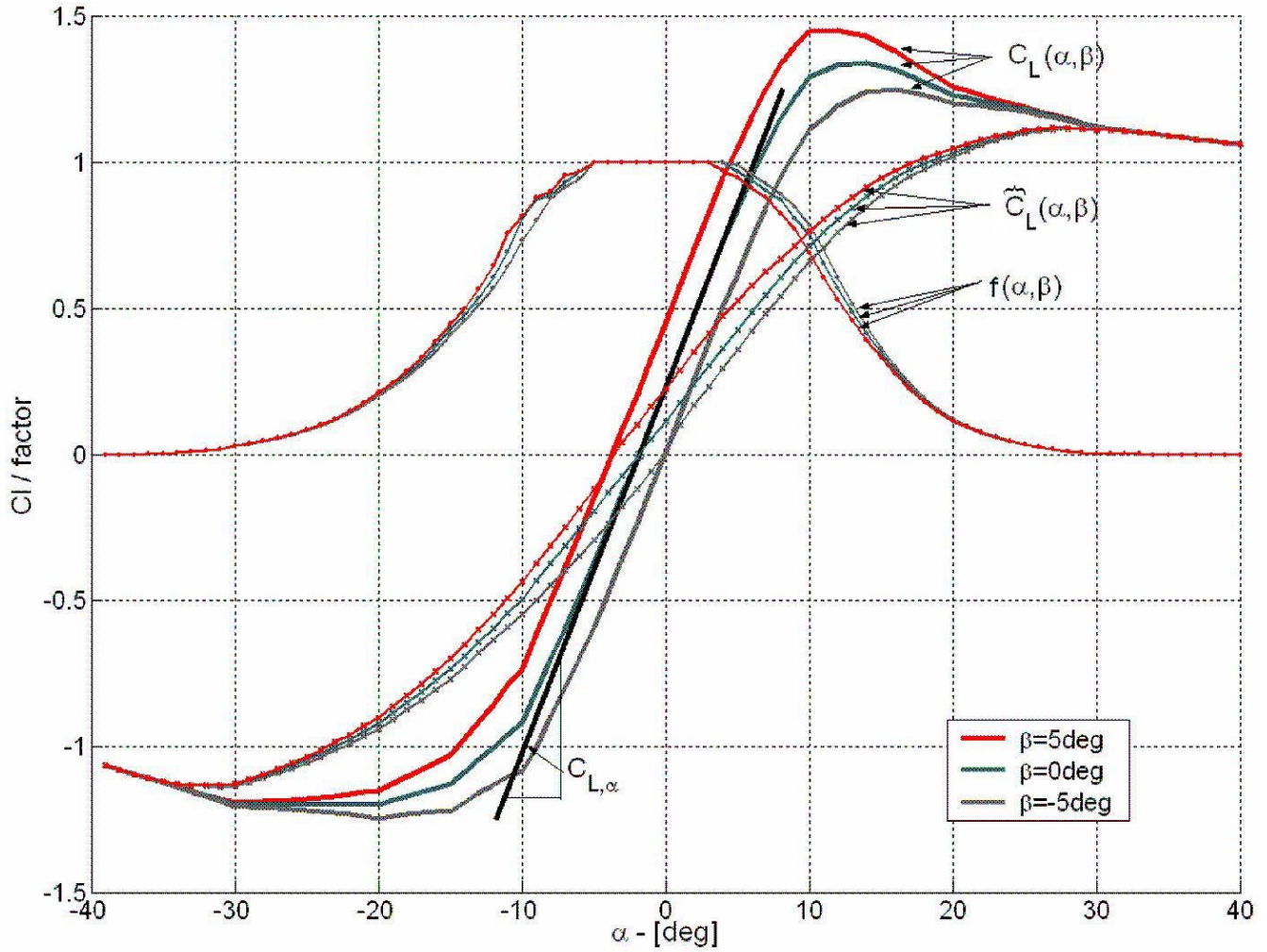


FIGURE 3 STATIC LIFT COEFFICIENT AND SEPARATION CURVES FOR -5° , 0° AND 5° FLAP DEFLECTION.

2.1.3 THE DYNAMIC VISCOUS PART OF THE DYNAMIC STALL MODEL

The Beddoes-Leishman type model assumes that for a given lift there is a certain pressure distribution with a certain separation point. The first step of the viscous unsteady effects is given by the assumption of a time-lag between the pressure distribution and lift [30]

$$\tau_p t^* \cdot \frac{\partial \tilde{C}_L}{\partial t} + \tilde{C}_L = \frac{\partial C_L}{\partial \alpha} \Big|_{\beta=0} (\hat{\alpha} - \hat{\alpha}_0) + \pi \frac{c}{2U} \frac{\partial \alpha}{\partial t} \quad (19)$$

the \tilde{C}_L on the left side indicates the pressure lagged lift coefficient, whereas, the right side contains the unsteady inviscid lift. The next step with the unsteady effect concerns the trailing edge separation function, which should include an empirical model for the dynamics from the boundary layer. The dynamics of the boundary layer is modeled through the dynamic trailing edge separation variable \tilde{f} .

$$\tau_b t^* \cdot \frac{\partial \hat{f}}{\partial t} + \hat{f} = f \left(\frac{\tilde{C}_L}{\frac{\partial C_L}{\partial \alpha}}, \hat{\beta} \right) \quad (20)$$

Two time constants have been used so far, the τ_p and τ_b corresponding to an assumed dynamic pressure-lift lag and a boundary layer lag which physically could be interpreted as the time it takes the boundary layer to buildup when subject to trailing edge separation. Assuming small angles the induced viscous drag is given by

$$C_{D,ind} = (\hat{\alpha} - \acute{\alpha}) C_{L,dyn} \quad (21)$$

$$\hat{\alpha} = \alpha - \alpha_0(\beta) \hat{f} \quad (22)$$

$$\acute{\alpha} = \hat{\alpha} - \hat{\alpha}_0(\hat{\beta}) \hat{f} \quad (23)$$

where the contribution from the trailing edge flap to the geometric incidence $\hat{\alpha}$ and the effective incidence $\acute{\alpha}$ is scaled with the unsteady trailing edge separation function \hat{f} in an effort to diminish the flap effect on the induced drag for the stalled conditions where the flap generally has less effect.

In the Beddoes-Leishman model, the unsteadiness of the pressure drag due to the variations in trailing edge separation point is deducted from the analytical expression for the pressure drag on a flat plate in a potential Kirchoff flow

$$C_{D,flat_plate} = \frac{\partial C_L}{\partial \alpha} \alpha^2 \left(\frac{1 - \sqrt{f}}{2} \right)^2 \quad (24)$$

Beddoes and Leishman later modified this equation due to unfavorable comparisons with experimental result, which has been modified yet again to include the effect of the trailing edge flap deformation. It is assumed that the factor $(1 - \sqrt{f})^2 / 4$ described the pressure drag variation from the trailing edge separation point, the unsteady contribution to total drag because of \hat{f} lags behind $\acute{\alpha}$, hence the unsteady drag contribution becomes

$$C_{D,sep} = [C_D(\acute{\alpha}, 0) - C_D(\alpha_0, 0)] \left[\left(1 - \sqrt{\hat{f}} \right)^2 - (1 - \sqrt{f})^2 \right] / 4 \quad (25)$$

As for the drag the unsteady moment operates around the measured or calculated quasi steady moment coefficients. The unsteady separation point affects the moment as the zones of recirculation moves towards the leading edge causing a more uneven pressure balance with most suction force near the leading edge. This is modeled through the pressure center moment arm o which can be calculated using the quasi steady moment coefficients

$$o = \frac{C_M(\alpha, 0) - C_M(\alpha_0^c, 0)}{C_M(\alpha, 0)} \quad (26)$$

$$C_{M,sep} = \left[\frac{\partial C_L}{\partial \alpha} \Big|_{\beta=0} (\hat{\alpha} - \alpha_0^c) \hat{f} + \tilde{C}_L(\hat{\alpha}, 0)(1 - \hat{f}) + \pi \frac{c}{2} \frac{\partial \alpha}{\partial t} \right] [o(\hat{f}) - o(f)] \quad (27)$$

The dynamic and viscous lift, drag and moment coefficients was presented in the work by Hansen et al [30] the effect of a deformable trailing edge flap was added in the work by Andersen et al [21] and finally given here as

$$C_{L,dyn} = \frac{\partial C_L}{\partial \alpha} \Big|_{\beta=0} (\hat{\alpha} - \hat{\alpha}_0) \hat{f} + \tilde{C}_L(1 - \hat{f}) + \pi \frac{c}{2} \frac{\partial \alpha}{\partial t} \quad (28)$$

$$C_{D,dyn} = C_D(\hat{\alpha}, 0) + C_{D,ind} + C_{D,sep} \quad (29)$$

$$C_{M,dyn} = C_M(\hat{\alpha}, 0) + C_{M,sep} + \Delta C_M^* \hat{f} - \pi \frac{c}{4} \frac{\partial \alpha}{\partial t} \quad (30)$$

The last term in the dynamic moment Equation (30) is the so called added mass or pitch rate damping term, it is important when predicting the classical flutter limits.

2.1.4 RESULTS AND DISCUSSION

Figure 4 illustrates that the lift for the suggested dynamic stall model operates in agreement with the measurements performed in the Velux wind tunnel described in the work of Bak et al [12]. Arrows indicate the orientation of the loops in time. The incidence is changed harmonic at three different reduced frequencies $k=\omega c/(2U)$, with ω being the actual frequency of the harmonic flap motion. Full lines show the measured ΔC_L loops from Velux. Lift values are shifted so $\Delta C_L=0$ for $\beta=0^\circ$. Dotted lines represent the presented model. The trailing edge flap deflection ranges from -3° to 1.97° for reduced frequency $k=0.081$, whereas, the reduced frequency $k=0.181$ ranges from $\beta=-2.8^\circ$ to 1.3° . Arrows indicate the orientation of the loops in time. For the quasi-steady case the lift measured in the wind tunnel is used directly in the model, unsteady effects are given by the present model, which match the dynamic lift loops measured in the wind tunnel well for the reduced frequencies and amplitudes used.

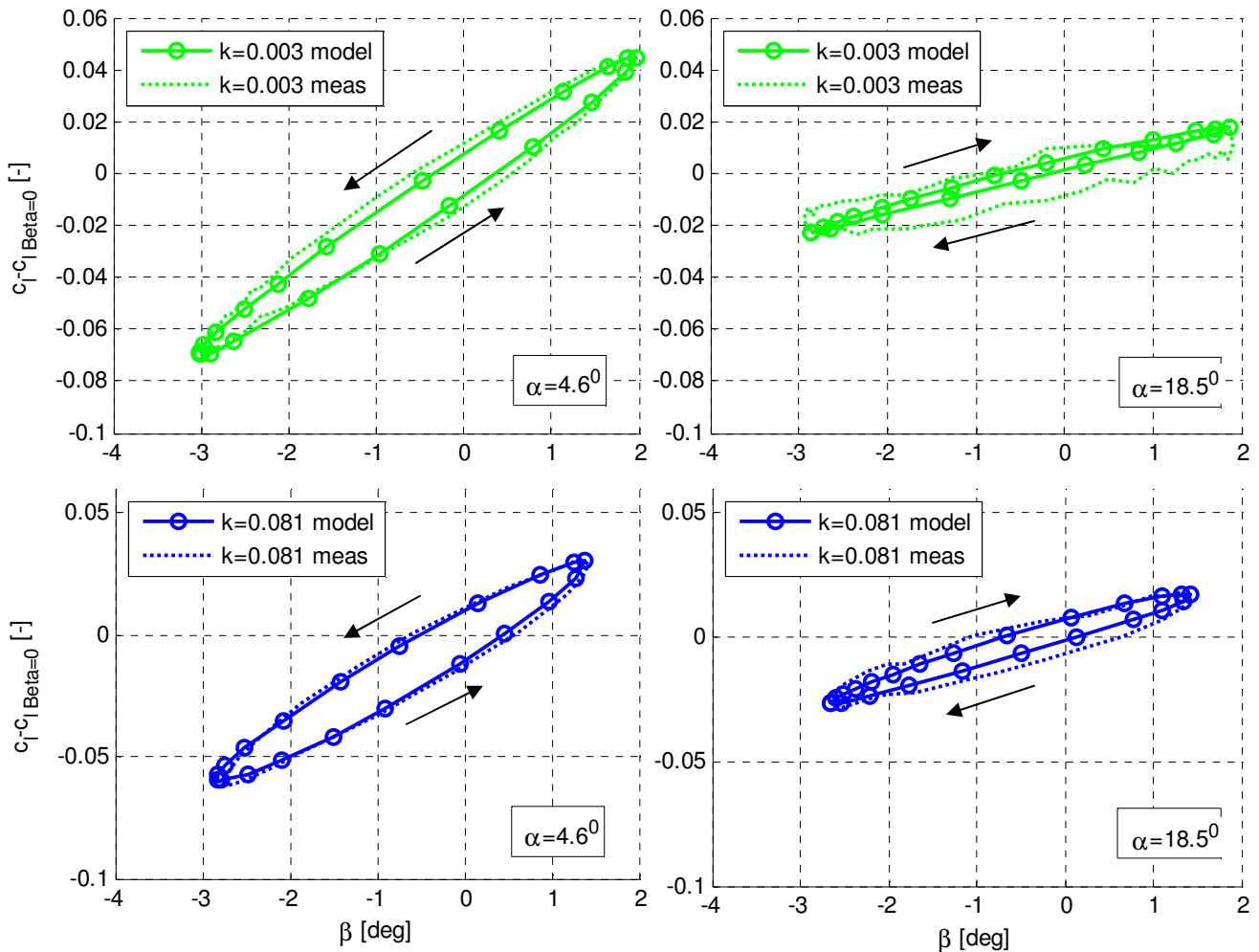


FIGURE 4 UNSTEADY LIFT COEFFICIENT COMPARISON BETWEEN THE PRESENT MODEL AND MEASUREMENTS (LEFT) ATTACHED FLOW REGIME USING A CONSTANT INCIDENCE AT 4.6° (RIGHT) SEPARATED FLOW REGIME USING A CONSTANT INCIDENCE AT 18.5° .

For incidence angle at 4.6° there is a good agreement between measurements and this model. For incidence at 18.5° in deep stall the deformable trailing edge flapping motion creates loops which are well captured by the model. Notice how the loop slope is becoming steeper for increased reduced frequency, a feature also seen in the measurements. Although the Velux wind tunnel was not originally intended for blade measurements and the turbulence intensity is relatively high, around one percent, the measurements have shown a high level of reproducibility. As part of an inherent procedure the corrected steady state measurements are compared to computational fluid dynamics, literature data and previous measurements. Factors like tunnel blockage are included in the corrections of the raw measurements; however, it should be strongly emphasized that the present model uses the steady state measurements as input.

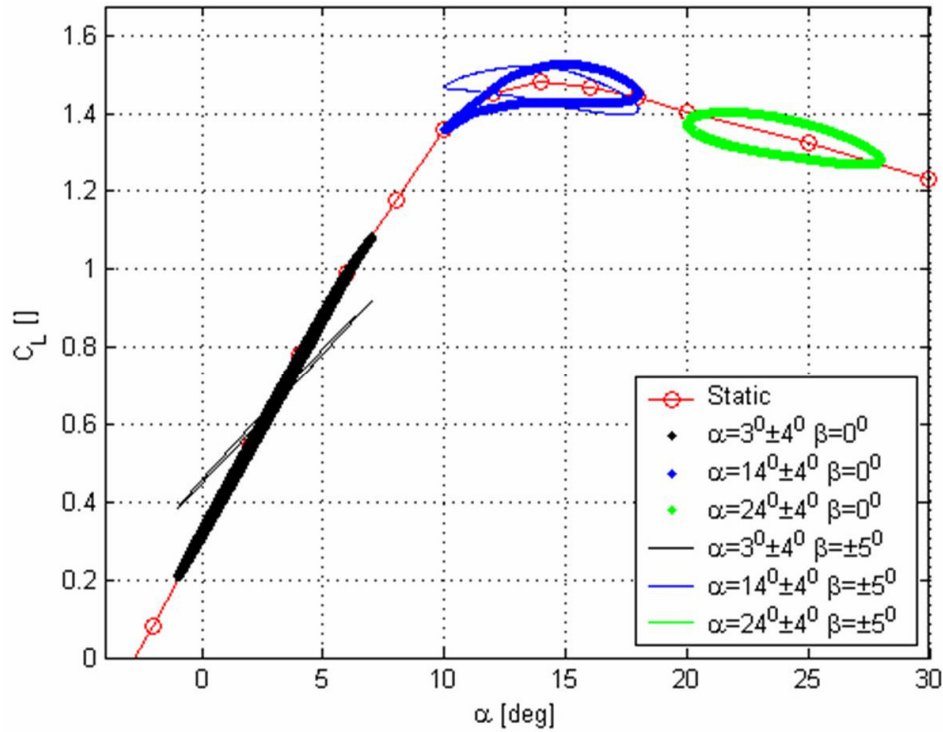


FIGURE 5 UNSTEADY C_L FROM COUNTER-PHASE PITCHING AND DEFORMABLE TRAILING EDGE FLAP OSCILLATORY MOTION.

To show the computational possibilities offered by the new model, Figure 5 shows oscillatory pitching motion and deformable trailing edge flap motion in counter phase where the reduced frequency is $k=0.1$. The amplitudes for the oscillatory pitching motion are 4° and 5° for the flap motion. It is seen that the C_L loop can be halved using the combined counter-phase flap deflection and pitching motion compared to the pure pitching motion.

2.1.5 CONCLUSIONS OF THE DYNAMIC STALL MODEL

A dynamic stall model has been developed which predicts the unsteady aerodynamic forces and moments on an airfoil section undergoing arbitrary motion in heave, lead-lag, pitch and trailing edge flapping. For the separated flow region this dynamic stall model becomes a crossover between the inviscid model of Gaunaa [29] and the model of Hansen et al [30] which include the effect of flow separation. The dynamic lift in both stalled and attached region show good agreement with the measurements performed in the Velux tunnel, which can be found in the work of Bak et al [12].

2.2 WAKE MODELLING

Wind turbines produce wakes, see Figure 6. The Blade Element Momentum (BEM) model is often used in aeroelastic simulations. Three dimensional flow effects are not readily considered due to the stream tube strip assumption which also forms the basis for the derivation of the axial induction. Consequently, the induction caused by actuating the trailing edge flap is limited to the part of the blade where the flap is attached.

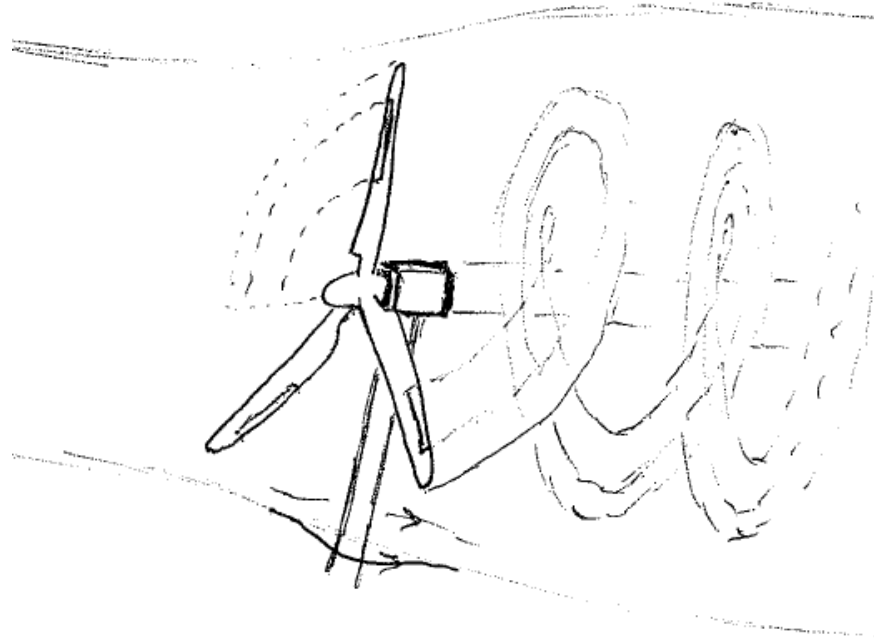


FIGURE 6 WIND TURBINE WAKE ILLUSTRATION.

There are several motivations for incorporating a near wake model in a BEM based model. The BEM theory is derived on the basis on a steady state assumption. On wind turbine rotors the loading is highly dynamic due to turbulence, actuators and various eigenmotions. The induction has to incorporate a Dynamic inflow model in order to include the effects of the dynamic wake. Different dynamic inflow models in aeroelastic codes are described [35] [36]. Various computational fluid dynamic codes offer a detailed three dimensional flow, but are computationally heavy for longer unsteady load computations. The Near Wake model [37] determines the unsteady wake based on the vortex formulation which has shown to be a good balance between computational speed and accuracy. The complete vortex system behind a rotating blade in an unsteady environment consists of the trailed vorticity due to radial variation in the bound circulation along the blade and the shed vorticity from the time variation of the bound circulation. In 3D the induction represent the influence from the rest of the wing on a section of the wing. By considering only the trailed vortex system of one quarter of a revolution, it is possible to approximate the single blade near wake contribution to the induction by exponential functions. This is done to speed up the calculation of the dynamic induction. The originally proposed two term indicial function approximation [38] of the normalized Biot-Savart circular vortex arc equation are in the present work replaced by variable indicial terms fitted using constrained

optimization for a better approximation of the exact response. Besides the quarter revolution near wake contribution to the induction it is also necessary to consider the contribution from the other blades and the far wake in general. The total loading of the rotor, is a combination of the dynamic inflow model [39] and the suggested Near Wake model. The cross plane vortex filament extension by Wang & Coton [40] has been included in the present model allowing the vortex filament surface to shift away from the rotor plane, adding a tangential induction component to the contribution from the near wake model.

2.2.1 NEAR WAKE MODEL

The near wake geometry is shown in Figure 7. The model is an extension of the near wake model proposed by Beddoes [38]. Beddoes states that the induced velocity contribution dw at point A from a vortex element of length ds , azimuth position Ω , strength Γ at radius r is

$$dw = \frac{\Gamma ds}{4\pi r^2} \frac{1 - \left(1 - \frac{h}{r}\right) \cos(\Omega)}{\left[1 + \left(1 - \frac{h}{r}\right)^2 - 2\left(1 - \frac{h}{r}\right) \cos(\Omega)\right]^{3/2}} \quad (31)$$

The induced velocity at point A can be normalized with the initial value of the induction dw_0 which is the initial influence of a vorticity filament trailed from the blade.

$$\frac{dw}{dw_0} = \frac{|h| \frac{h}{r^2} \left(1 - \left(1 - \frac{h}{r}\right) \cos(\Omega)\right)}{\left[1 + \left(1 - \frac{h}{r}\right)^2 - 2\left(1 - \frac{h}{r}\right) \cos(\Omega)\right]^{3/2}} \quad (32)$$

$$dw_0 = \frac{\Gamma ds}{4\pi h|h|} \quad (33)$$

The circulation Γ is derived from the chord length c , relative velocity V_r and lift coefficient C_L using Joukowsky's law

$$\Gamma = \frac{1}{2} V_r c C_L = \frac{L}{\rho V_r} \quad (34)$$

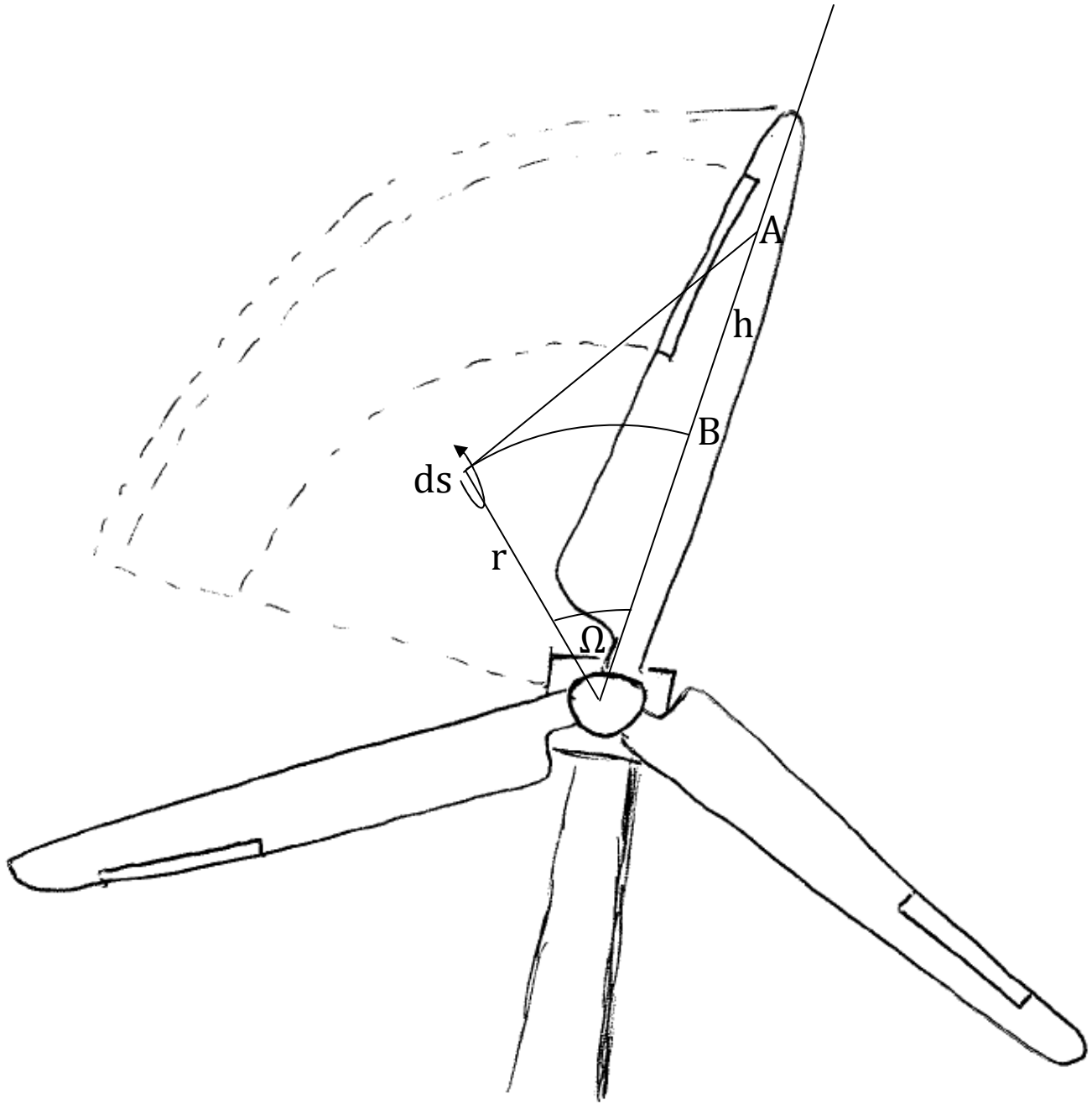


FIGURE 7 GEOMETRY FOR THE NEAR WAKE MODEL.

The indicial function technique was also initially suggested by Beddoes to approximate Equation (32) by a series of exponential functions

$$\frac{dw}{dw_0} = \sum_{k=1}^n c_k e^{b_k \frac{\Omega}{\Phi}} \quad (35)$$

Equation (35) represents the decay of influence from the trailed circulation for the vortex element as a function of the circular path. The contribution at time step i to the induction from one circular arc is given by Beddoes

$$w(i) = \sum_{k=1}^n Z_k(i) \quad (36)$$

$$Z_k(i) = Z_k(i-1)e^{b_k \frac{\Delta\Omega}{\Phi}} + c_k D_w e^{b_k \frac{\Delta\Omega}{2\Phi}} \quad (37)$$

$$\Phi = \frac{\pi}{4} \left| \left(1 + \frac{h}{2r} \right) \ln \left(1 - \frac{h}{r} \right) \right| \quad (38)$$

the axial induction contribution D_w from the currently generated vortex element is given as

$$D_w = \frac{\Gamma \left| \Delta\Omega \frac{r}{h} \right| \cos(\varphi)}{4\pi h \sqrt{1 + \left(\Delta\Omega \frac{r}{h} \right)^2}} \quad (39)$$

The original version of Beddoes did not include the cosine term. The cosine term represents the cross plane vortex filament extension included by Wang & Coton [40]. The tilting angle φ is introduced as

$$\tan(\varphi) = \frac{V_\infty \cos(\gamma) + w_B}{\omega r + V_\infty \sin(\gamma) \sin(\Omega) + u_B} \quad (40)$$

V_∞ is the free stream velocity, ω the angular velocity and γ is the angle between the direction normal to the rotor plane and the free stream velocity, Figure 8. The total axial induction at point A equals the sum of all the circular vortex parts originating from the blades. The original model is based on the assumption that the trailed vorticity is to be found in the rotor plane, which is a reasonable assumption for the outer part of the blade where the local tip speed ratio is high. However, for the inner part of the blade the local tip speed ratio is low and the vorticity sheet can be tilted as much as 45 ° relative to the rotor plane.

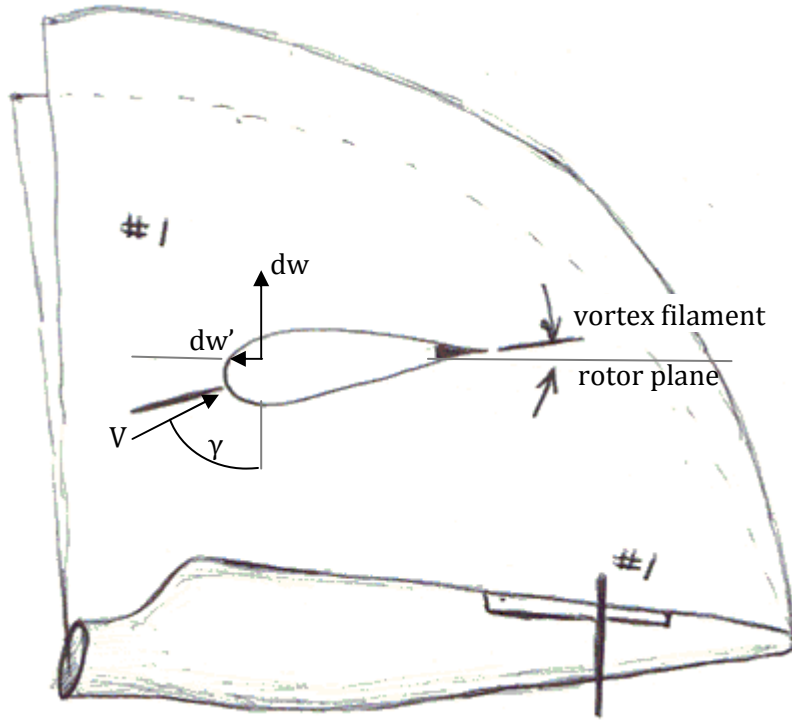


FIGURE 8 CROSS-PLANE CONVECTION.

Finally w_B and u_B are the axial and tangential velocities at point B . Contributions to the tangential induction can be found by using equations analogue to the axial induction.

$$w'(i) = \sum_{k=1}^n Z'_k(i) \quad (41)$$

$$Z'_k(i) = Z'_k(i-1)e^{b_k \frac{\Delta\Omega}{\Phi}} + c_k D'_w e^{b_k \frac{\Delta\Omega}{2\Phi}} \quad (42)$$

$$D'_w = \frac{\Gamma \left| \Delta\Omega \frac{r}{h} \right| \sin(\varphi)}{4\pi h \sqrt{1 + \left(\Delta\Omega \frac{r}{h} \right)^2}} \quad (43)$$

D'_w represents the tangential induction contribution from the currently generated vortex element and w' the total tangential induction at a given radial position on the blade.

The analytical response, Equation (32), is approximated in the work Beddoes [38] and Madsen & Rasmussen [37] by given functions. Beddoes suggested using two linear indicial equations ($n=2$) with four constant coefficients $c_1=1.359$, $c_2=-0.359$, $b_1=-1$ and $b_2=-4$. The approach presented uses a different approach. In the present work an automated tuning of the approximation constants is described. By introducing the indicial function technique the total induction at a given point on the

blade can be calculated using a reduced number of linear indicial equations. The analytical solution, Equation (32), is approximated using exponential terms. A series of n linear equations are solved iteratively for the c_k coefficients using LU factorization.

$$\left. \frac{dw}{dw_0} \right|_{\Omega=\Omega_m} = \frac{|h| \frac{h}{r^2} \left(1 - \left(1 - \frac{h}{r} \right) \cos(\Omega_m) \right)}{\left[1 + \left(1 - \frac{h}{r} \right)^2 - 2 \left(1 - \frac{h}{r} \right) \cos(\Omega_m) \right]^{3/2}} = \sum_{k=1}^n c_k e^{b_k \frac{\Omega_m}{\Phi}} \quad (44)$$

For each combination of h/r , the optimization algorithm has to determine how many exponential terms are needed and the numerical values for the coefficients c_k , b_k . The choice of Ω_m is subject to a weighting function which gives extra significance to values near the bound vorticity. Because the contribution the induction is greatest from elements close to the point evaluated.

$$\Omega_m = \frac{2(m-1)}{\pi} \left[1 - 0.9 \left(1 - \frac{(m-1)}{(n-1)} \right)^3 \right] \quad (45)$$

$m \in [1..n]$ and should implemented as an integer value. The b_k coefficients are found using a gradient based Simplex optimization algorithm [41]. The initial condition for the gradient method is taken from Beddoes first approximation. The c_k coefficients are found solving the linear set of equations

$$\begin{bmatrix} c_1 e^{b_1 \frac{\Omega_1}{\Phi}} & c_2 e^{b_2 \frac{\Omega_1}{\Phi}} & c_3 e^{b_3 \frac{\Omega_1}{\Phi}} & \dots & c_n e^{b_n \frac{\Omega_1}{\Phi}} \\ c_1 e^{b_1 \frac{\Omega_2}{\Phi}} & c_2 e^{b_2 \frac{\Omega_2}{\Phi}} & c_3 e^{b_3 \frac{\Omega_2}{\Phi}} & \dots & c_n e^{b_n \frac{\Omega_2}{\Phi}} \\ \vdots & \vdots & \vdots & \ddots & \vdots \\ c_1 e^{b_1 \frac{\Omega_m}{\Phi}} & c_2 e^{b_2 \frac{\Omega_m}{\Phi}} & c_3 e^{b_3 \frac{\Omega_m}{\Phi}} & \dots & c_n e^{b_n \frac{\Omega_m}{\Phi}} \end{bmatrix} \begin{bmatrix} dw/dw_0|_{\Omega=\Omega_1} \\ dw/dw_0|_{\Omega=\Omega_2} \\ \vdots \\ dw/dw_0|_{\Omega=\Omega_m} \end{bmatrix} \quad (46)$$

which after a simple LU factorization yields the c_k coefficients. As an example of the performance of this approach, Table 1 shows results for different approximated coefficients, for $h/r=-0.275$.

TABLE 1 (A) COEFFICIENTS FROM BEDDOES TWO TERM EXPONENTIAL APPROXIMATIONS, (B) PRESENTED SIX TERM EXPONENTIAL APPROXIMATIONS AND (C) NINE TERM APPROXIMATION. SUMMED SQUARED RESIDUAL TO THE ANALYTICAL SOLUTION IS PRESENTED IN THE LAST COLUMN FOR COMPARISON.

	k=1	2	3	4	5	6	7	8	9	$\Sigma \varepsilon^2$	
(A)	c_k	1.3590	-0.3590							0.136	
	b_k	-1.0000	-4.0000								
(B)	c_k	5.4531	2.7266	1.3633	0.6816	0.3408	0.1704			2.7e ⁻⁷	
	b_k	0.0594	-1.4211	2.2969	-0.0404	0.2367	-0.1314				
(C)	c_k	5.7500	2.8750	1.4375	0.7187	0.3594	0.1797	0.0898	0.0449	0.0225	2.0e ⁻⁷
	b_k	0.3997	-2.0504	2.8331	-1.3071	5.0194	-15.904	35.751	-42.887	19.145	

The influence of the analytical solution of Equation (32) by comparison with the approximation in Equation (35) using coefficients specified in Table 1 ($n=6$) is illustrated in Figure 9, where the range is a zoom from the total 0-90 degrees range in order to illustrate a region where the original Beddoes

approximation deviates from the analytical solution. In general the computational cost of using the near wake model to the traditional wake modal is about 1.5 – 2.5 times more costly. This depends on the radial blade discretization and the amount of indicial terms used to approximate the analytical solution. For a blade discretized with 20-30 points may be 1.5 times and for 50-60 points closer to 2.5 times more costly (n=2).

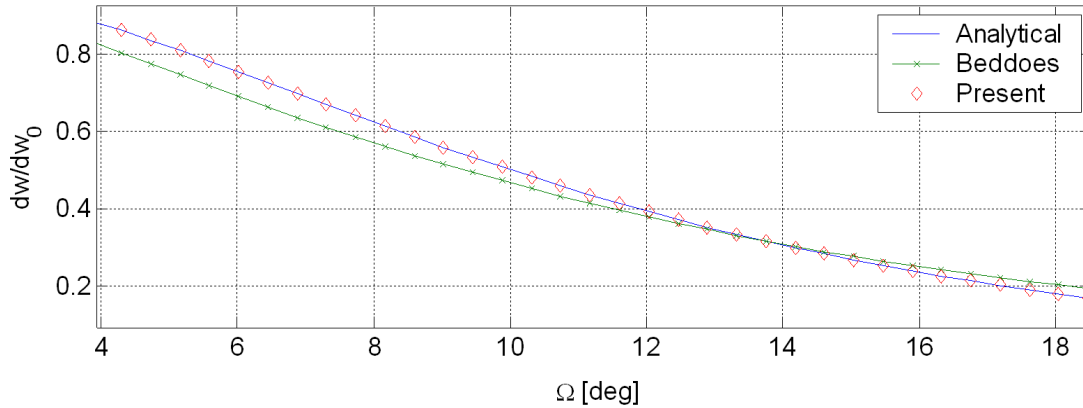


FIGURE 9 INDUCTION DECAY RATE COMPARISON OF BEDDOES TWO TERM EXPONENTIAL APPROXIMATION AND THE PRESENTED EXPONENTIAL APPROXIMATION FOR N=6.

A very good approximation to the analytical Equation (32) is obtained using the six coefficients for vortex filaments lying throughout the full range. However, a modification of Equation (38) was made as specified by Madsen & Rasmussen [37] in which ϕ avoids becoming zero for

$$\phi = 1 + \frac{h}{2r} \neq 0 \quad (47)$$

The modification replaces ϕ with a constant value equal to (1-0.25) for all cases where $h/2r > 0.25$ and then let the optimization algorithm approximate the decay rate given by Equation (32).

A pitch step of -5° is applied at some azimuth position. The development of the induction at different radial positions is shown in Figure 10. An almost immediate response of the induction is seen at the blade tip, whereas a much slower build-up takes place on the middle part of the blade. The figure furthermore illustrates the difference between using near wake decay factors presented by Beddoes (n=2) and a tuned set of exponential coefficients based on n=6. For the fast response in induction on the outer part of the blade very little difference is seen between the two sets, whereas, a larger difference is seen near the inner part of the blade. The tuned set predicts a slower growth in axial induction compared to the original coefficient set, the original Beddoes formulation over predicts the induced velocity when compared with the present formulation using six tuned exponential coefficients.

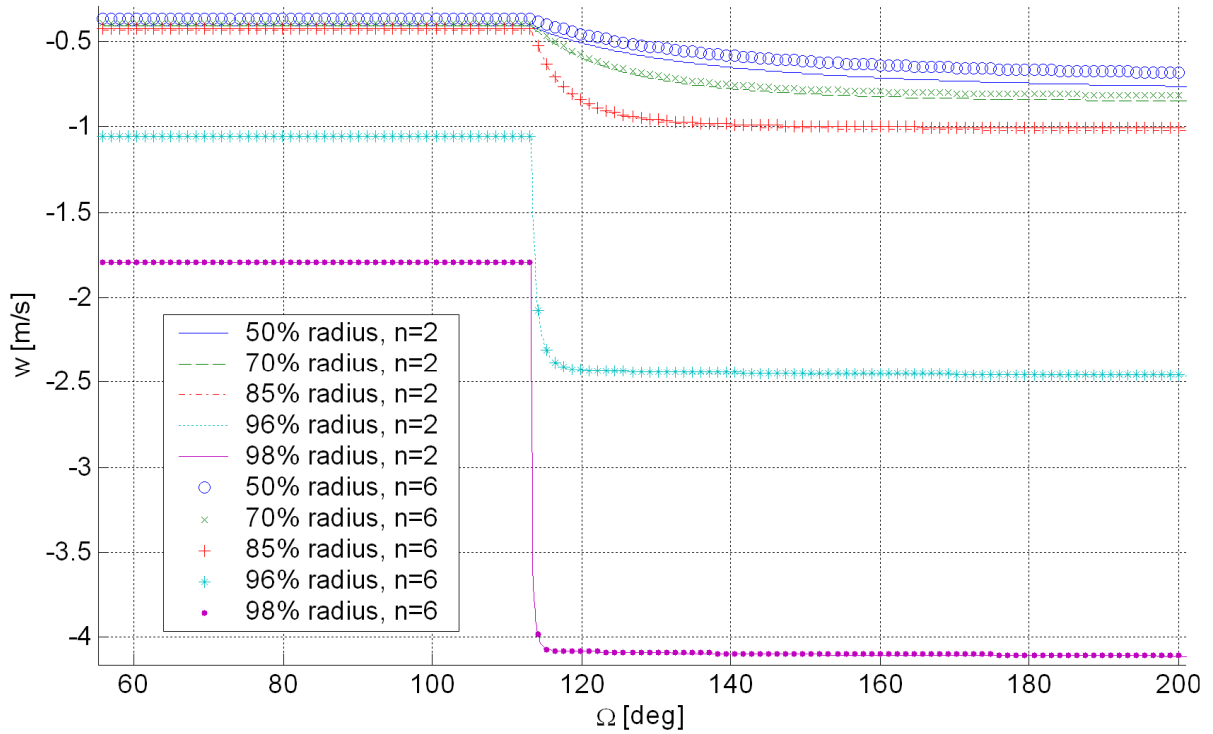


FIGURE 10 PITCH STEP INDUCTION DEVELOPMENT FOR ROTATING BLADE AT DIFFERENT RADIAL POSITIONS. BEDDOES DECAY RATE (N=2) IS COMPARED TO EXPONENTIAL FIT (N=6).

2.2.2 FAR WAKE MODEL

In order to calculate the total induction field of the rotor, it is important that the vorticity trailed and shed into the wake by the blades are represented correctly.

The frequency range for the dynamics in the near wake model includes vibrational mode eigenfrequencies from tower-dominated modes to blade-dominated modes and in the future possibly the deformable trailing edge flap devices. The slower variations in the induction like changes in the average wind speed should come from a far wake model. Elements from a far wake model described by Sørensen & Madsen [39] have been adopted in the current model. There is a considerable difference in induction variation along the blade for a rotating blade when comparing the variation computed with a near wake model and with a blade element momentum model. Along the central part of the blade the near wake predicts a lower induction because the far wake induction is missing. This far wake induction contribution is added to the present model. From the dynamic inflow model the near wake induction is cut out and the tip-loss correction is switched off. The 90° near wake cut in rotational wake is implemented by applying the far wake load scaling coefficient k_{fw} to the local thrust coefficient for an annular blade element

$$C_{T, fw} = \frac{V_r^2 c_N c k_{fw}}{V_\infty^2 2\pi r} \quad , \quad (48)$$

in which V_r is the relative wind speed seen by the section, c_N the normal force coefficient from the airfoil, r is the radius of the annular element and the undisturbed wind speed is V_∞ . Through a third order polynomial the steady axial induction factor is determined

$$a = k_1 \left(\frac{C_{T,fw}}{F} \right)^3 + k_2 \left(\frac{C_{T,fw}}{F} \right)^2 + k_3 \frac{C_{T,fw}}{F} + k_4 \quad , \quad (49)$$

where F is Prandtl's correction factor, which is unity because the tip effect is captured by the near wake model. The constants k_1 to k_4 are approximated to the inversion of $C_T(a)$. The steady induction can be corrected for yawed and tilted flow misalignments, after which the unsteady induction is added using the indicial function technique adding an element of the dynamic inflow to the model, which in discrete form is

$$z_n^{k+1} = z_n^k e^{-\frac{dt}{\tau_n}} + A_n a \left(1 - e^{-\frac{dt}{\tau_n}} \right) \quad , \quad (50)$$

where z is the wake state variables, τ_n the time constants and A_n the mixing coefficients for the indicial functions. The time constants have been normalized and approximated as in the work by Madsen & Rasmussen [37] and shown radial dependency which can be approximated by a second order polynomial with k_n constant coefficients and blade radius R

$$\tau_n(r) = k_{n,2} \left(\frac{r}{R} \right)^2 + k_{n,1} \left(\frac{r}{R} \right) + k_{n,0} \quad (51)$$

The τ_n time constants can be tuned either using CFD or measurements. The step by step procedure for the wake model is as follows;

- step 1 calculate the normal force for an annular rotor element**
- step 2 scale the number of blades (k_{fw}) to find the annular far wake thrust coefficient**
- step 3 use the third order polynomial for the far wake induction factors - Equation (49)**
- step 4 add the axial induction factor from the near wake to get the total induction**
- step 5 repeat step 1 until convergence**

A parameter study was performed in which the scaling factor k_{fw} was determined for a variety of tip speeds and rotor thrusts. By scaling the far wake, adding the near wake model and comparing with a blade element momentum model using Prandtl's tip-loss correction [42] it was possible to find k_{fw} for a number of λ , C_T combinations. The objective function used by this iterative process follows the equation

$$\int_0^R w_{BEM} dr = \int_0^R w_{BEM}(k_{fw}) dr + \int_0^R w_{NW} dr \quad (52)$$

The $k_{fw}(\lambda, C_T)$ surface will depend on design parameters like the planform. The result of the λ, C_T parameter study for a 80 meter diameter wind turbine is shown in Figure 11. Notice how the value is close to 2.7 originally suggested by Madsen & Rasmussen. The variation in thrust stems from changing the pitch and to some degree also the tip-speed, whereas, the tip-speed ratio is changed by a varying the rotational speed. There is a great resemblance for the various different rotors tested. However, it is recommended to generate this k_{fw} surface for each rotor used in order to get the same mean loading as the original BEM.

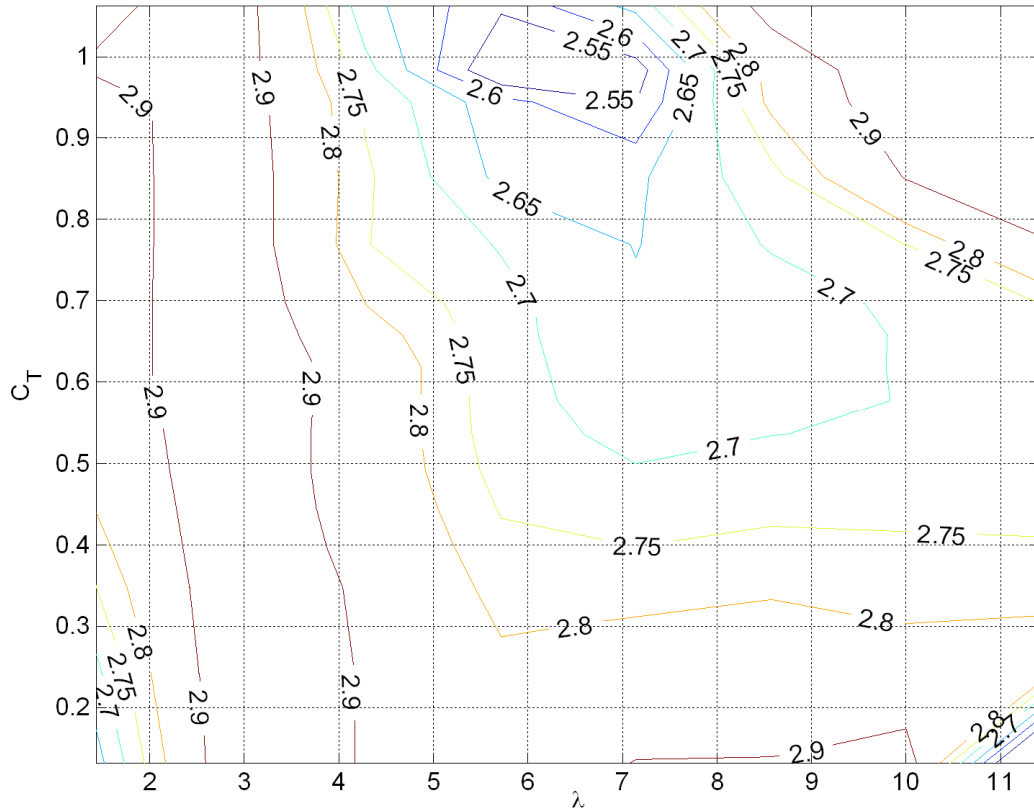


FIGURE 11 THE FAR WAKE LOAD CALIBRATION COEFFICIENT IS PLOTTED FOR DIFFERENT ROTOR LOADINGS AND TIP-SPEED RATIOS.

The following equation for the λ, C_T surface was approximated

$$k_{fw}(\lambda, C_T) = l_1\lambda^4 + l_2\lambda^3 + l_3\lambda^2 + l_4\lambda + l_5C_T^4 + l_6C_T^3 + l_7C_T^2 + l_8C_T + l_9\lambda C_T + l_{10} \quad (53)$$

$$\begin{bmatrix} l_1 \\ \vdots \\ l_q \end{bmatrix} = \begin{bmatrix} \lambda_1^4 & \lambda_1^3 & \lambda_1^2 & \lambda_1 & C_{T_1}^4 & C_{T_1}^3 & C_{T_1}^2 & C_{T_1} & \lambda_1 C_{T_1} \\ \vdots & \vdots & \vdots & \vdots & \vdots & \vdots & \vdots & \vdots & \vdots \\ \lambda_q^4 & \lambda_q^3 & \lambda_q^2 & \lambda_q & C_{T_q}^4 & C_{T_q}^3 & C_{T_q}^2 & C_{T_q} & \lambda_q C_{T_q} \end{bmatrix} \begin{bmatrix} 1 \\ \vdots \\ 1 \end{bmatrix} / \begin{bmatrix} k_{fw}(\lambda_1, C_{T_1}) \\ \vdots \\ k_{fw}(\lambda_q, C_{T_q}) \end{bmatrix} \quad (54)$$

in which $I_{1..q}$ are constants to be determined using the following least square fitting method based on LU decomposition by backwards and forward substitution indicated as / and index q is the number of simulations run (*in total 110 from $10\lambda \cdot 11C_T$*). Solving this equation gives the following coefficients for the fitted surface $I_q = [-9.02 \cdot 10^4 \ 0.0241 \ -0.213 \ 0.676 \ -2.35 \ 5.97 \ -4.95 \ 1.30 \ 0.0257 \ 2.20]^T$. The percent error between the fitted surface and the actual far wake load calibration coefficients is within two percent.

2.2.3 A NOTE ON SHED VORTICITY

The induction from the trailed vorticity system is part of the overall dynamic wake system and it interacts with the shed vorticity model and vice versa. The trailed vorticity is related to $\delta\Gamma/\delta r$ and the shed vorticity is related to $\delta\Gamma/\delta t$. The two dimensional shed vorticity is introduced through the dynamic stall model from the previous chapter.

2.2.4 COMPUTATIONAL FLUID DYNAMICS

The EllipSys3D flow solver was used for comparison with the present near-wake model. It is an incompressible Navier-Stokes finite volume flow solver written by Michelsen [43] [44] and Sørensen [45]. The surface mesh around the UpWind reference turbine had 256 cells in the chordwise direction and 128 cells in the spanwise direction Figure 12 shows a detailed view of the blade with a deflected flap.

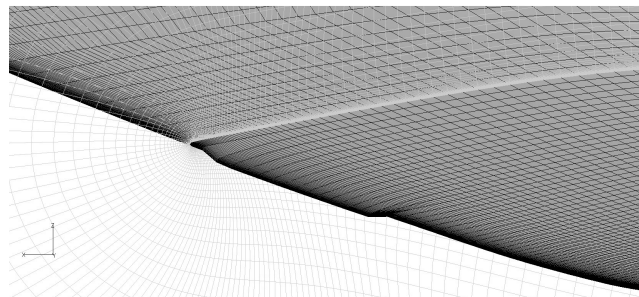


FIGURE 12 DETAILED VIEW OF THE MESH AROUND THE UPWIND BLADE FITTED WITH A TRAILING EDGE FLAP.

The present simulations were run assuming steady state since the flap was static.

2.2.5 RESULTS WAKE MODELLING

The present wake model is compared with the original Blade Element Momentum (BEM) model. The radial variation of the induction distribution for the rotating blade computed with the components of the NW model, the scaled FW BEM model the pure BEM model is shown in Figure 13; calculations are performed at 7m/s constant wind speed with constant rotor speed $\lambda = 9.7$ using cross-plane convection by Wang & Wong [40]. Notably the present model also models the effects of the tip vortex. Some difference exists locally between the BEM model and the present model with regard to the axial induction for the outer and inner part of the blade; however, on the integral blade scale the steady state induction is identical.

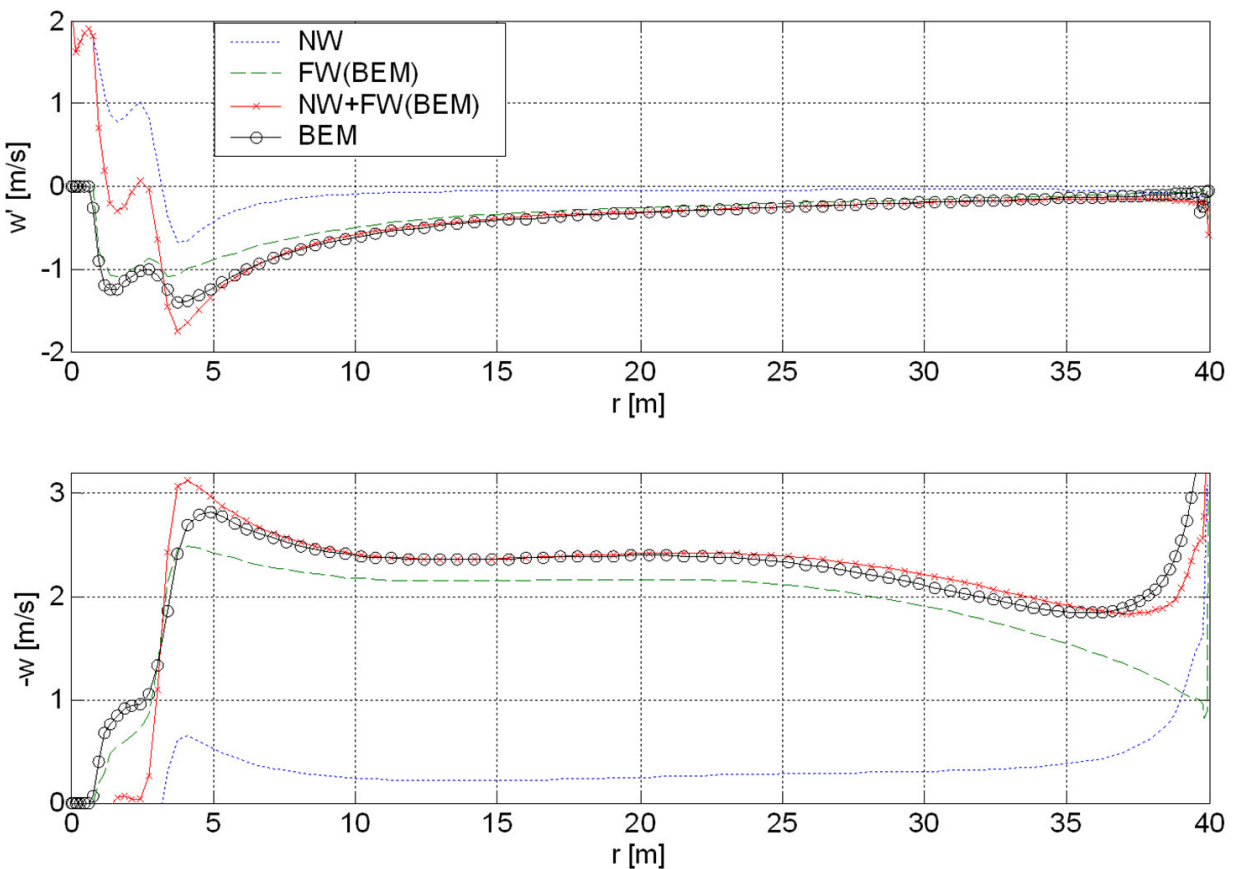


FIGURE 13 THE NEAR WAKE 'NW' AND THE FAR WAKE 'FW' IS COMPARED TO THE ORIGINAL BLADE ELEMENT MOMENTUM CODE 'BEM' AND THE WAKE IMPLEMENTATION IN HAWC2 'NW+FW' FOR (TOP) TANGENTIAL INDUCTION AND (BOTTOM) AXIAL INDUCTION.

Figure 14 is an example of the time development of the induction due to a trailing edge flap actuation as a combined contour surface plot.

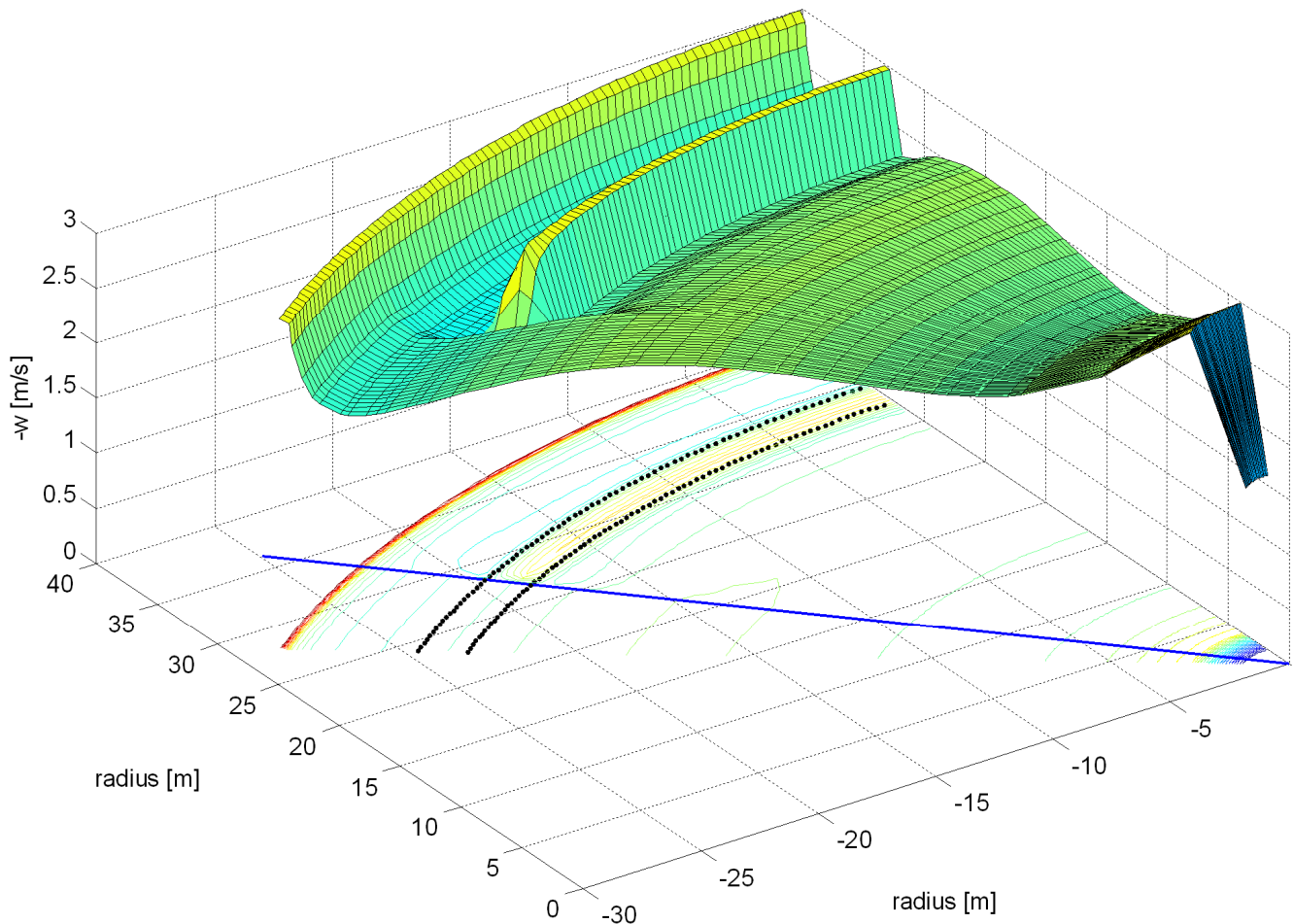


FIGURE 14 ILLUSTRATES SNAP SHOTS OF THE ROTATED AXIAL INDUCTION FOR GIVEN CONSTANT TIME INTERVALS. A TWO METER DEFORMABLE TRAILING EDGE FLAP IS MOUNTED ON THE BLADE AT RADIUS 32 TO 34 METERS PERFORMING A STEP CHANGE OF 3° . THE LOCATION OF THE FLAP IS ILLUSTRATED BY THE CONCENTRIC DOTTED DOTS, AND THE TIME OF ACTUATION IS SHOWN BY THE STRAIGHT LINE CROSSING ORIGO.

The strong induction at the tip as well as at the blade root is the most recognizable feature. One of the main advantages of the present model in comparison with BEM theory is that the induction at a point on the blade is influenced by the trailed vorticity from all the other points on the blade. This means that changes in the aerodynamic properties locally on the blade will have some influences on the induction at the neighboring sections. Examples of local changes are the use of deformable trailing edge flaps, stall strips and active vortex generators. The effect of a two meter long deformable trailing edge flaps

is illustrated in Figure 14. A three degree flap deflection step at the time outlines with the blue line causes a resulting development in induction. Notice that the effect in induction for the two meter flap exceeds the area where the flap is mounted on the blade.

This effect is illustrated more clearly in Figure 15 with a comparison between the traditional BEM model, the present wake model and a steady state Ellipsys 3D Computational Fluid Dynamic (CFD) calculation. The radial vorticity distributions for the five Mega Watt (MW) reference wind turbine from the UpWind project⁴ is used.

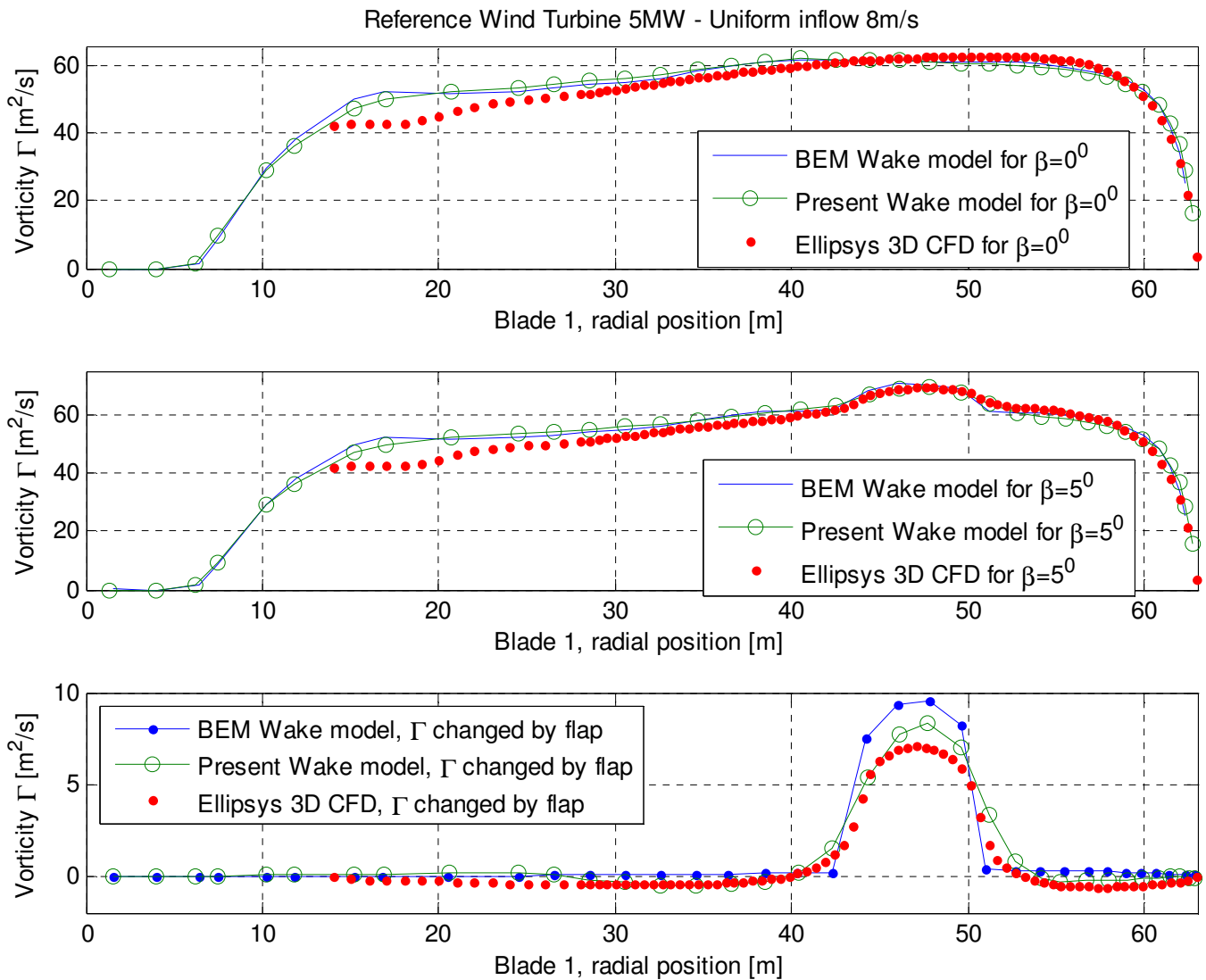


FIGURE 15 STEADY STATE RADIAL VORTICITY DISTRIBUTIONS FOR THE REFERENCE TURBINE AT UNIFORM INFLOW 8M/S (UP) NO FLAP ACTIVITY (MID) FLAP DEFLECTED 5 DEGREE POSITIVE (DOWN) DIFFERENCE IN VORTICITY DUE TO FLAP DEFLECTION FOR THE ORIGINAL BEM WAKE MODEL, THE PRESENT PROPOSED WAKE MODEL AND ELLIPSY 3D (CFD). THE FLAP IS LOCATED FROM 44.1 TO 50.4 METERS.

⁴ SIXTH FRAMEWORK PROGRAMME (FP6), 2009.
Available from Internet <http://www.upwind.eu/> Accessed 17 September 2009.

According to Figure 15 (UP, MID) the BEM model has a slightly lower vorticity around the radial positions 25-35 meters and higher vorticity around 15 meters than the present near wake model. But as a whole the vorticity distribution of these two models appears identical. There is a slightly greater difference between these two models and CFD. For the 15-40 meter region the CFD vorticity is lower than the two models and for the 45-60 meter region the vorticity is higher.

When deflecting the flap downwards (MID) the vorticity is increased for all models around the flap which is located from 44.1-50.4 meters. For the traditional BEM wake model the increase in vorticity appears to be greater especially around the flap mid point around 47 meters compared to the present wake model.

The quasi steady effect in vorticity of the deflected flap is best evaluated when subtracting the non-flapped vorticity distribution with the flapped vorticity distribution; see Figure 15 (DOWN). The integral change in flap deflection appears comparable for the BEM model and the present near wake model. The CFD model has slightly more negative vorticity from 20-25 meters. Some trends are similar between the present near wake model and CFD especially in the 30-40 meter regions and at 55 meters.

The effect of the flap is felt throughout the blade in the present wake model and the CFD model. Whereas, the traditional BEM wake model experiences a local effect in vorticity near the flap.

An important future work would be to investigate the effect of adding additional discrete points in the present near wake model especially around the flap edge regions. This is important because the radial vorticity gradient is greater when flapping.

Another comparison based on the reference turbine is shown in Figure 16. The GENeral Unsteady Vortex Particle (GENUVP) code by Voutsinas [46] developed at the National Technical University of Athens (NTUA) and the present wake model is compared. The comparisons was carried out using the rainflow counting technique in which normal force amplitudes at 75% radius for a ten minute simulated series was counted. The simulations are based on constant rotor rotational speed (0.964 rad/s) and turbulent wind inflow conditions at 8m/s mean wind speed and 15% turbulence intensity.

The range in Figure 16 represent peak-to-peak rainflow counted amplitudes in the 75% normal force sensor and the number of cycles is the number of counted amplitudes with a given range of amplitude in the 10 minute simulated time series used. There is a good agreement between the two models for most regions of amplitudes counted. However, there is a discrepancy in small amplitudes. GENUVP predicts more small oscillations than the present wake model. Further investigations are needed. It has been suggested that the discrepancy between the two models may lie in the interpolation procedure for the turbulence box. It is difficult to conclude which of the two versions Beddoes $n=2$ and the approximated $n=7$ offers the best wake model. It takes 1.5 times longer to calculate the $n=7$ version compared to the original Beddoes $n=2$. The counted cycles for the traditional BEM wake model follows the other wake models well, although the decrease in counted cycles for larger range of amplitudes appears slightly more scattered by comparison.

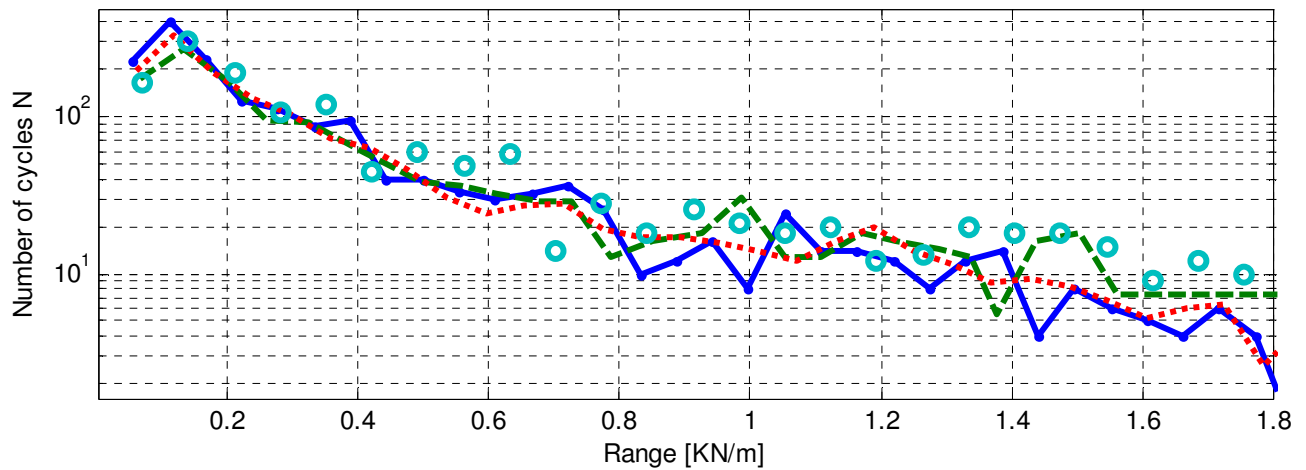
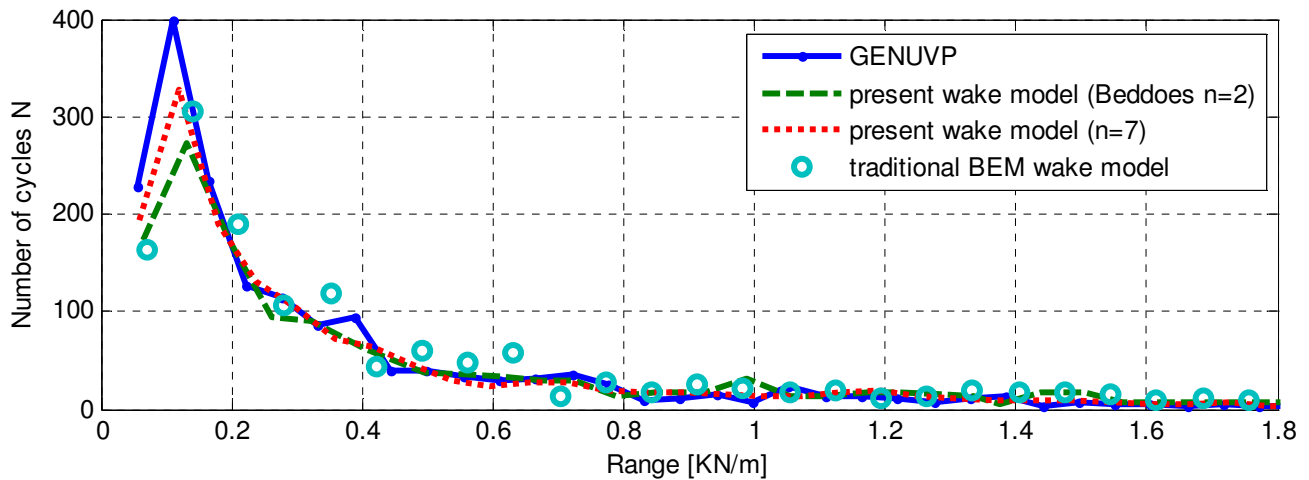


FIGURE 16 COMPARISONS BETWEEN THE TRADITIONAL BEM WAKE MODEL IN HAWC2, TWO VERSIONS OF THE PRESENT WAKE MODEL AND THE GENUVP FROM CRES USING THE RAINFLOW COUNTING TECHNIQUE BASED ON NORMAL FORCE AMPLITUDES AT 75% BLADE RADIUS.

2.2.6 CONCLUSIONS WAKE MODELLING

The Near Wake (NW) model originally proposed by Beddoes [38], investigated by Madsen & Rasmussen [37] was extended by the work of Wang & Coton [40] and implemented in the aeroservoelastic tool HAWC2 [25]. A better approximation to the analytical trailed vorticity filament equation is proposed through several indicial terms with optimized coefficients. The present model is compared to the GENERAL Unsteady Vortex Particle (GENUVP) model [46] developed at the National Technical University of Athens. The normal force at 75% radius is compared using the rainflow counting technique.

Several results have been obtained

- The NW model clearly captures the same inductive tip effects as Prandtl for the Blade Element Momentum (BEM) model.
- Although there are local variations in the inductions between the NW and BEM model, the induction is identical when integrated over the whole blade.
- The normal force at 75% radius shows a strong correlation between GENUVP and HAWC2 for most frequencies. There is a general discrepancy for the smallest amplitudes which may have something to do with how the turbulent wind box is interpolated for the two aeroelastic codes.
- A series of deformable trailing edge flaps was mounted on the five Mega Watt reference turbine used in the UpWind project. By activating the flaps the induction clearly shows tendencies to couple in the radial direction, which is not the case for the BEM formulation, where the induction only couple through the elastic beam elements.

Future work

- In the work of Madsen & Rasmussen [37] an investigation of aerodynamic work by sinusoidal fluctuation in the NW was carried out, this and an investigation into aerodynamic damping still remains to be carried out.
- Further investigations into the far wake scaling factor for all blades using computational fluid dynamic simulations.
- Adding additional discrete points in the present near wake model especially around the edge regions of the flap.

Results of aeroelastic simulations incorporating the deformable trailing edge flaps will be presented in this chapter. The following sections contain descriptions of sensors, control algorithms and obtained results. Cost-effective sensors and the integration with various actuators have been used for decades. It is generally accepted that computing power, memory, and sensors follow the exponential decrease in size, cost, and power consumption associated with Moore's Law. The following is a list of sensors used, they are all assumed available and feasible to use on a wind turbine

- rotor speed sensor
- pitch angle sensor
- blade strain gauge measuring strain from flapwise blade deflection
- flap strain gauge measuring flap deflection
- Pitot tube inflow measurement

The flap controllers proposed in Chapter 3 consists of filters and gains. More complex controllers could have been used for the flaps, for instance non-linear controllers have been suggested by Henriksen [47]. Tools for determining the models experimentally have been proposed by Wingerden [19]. The more advanced models can be used for a range of applications like anticipating future events as model predictive controllers by Henriksen [48]. The simple approach was chosen first and foremost to make the design as simple as possible for these investigations.

Initial studies by revealed that actuating the flap coupled greatly with torsional, flapwise and somewhat edgewise blade deflections [49]. In fact, on a torsionally stiff blade, deflection of the flap to the pressure side of the airfoil generates an increase in aerodynamic load and a deflection to the suction side decreases the aerodynamic load. On a torsionally soft blade, a deflection of the flap towards the pressure surface will create a pitching moment that twists the nose of the blade towards the pressure surface, thereby decreasing the angle of attack and load. For a deflection towards the suction surface the opposite will happen. Hence a full aeroelastic investigation was deemed necessary. **Section 3.1** describes the wind turbine, the aeroelastic tool and deformable trailing edge flap used.

Section 3.2 contains the work of Andersen et al [22] where full aeroelastic simulations of a wind turbine are used to determine where to place strain gauge sensors on the blades and where to place the active flap.

Section 3.3 contains aeroelastic simulations incorporating the deformable trailing edge flap with special focus on using local flow angle measurements (Pitot tube) for fatigue load reduction.

Section 3.4 contains the work of Andersen et al [50]. Here the strain gauge sensor and the inflow sensor are combined with a power controller.

The different controllers are tested using simulated wake deficits from a wind turbine farm in **section 3.5** where extracts of the work by Markou et al [51] is presented.

The primary objective of the flap controllers presented in this chapter will be to minimize fatigue loads in the blade root regions for the flapwise direction. The **dynamic stall model** for the deformable

trailing edge flap is used in sections 3.2, 3.3, 3.4 and 3.5. The **near wake model** is used in sections 3.2 and 3.5. Besides using inflow and strain for fatigue reduction, the use of airfoil pressure difference between suction and pressure side for load control was investigated by Gaunaa & Andersen [52].

3.1 MODEL BACKGROUND

The five Mega Watt reference turbine used in the UpWind project has a rotor diameter of 126 meters. The turbine is divided into substructures like tower, nacelle and blades in the multi-body code HAWC2 [25]. Each substructure has its own coordinate system which facilitates rotations of the substructures with respect to each other. The multi body elements use the Timoshenko beam elements with six degrees of freedom per node. Aerodynamic torque, thrust and other loads are dynamically calculated using an unsteady **Blade Element Momentum** (BEM) model approach with various unsteady wake effects.

The **structural properties** of the wind turbine used for the aeroelastic calculations such as centre of gravity, elastic, shear and pitch axis is provided by Jonkman's five Mega Watt (MW) reference wind turbine [53]. This turbine is used sections 3.2, 3.3, 3.4 and 3.5.

The blade forces and blade root moments has been compared to other aeroelastic codes in Work Package (WP) 2.2 of the UpWind project. The results of these comparisons for the reference turbine are available online at <http://www.upwind.eu>.

3.1.1 THE DEFORMABLE TRAILING EDGE FLAP

The **deformable trailing edge flap** used is characterized by a smooth and continuous gradient from the non-deformable part of the airfoil to the deformable part. Furthermore, the part of the flap closest to the trailing edge has the largest structural rotation and at the point where the flap is fixed to the non-deformable part of the airfoil there is no structural rotation. In chordwise direction the flap is 10% of the chord length. This type of flap was chosen because flow separation and thereby corresponding noise and drag are reduced, compared to a rigid flap. The flap is constrained to maximum deflections of +/- 8 degree, corresponding to C_L changes of +/- 0.25. This change in lift is overrated for the piezoelectric prototypes tested in the wind tunnel. But a new prototype based on a combination of rubber and pneumatics and/or hydraulics promises larger changes in e.g. the lift. This new deformable trailing edge rubber flap prototype is described by Madsen et al [15].

3.1.2 DEFINING FATIGUE

The rainflow counting technique originally developed by Endo & Matsuiski [54], the linear damage rule by Palmgren-Miner's [55] [56] and Wöhler's curve [57] equation makes it possible to calculate the **equivalent fatigue number** for a given sensor mounted on the wind turbine. When nothing else is specified the fatigue load reduction will refer to the equivalent blade root moment in flapwise direction for a 10 minute time series. The orientation of the blade flapwise root moment follows the rotor plane and not the blade pitch axis to ensure the maximum decoupling from gravity when pitching.

3.2 CONTROL BASED ON STRAIN MEASUREMENTS

This section describes simulations of a deformable trailing edge flap controller integrated with the reference turbine. Strain gauges are mounted on the blades which serve as input for the flap controller. The effect of signal noise and delays is also investigated. It should be noted that it is likely that the current investigation also is valid for other types of sensors which measure the flapwise blade deformations or blade bending moments.

Load reductions are investigated by means of ten minute simulated turbulent 10m/s mean wind time series and effects of tower shadow and a wind shear is included.

Instead of writing up a state space model of a turbine for one specific load case for which traditional control tool box utilities can be applied, the presented work utilizes the full time marching aeroelastic code directly as a component in the control loop design, offering the full palette of parameters for a constrained optimization routine used. The downside to this approach is increased computational time.

First the control model and the sensor model will be described in Chapter 3.2.1, setup of cases investigated in Chapter 3.2.2, followed by results in Chapter 3.2.3 and finally a conclusion will be presented in Chapter 3.3.4.

3.2.1 MODEL

This section describes sensors, control algorithm, flap, optimization strategy, initial guesses, signal delays and control signal noise implementations. The simulation use finite beam elements for the blades where the normal force N and bending moment M are available and used to calculate the strain. The simple beam theory is used in the present work, in which, the measured strain ε is given by bending stress σ divided by elastic modulus E for a symmetrically bent beam

$$\varepsilon = \frac{\sigma}{E} = \frac{N}{AE} - \frac{Mh}{EI} \quad , \quad (55)$$

the blade normal force N will vary with the rotor speed and depend on blade mass, A is the cross sectional area, h is the distance perpendicular to the neutral axis and EI is the bending stiffness. A more complex model is needed for simulating strains on the full three dimensional setup of blades with spars and composite plies.

The controller is an extension of a traditional power controller [58] for the reference turbine where the generator moment and blade pitch are set using a low pass filtered rotor speed signal ω_f

$$\tau_\omega \frac{\partial \omega_f}{\partial t} + \omega_f = \omega(t) \quad , \quad (56)$$

the unfiltered rotational signal is ω and τ_ω translates to the low pass filter cutoff frequency. This enables the generator and pitch to react to low frequency rotor speed variations e.g. due to mean wind

speed changes, whereas the flaps reacts to medium and high frequency variations from elastic deformations and turbulent gusts. A high pass filter is therefore part of the flap controller, in which, the flap deflection angle β is

$$\beta = K_p [\varepsilon(r_s) - z] \quad (57)$$

$$\tau \frac{\partial z}{\partial t} + z = \varepsilon(r_s) \quad (58)$$

The actuation will be lagged in time but this will primarily be due to the inertia for large blades. The strains ε used by the control algorithm are measured a distance r_s from the blade root. Figure 17 illustrates how strain gauge sensors and flap actuators can be placed on a blade.

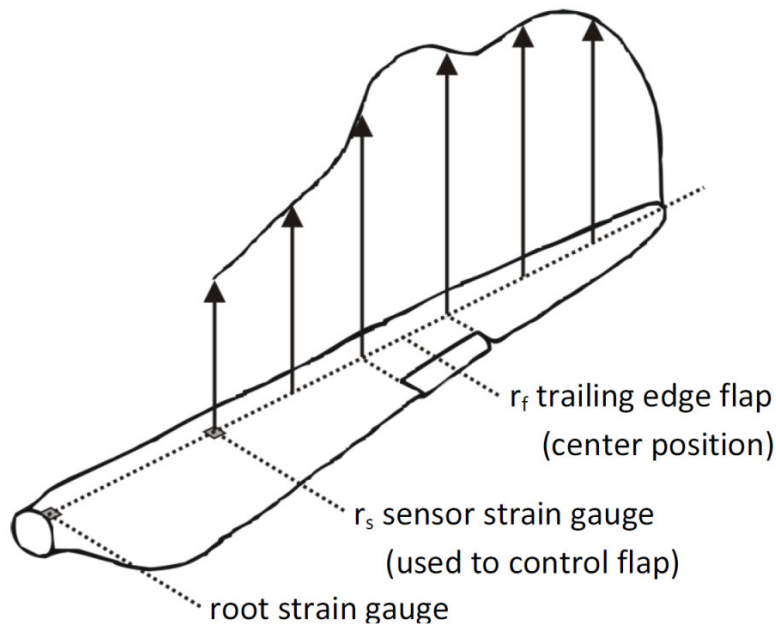


FIGURE 17 SENSORS AND FLAP ACTUATOR.

Once the location of the strain gauge is chosen, the control system will affect the blade dynamics making it a fully coupled aeroservoelastic problem which has to be solved iteratively.

Numerous parameters could be considered for the optimization runs, the ones deemed important have been divided in two groups,

- the parameter subject to sweeps, like the flap and sensor position.
- the free parameters used by the optimization routine, like the proportional gain and the filter time constants.

The trailing edge flap is constrained to deflect plus minus eight degrees. An optimization strategy is needed in order to systematically tune gains and time constants for the proposed controller.

Consider a constrained non linear optimization problem in the form

$$\begin{aligned} & \text{minimize} && M_x^*(K_p, \tau, r_f, r_s) \\ & \text{subject to} && Ax \leq b, x \geq 0 \end{aligned} \quad (59)$$

where M_x^* is sum of equivalent blade root moment fatigue load for a given turbulent wind series for all the three blades on the reference turbine and A and b describe the system of constraints.

3.2.2 SETUP OF CASES

The aeroelastic tool HAWC2 will be used to determine the optimization coefficients or gradients by means of a forward finite difference method

$$\frac{\partial M_x^*}{\partial x} = \left[\frac{\partial M_x^*}{\partial K_p} \quad \frac{\partial M_x^*}{\partial \tau} \quad \frac{\partial M_x^*}{\partial r_f} \quad \frac{\partial M_x^*}{\partial r_s} \right] \quad (60)$$

x is the optimization variable vector containing $[K_p \ \tau \ r_f \ r_s]$. The optimization is by default constrained to

$$A = \begin{bmatrix} r_f & 0 & 0 \\ 0 & r_s & 0 \\ 0 & 0 & \tau \end{bmatrix}, \quad b = \begin{bmatrix} R - 0.5\tilde{l}_f R \\ R \\ 0.4 \frac{\omega_0}{\omega_f} \end{bmatrix} \quad (61)$$

Instead of one flap per blade several flaps per blade is investigated which increase the number of x variables by a factor of four per flap. The strain gauge sensor and flap should not be placed beyond the blade length R . \tilde{l}_f is normalized flap length with regard to blade length. Constraints have been placed on maximum values for the high pass filter time constant τ given by the scaled ratio between rated rotor speed ω_0 and low pass filtered rotor speed ω_f .

When applying a gradient based optimization routine to a highly non-linear and possibly non-convex problem, there is a risk of ending up in a local minimum. To uncover this, the following parameters was used in course sweep for the reference turbine with turbulent inflow

- elastic and shear modulus of the blade (E, G)
- rotational speed of the rotor, pitch angle, mean turbulent inflow wind speeds (ω, θ, V_∞)
- proportional gain for the flap control (K_p)
- high pass filter time constant for the flap control (τ)
- flap and sensor position (r_f, r_s)

The level of coarseness for the above parameter sweeps was determined by the variations in the sum of equivalent blade root moment fatigue load (M_x^*).

The strain gauge sensors used in the control design primarily measure the elastic response rather than the actual aerodynamic excitation itself, hence the controller reacts after the aerodynamic event has occurred. Other types of delays between event and actuation exists, some are based on choice of

equipment others on control strategy. A significant increase in fatigue loads was seen when additional time lags was introduced in the flap control loop [13] [22] [49] [59]. It is therefore important to investigate the effect of having additional signal delays in the controller. Two types of signal delays have been investigated time lags and time delays. The lag is a simple first order filter

$$\tau \frac{\partial \varepsilon'}{\partial t} + \varepsilon' = \varepsilon(t) \quad (62)$$

The sensor input to the controller ε' has been filtered from the original signal effectively adding a phase lag and removing the high frequency content. A signal delay is also investigated in which the signal is placed in a stack and executed at a later time. The signal noise is defined as

$$SNR(dB) = 20 \log \left(\frac{\langle \varepsilon \rangle}{\sigma_{\vartheta}} \right) \quad (63)$$

simply dividing the mean of the signal with the standard deviation of the noise instead, often used in the field of image sensing to describe the SNR. White signal noise is used with signal to noise ratios of 1dB, 2dB, 3dB, 4dB, 5dB and 10dB.

3.2.3 RESULTS AND DISCUSSION

The elastic and shear modulus of the blades and the rotational speed was varied in an initial study to uncover some basic dynamic properties of the turbine. In Figure 18 (left) a blade with three times the elastic and shear modulus have been tested and compared to a blade with elastic and shear modulus according to the reference turbine standards, gains, time constants and flap position are swept in a rough grid then tuned for best performing parameters for more accurate values. In Figure 18 (right) rated rotational speed and half rated speed of the rotor is kept constant while tuning gains and time constants and sweeping the flap position.

Two equations for predicting well suited gains and time constants have been suggested to make the optimization procedure less time consuming. A starting guess for a proportional gain K_p is proposed as

$$K_p = \frac{0.02}{\tilde{l}_f} \frac{\sqrt{\omega_b}}{1 + 20\psi^2} \left(\frac{2\omega_0 - \omega}{\tilde{r}} \right)^{1.75} \quad (64)$$

The first flapwise mode shape for the blade (fully clamped) is normalized to unity at maximum deflection, the value ψ represents the mode shape value (between 0 and 1) at radial position \tilde{r} where the flap is positioned on the blade, ω_b is the first flapwise eigenfrequency for the reference turbine blade clamped at the blade root. When adjusting the time constant τ the state variable z will trace sensor ε faster or slower depending on τ , effectively shifting the operational frequency band for the

high pass filter. A simplified equation for finding a good starting guess for the high frequency pass filter time constant is

$$\tau = 0.045(2\omega_0 - \omega_f)^2 e^{1-\tilde{r}} \quad (65)$$

There is no way of guaranteeing that the optimization algorithm will not end up in a local minimum. However, when combining the parameter sweep option with the gradient based Simplex optimization routine considerable load reductions has been obtained, which is the ultimate goal of our efforts.

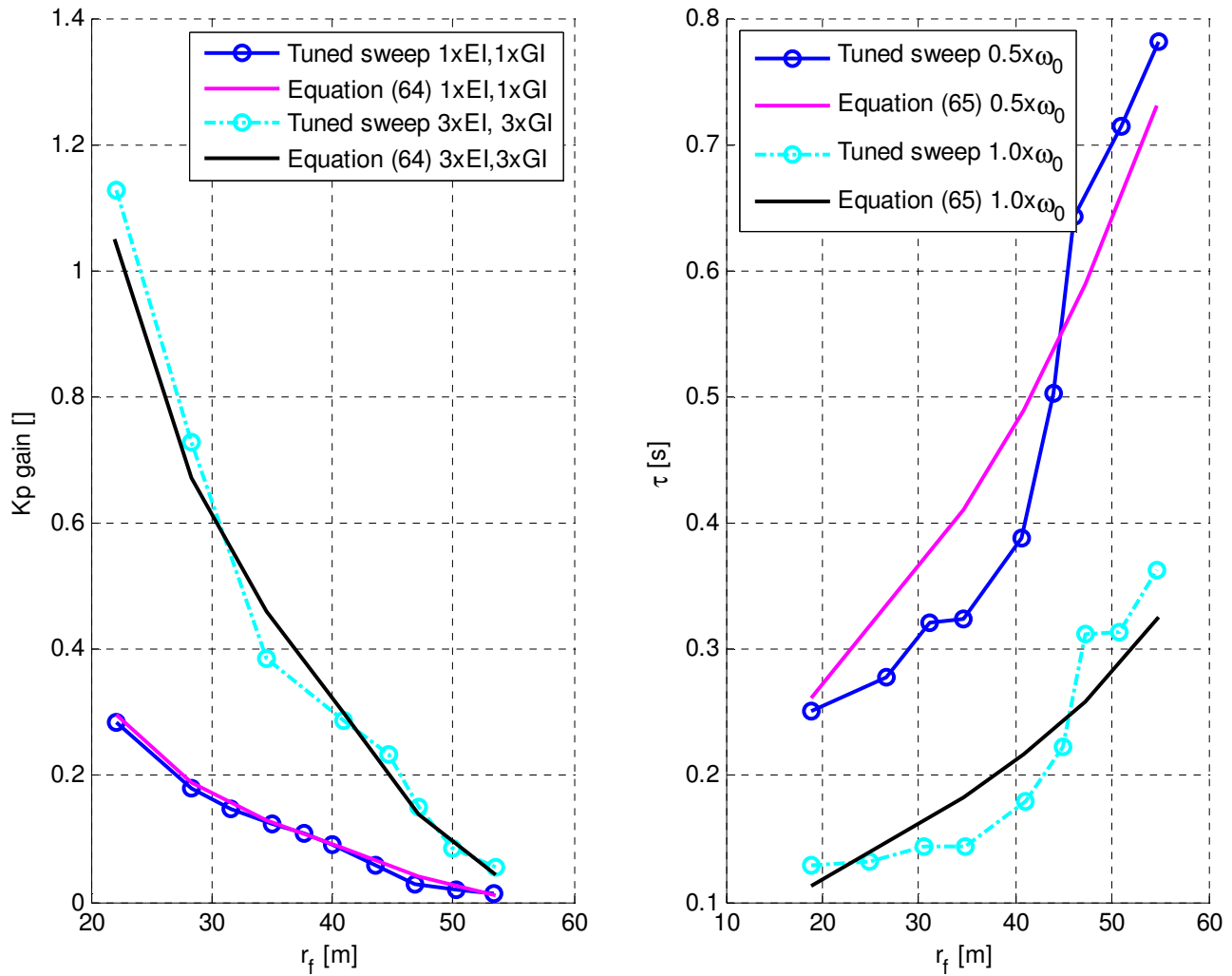


FIGURE 18 GAINS AND TIME CONSTANTS BASED ON NUMEROUS SIMULATIONS VS PROPOSED EMPERICAL EQUATIONS FOR (LEFT) GAIN AND (RIGHT) TIME CONSTANTS.

Figure 18 illustrates the difference between Equation (64) and (65) and the parameter swept and optimized cases. The approximations to the swept and tuned results in Figure 18 could have been better but as initial guesses the accuracy should be sufficient.

The search for the best combination of sensor and flap blade position was conducted for the case without control signal distortions. Figure 19 illustrates a parameter sweep of r_f and r_s while optimizing K_p . The filter time constant is set to the value specified in Equation (65) which generally is slightly above the first flapwise eigenfrequency. According to Figure 19 the 6.3 meter long flap should be mounted 42-48 meters from the blade root and the strain gauge sensor should be placed 28 meters from the blade root. Time constants used for the high frequency pass filter are according to Equation (65).

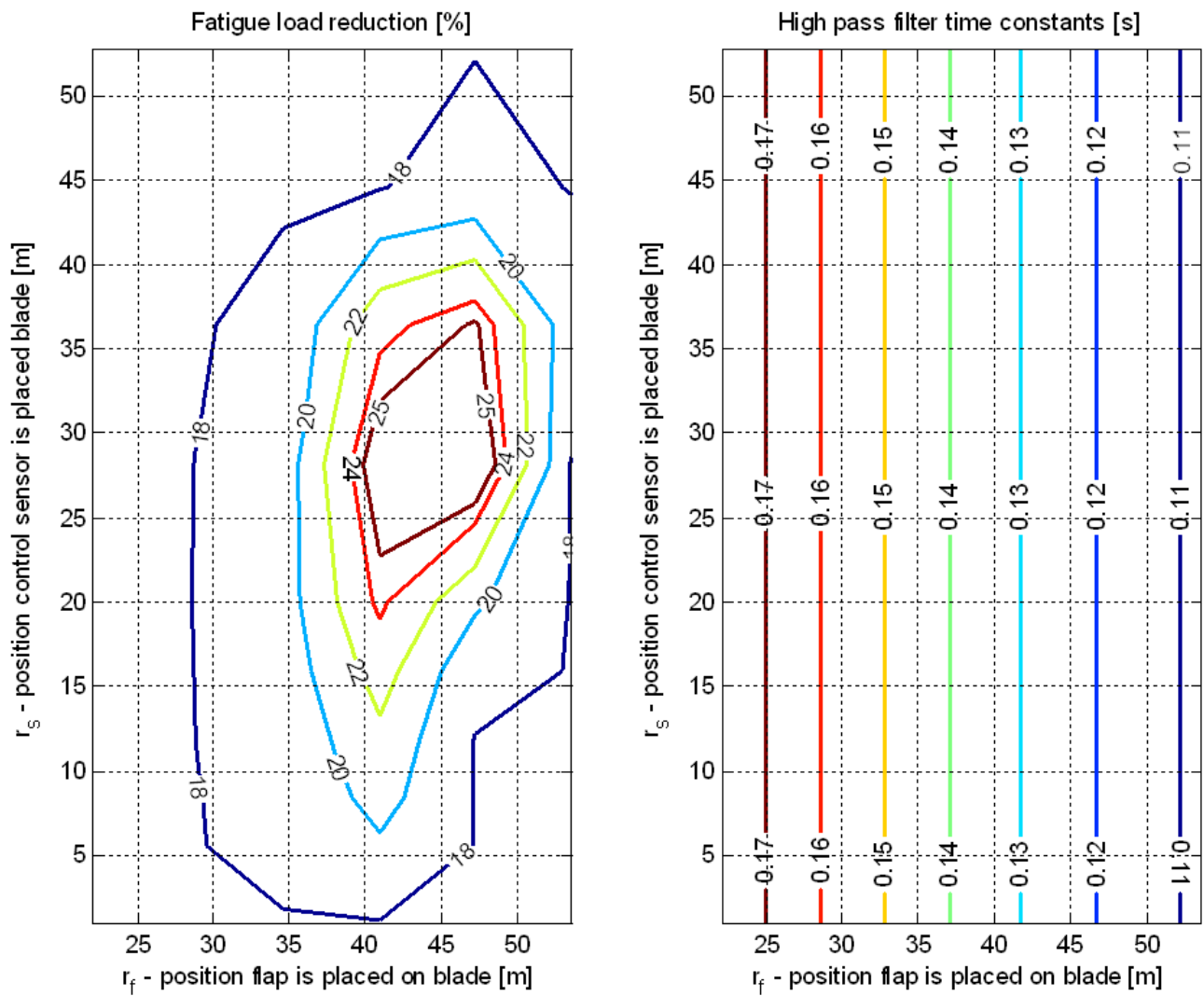


FIGURE 19 (LEFT) FATIGUE LOAD REDUCTION AS FUNCTION OF CONTROL SENSOR AND FLAP POSITION (RIGHT) HIGH FREQUENCY FILTER TIME CONSTANT FROM EQUATION (65).

It is well known that a particular mode shape has a corresponding eigenfrequency. This leads to the next investigation, similar to the prior, with the exception that the high frequency pass filter time constant, τ , is optimized along with the control gains.

Figure 20 illustrates a parameter sweep of r_f and r_s while optimizing K_P and τ . When comparing Figure 19 to Figure 20 three features are distinctive; when optimizing τ it becomes an intricate function of both r_f and r_s , the control sensor near the blade root moment gives high load reductions, and the high fatigue load reductions is no longer restricted to a narrow region near the center of the blade. This leads to two possibilities when designing which frequencies the flap should react to; either by moving the sensor along the blade or by adjusting the high frequency pass filter time constant.

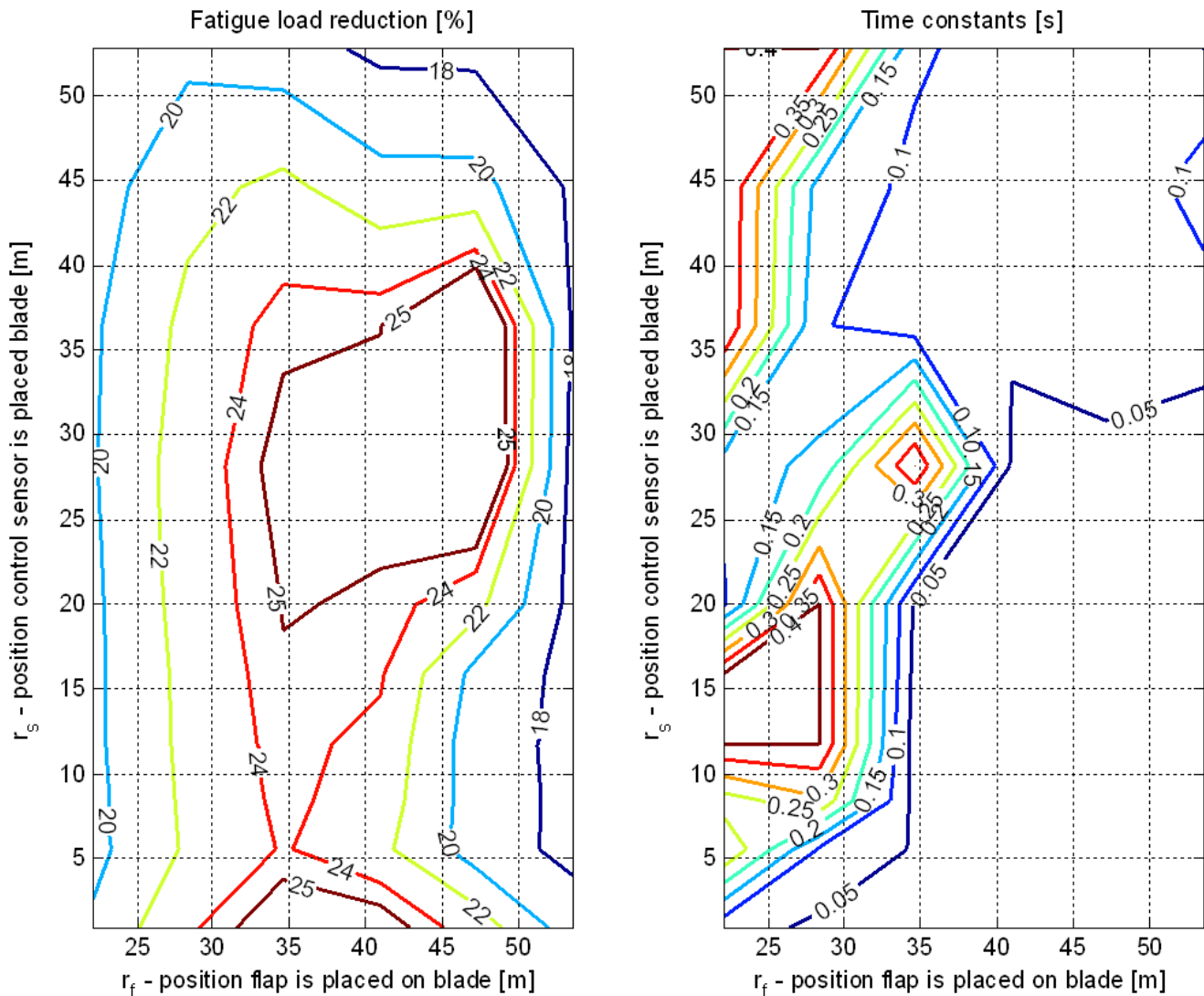


FIGURE 20 (LEFT) FATIGUE LOAD REDUCTION AS FUNCTION OF CONTROL SENSOR AND FLAP POSITION (RIGHT) OPTIMIZED HIGH FREQUENCY FILTER TIME CONSTANT.

Not all time constants are valid and not all sensor positions yield good results. In fact only two sensor regions (blade root and around the center of the blade) offers high load reductions. However, there is some flexibility when choosing sensor position and time constant. The optimization tends to place the sensor closer towards the blade root, when large time constants are used. As the time constant increase the frequency band is widened allowing more low frequency content in the input signal.

It might be possible to tune K_P and τ on a real turbine but depending on the control authority of the flap(s) safety and the ability to identify faults in the system should be considered along with procedures for shutting down the active flap control in this event.

The optimization has fatigue load reductions in the flapwise blade root moment in focus. It is important to see how the optimization affects other parameters like power production, flap activity etc. The effect on power production by use of flap control is investigated in Chapter 3.4, whereas Figure 21 illustrates the level of flap activity for the various blade positions of the sensor and flap using the standard deviation in flap deflection for the simulated time series.

The flap activity diminishes near the blade root region when using tuned filter time constants which is an interesting bonus and not part of the optimization objective. It is not surprising that the flap deflection amplitude increases, thus the standard deviation, near the blade root because the normal force is proportional the relative wind speed squared, but it is perhaps surprising to see just how complex the relation between the best performing filter time constant and r_f , r_s is in Figure 20. The flap position on the wind turbine blade giving the highest fatigue load reduction is investigated for blades that are elastic in flapwise, edgewise and torsional directions. For the elastic blade the flap should be placed closed to 45 meters from the blade root, see Figure 19, if filter time constants became a free optimization parameter the r_f , r_s zone for best performing fatigue load reductions widens, see Figure 20. The flap mounted on the stiff blade reduced the blade root moment fatigue by 17%, and for the fully elastic blade the reduction was 25%. This is a perfect example of just how intricate the dependencies are, although the proposed controller is simple, the optimization problem is not.

An intuitive subsequent step after mounting one flap on a wind turbine blade is to investigate the effect of having multiple flaps per blade. Initial investigations by Andersen [49] [59] revealed that additional flaps gave a decrease in fatigue loads. Two and three flaps per blade with corresponding strain gauge sensors were investigated, keeping the same setup as for the single flap per blade. For two flaps per blade the optimization needed to tune 2x4 parameters, more specifically each of the two flaps needed to tune the position of the control sensor, the flap itself, the filtered time constant and the gain. For three flaps per blade 3x4 parameters needed to be tuned, again with the same number of parameters per blade. The first thing to notice is the fact that although one flap gives a 25% fatigue load reduction, two flaps are far from giving 50%, in fact only 34% is achieved. Finally, adding the third flap per blade yields even less in terms of fatigue load reduction. Table 2 gives an overview of the set of gains, time constants, flap, and control sensor blade positions, yielding the highest fatigue load reductions in the flapwise blade root bending moment. The flap activity levels needed to facilitate these reductions are also part of the table and can be seen the standard deviation in flap deflection row. Although the loads are not significantly decreased when using three flaps per blade instead of one, the flap activity level is decreased, which could be useful knowledge for future smart rotor blade designs.

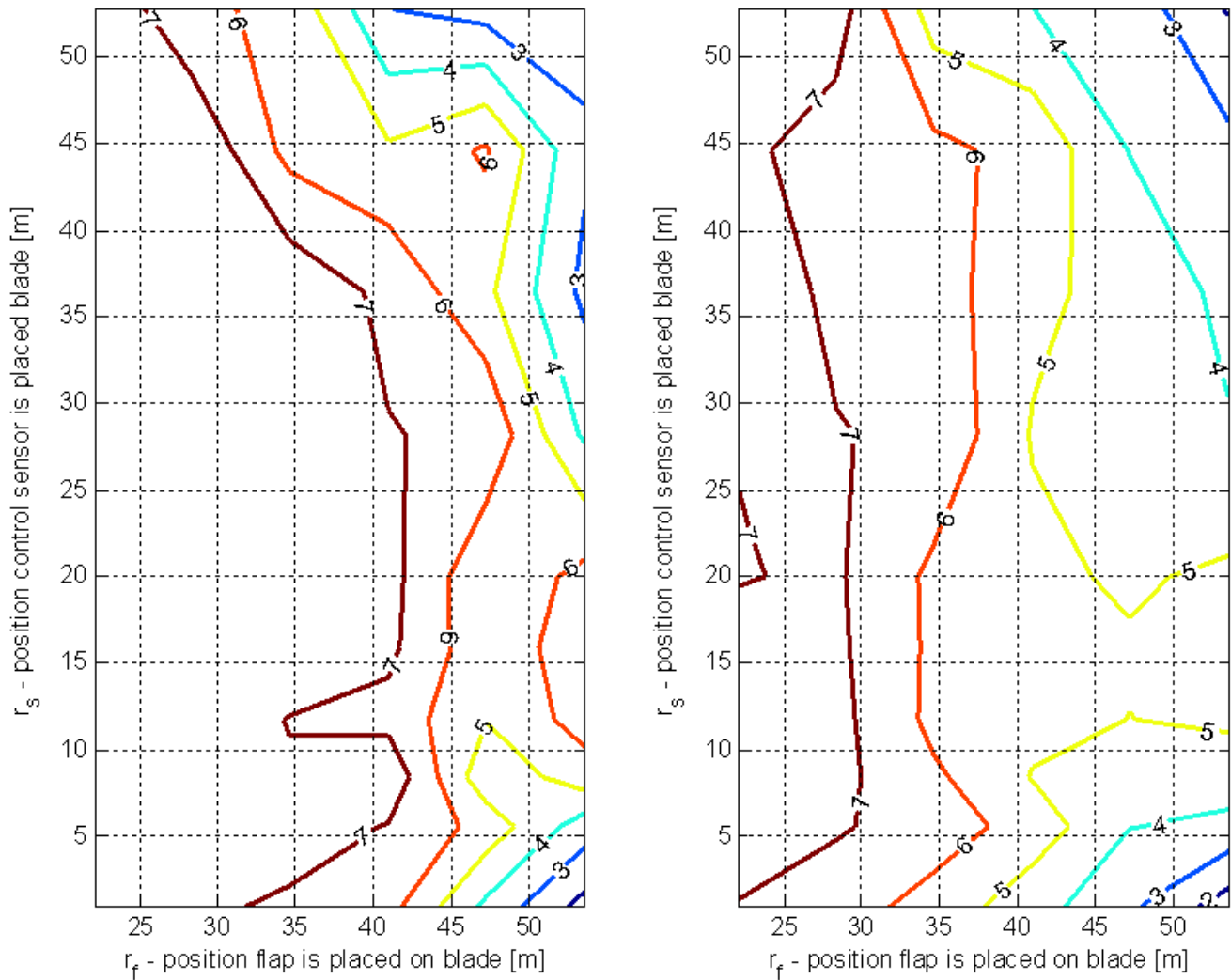


FIGURE 21 FLAP ACTIVITY ILLUSTRATED USING THE STANDARD DEVIATION OF THE FLAP DEFLECTION SIGNAL (LEFT) CONTROL BASED ON UNTUNED TIME CONSTANTS (RIGHT) SAME BUT CONTROL IS BASED ON OPTIMIZED TIME CONSTANTS.

TABLE 2 LOAD REDUCTION, ACTUATOR AND SENSOR POSITION, GAIN AND TIME CONSTANTS FOR ONE, TWO AND THREE FLAPS PER WIND TURBINE BLADE

	One flap,6m	Two flaps per blade,12m		Three flaps per blade,19m		
	#1	#1	#2	#1	#2	#3
Mean flap pos r_f [m]	45	34	45	30	45	54
Sensor pos r_s [m]	28	20	28	20	28	36
K_p [deg·KNm ⁻¹] / τ [s]	0.044/ 0.05	0.071/ 0.32	0.032/ 0.04	0.060/ 0.35	0.034/ 0.10	0.025/ 0.03
Standard deviation flap deflection [deg]	4.9	4.2	3.8	3.7	3.4	2.1
Fatigue reduction	25%	34%		37%		

The effect of having additional delays in the control signal was also investigated. It should be noted that no attempt was made to re-optimize the controller after signal delays and lags were introduced. Figure 22 show that the proposed controller is more sensitive to a signal delay than a signal lag. For the delayed signal the flaps have no effect after 200 ms, typically delays in signals originates from hardware and 200ms is substantial in this context. The same drastic reduction of the load reduction potential is not seen for the signal lag, in which the signal delay is modeled as a first order filter. What remains to be investigated is the effect of having a differential term in the control and more far reaching designing the controller to react to the aerodynamic input for instance in the form of a Pitot tube, rather than the elastic response in the form of a simulated strain measurement.

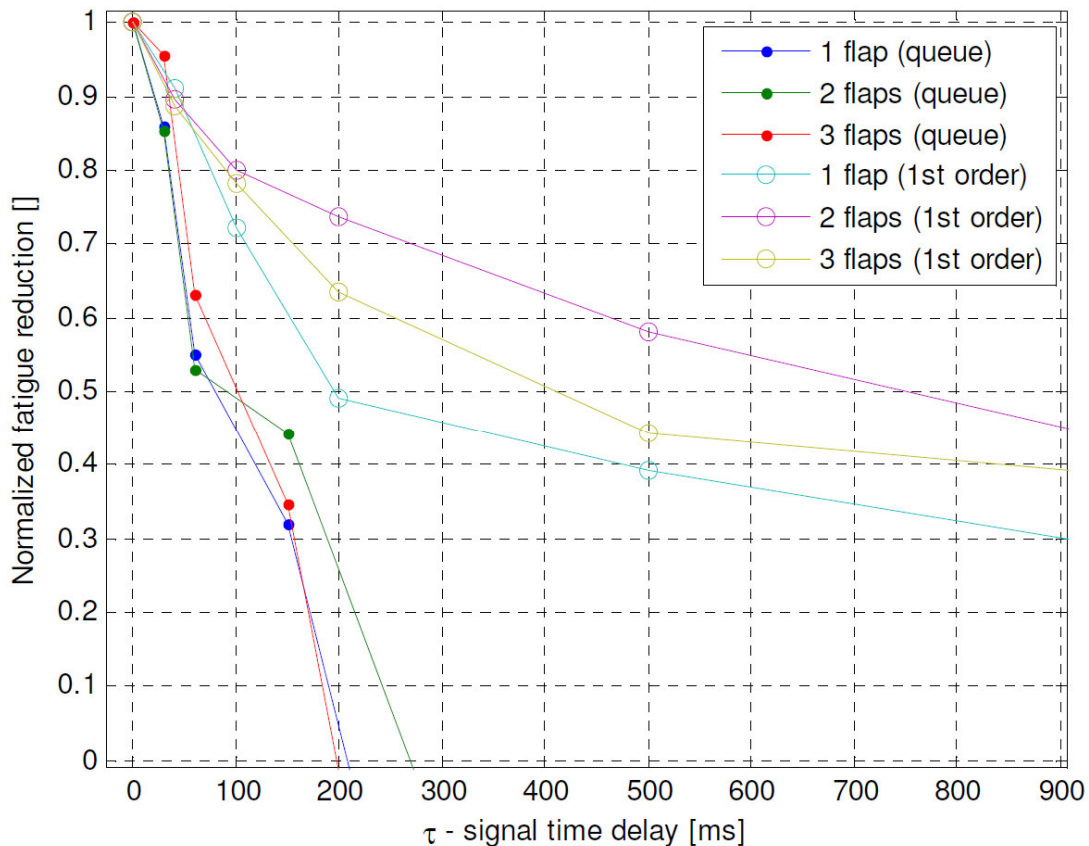


FIGURE 22 LOAD REDUCTION AFFECTED BY A DIRECTLY DELAYED SIGNAL (QUEUE) AND FIRST ORDER DELAYED (1ST ORDER).

When using strain gauges or other types of gauges the effect of signal noise will play a role in the performance of the controller. The effect of adding signal noise to the control signal has been investigated. The definition of the signal noise is provided in the previous subsection with model descriptions. In Figure 23 the fatigue load reduction is shown as function of the Signal to Noise Ratio (SNR), more specifically the 1dB, 2dB, 3dB, 4dB, 5dB and 10dB ratios have been investigated, where 10dB is the least affected signal and 1dB the most deteriorated signal. The investigation shows that once the SNR drops below 3dB the reduction potential starts deteriorating significantly. Furthermore, if

SNR is below 1dB the flaps should not be used with the present controller. Although this is a crude investigation and the noise remains to be combined with e.g. signal delays, typical SNR for strain gauges are well above 3dB which suggest a signal noise investigation for this type of controller could be a second priority. The controller was not re-optimized after adding the white noise; thus, the best performing controller parameters pertaining to the undisturbed signal was kept for cases of signal lag and delay.

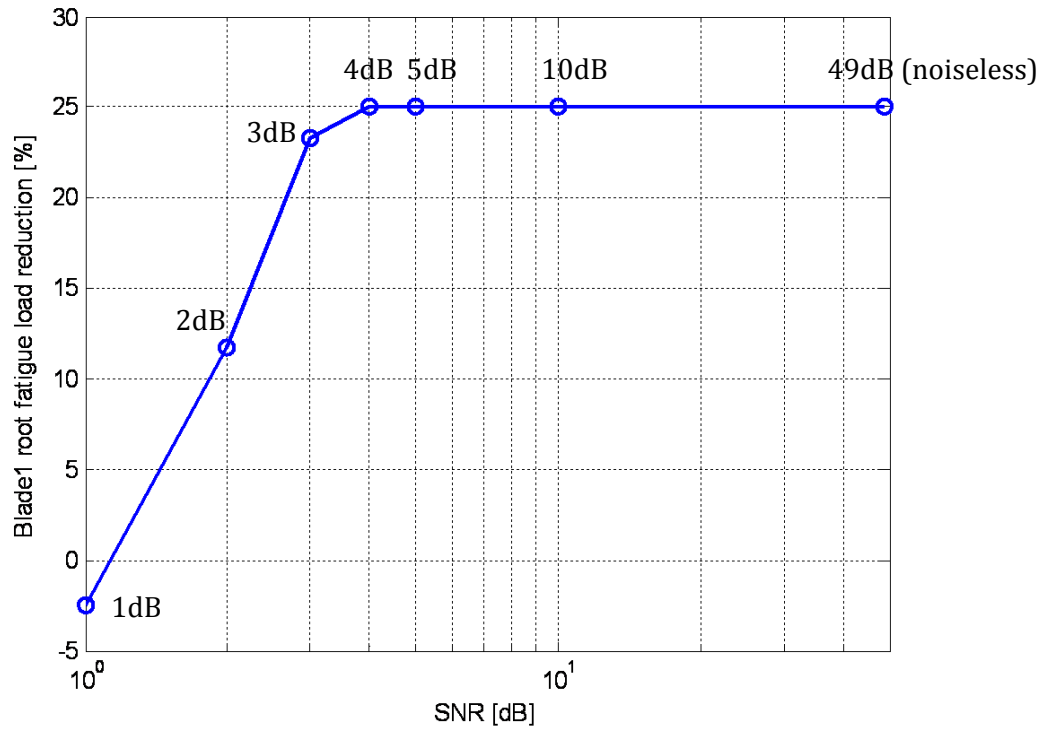


FIGURE 23 EFFECTS OF SIGNAL NOISE ON THE FATIGUE LOAD REDUCTION.

It should be noted that no instabilities were seen during these excitation runs. An interesting investigation to be made as future work is a comparison between the simple control proposed in the current work and more advanced control models.

It is not clear if the flap control suggested for this simulated reference turbine should be used on a real turbine or if the tuning procedure will work on other simulated turbines. These investigations could be part of future work.

3.2.4 CONCLUSION

A controller for the trailing edge flap has been proposed. HAWC2 [25] is used as a component in the control loop design, offering the full pallet of parameters for the optimization routine. A strain sensor is used as input for the flap control. The computations are done on the 5MW reference turbine also used in the EU-project UpWind⁵. The flaps are 6.3 meter long or 10% of the overall blade length. The optimum position for a flap was investigated using blades elastic in flapwise, edgewise and torsional direction. The flap should be placed 45 meters from the blade root and the strains should be measured 28 meters from the blade root. The flap mounted on the stiff blade reduced the blade root moment fatigue by 17%, for the fully elastic blade the reduction was 25%. The elastic part plays a significant role when using these tools to asses fatigue reduction potential and when evaluating control designs. When using optimization routines it is important to have well suited starting guesses. Based on numerous parameter sweeps, Equation (64) for proportional gains is proposed and Equation (65) for residual time constants. The equations should be regarded as suggestions for well suited start guess rather than derived equations based on physics. The effect of placing two and three flaps per blade have been investigated, one flap can reduce the blade root moment fatigue load by 25%, two flaps 34% and three flaps 37%. The effect of adding time lags and time delays in the control signal has been investigated. When a first order time lag is introduced the load reduction potential drop to 50% after a 200ms lag. A directly delayed signal of 200ms is unrealistically big but investigated for the sake of completeness, a control signal put in a delayed 200ms will render the flap(s) useless and above 200ms even harmful for the wind turbine. Signal noise is investigated and has an effect if the signal to noise ratio is lower than 3dB. Load reductions of 25% in blade root moment for individual blade pitch has been reported this should be compared to the 37% load reductions obtained using three flaps per blade. The flap and individual pitch control has not been combined in this investigation.

An interesting future investigation is a comparison between the simple control proposed in the current work and more advanced control models.

In this section the trailing edge flap reacts to the elastic deformation. In the next section a controller based on inflow sensors will be proposed. The obvious benefit of a signal based on inflow measurements as opposed a signal based on elastic deformations is presumable an improved response time from aerodynamic load disturbance to flap response.

3.3 CONTROL BASED ON INFLOW MEASUREMENTS

One of the benefits using flaps on wind turbine blades instead of traditional pitch mechanisms is faster response times. The motivation for the work presented in this section is to investigate the fatigue load reduction potential using inflow measurements which may be better suited for use in the flap actuator. The strain used in last section is caused by aerodynamic loading and requires time to build up, whereas the Pitot tube measures the input that gives rise to the aerodynamic load. An inflow sensor in the form of a Pitot tube has been implemented in HAWC2 [25]. The inflow sensor provides input for the flap controllers proposed in this section. Load reductions are investigated by means of ten minute

⁵ SIXTH FRAMEWORK PROGAMME (FP6), 2009.

Available from Internet <http://www.upwind.eu/> Accessed 17 September 2009.

time series. One, two and three flaps per blade, or 10%, 20% and 30% of the total blade length, have been investigated and each flap has its own inflow sensor.

3.3.1 MODEL

A boom is attached to a blade. The sideslip angle is not considered, only the traditional incidence angle is. The boom is assumed infinitely stiff. Hence, elastic deformation of the boom will not be modeled. The 2D disturbed effect from the blade itself is not included in the modelling here. This disturbance depends on the blade loading. There are indications that this is a fair assumption, Heinz [60] conducted CFD simulations in Ellipsys which showed that the load reduction using a Pitot tube is not reduced significantly, when the Pitot boom is short. Heinz found that this is even the case for a short Pitot tube. The assumption and concept is tested in a wind tunnel using a variable boom length Pitot tube mounted on an airfoil section controlling a deformable trailing edge flap, see Chapter 4.2. In HAWC2 the contribution to the measured incidence angle from the airfoil eigenmotion comes from the elastic axis x_{ea}, y_{ea} and pitch axis x_p, y_p , see Figure 24.

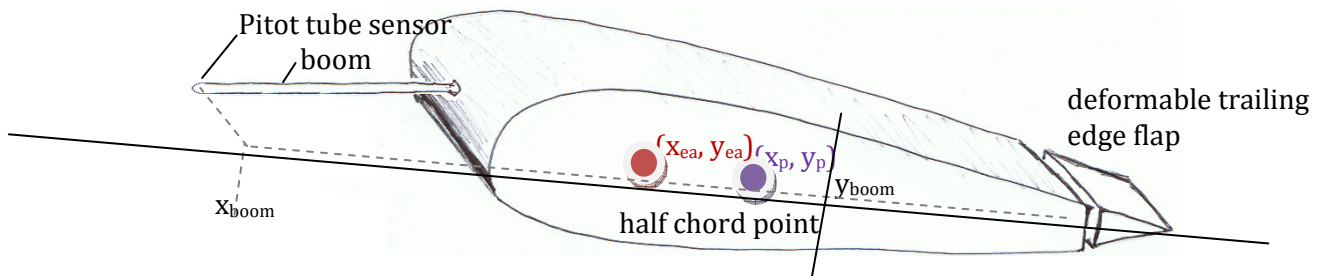


FIGURE 24 BLADE, BOOM AND A PITOT TUBE TO THE CONTROL OF THE DEFORMABLE TRAILING EDGE FLAP.

Apart from the eigenmotion due to elastic torsional deformation rate and the pitch rate the traditional geometric incidence angle is calculated using the interpolated free stream wind speed one boom length upstream.

An initial concern with using a Pitot tube as the only control sensor was that it primarily measures local changes in inflow conditions on the blade. Despite the use of nearwake models and the structural coupling along the spanwise direction of the blade, it was a concern that local gusts away from the Pitot tube would not be captured. This was the motivation for testing two different control algorithms for the Pitot tube. The governing equation for the first control algorithm, f_1 , is based on local inflow sensors from a Pitot tube, the f_2 based controller includes the rotor speed ω sensor. The motivation for using ω in f_2 is that the pure Pitot tube controller f_1 captures aerodynamic fluctuations close the sensor leaving out effects in other areas on the blade. By including the ω sensor in the f_2 controller effects from all three blades are feed into the controller. The basic idea behind the two control algorithms is to keep the lift, L , constant. This is done using a quasi-steady approach

$$f_1(\alpha, \beta, V) = \frac{2L}{\rho c} = \left[\frac{\partial C_L}{\partial \alpha} \alpha + \frac{\partial C_L}{\partial \beta} \beta \right] V^2 - \frac{\partial C_L}{\partial \alpha} \alpha_0 V^2 \quad (66)$$

$$f_2(\alpha, \beta, \omega) = \frac{2L}{\rho c} = \left[\frac{\partial C_L}{\partial \alpha} \alpha + \frac{\partial C_L}{\partial \beta} \beta \right] r_f^2 \omega^2 - \frac{\partial C_L}{\partial \alpha} \alpha_0 r_f^2 \omega^2 \quad (67)$$

ρ is air density and c is chord. The incidence shift for a cambered profile is α_0 . The inflow angle is α , wind speed is V and the flap deflection is β . The mid position of the flap in spanwise blade direction is r_f . The location of the pitot tube is placed at the mid flap position. These variables are all part of the governing equation for the first flap controller, which is found by setting the gradient to the quasi steady lift zero

$$\begin{aligned} \frac{\partial f_1}{\partial \alpha} &= \tilde{V}^2 \frac{\partial C_L}{\partial \alpha} \\ \frac{\partial f_1}{\partial \beta} &= \tilde{V}^2 \frac{\partial C_L}{\partial \beta} \end{aligned} \quad (68)$$

$$\frac{\partial f_1}{\partial V} = 2\tilde{V} \left(\tilde{\alpha} \frac{\partial C_L}{\partial \alpha} + \tilde{\beta} \frac{\partial C_L}{\partial \beta} \right) - 2\tilde{V} \left(\alpha_0 \frac{\partial C_L}{\partial \alpha} \right)$$

the above equations represent gradients to f_1 linearized around $\tilde{\alpha}$, $\tilde{\beta}$ and \tilde{V} which also serve as reference to the control residuals

$$\frac{\partial f_1}{\partial \alpha} (\alpha - \tilde{\alpha}) + \frac{\partial f_1}{\partial \beta} (\beta - \tilde{\beta}) + \frac{\partial f_1}{\partial V} (V - \tilde{V}) = 0 \quad (69)$$

when combined and rewritten

$$\frac{\partial C_L}{\partial \beta} \beta_1 = \left(2 \frac{V}{\tilde{V}} \left(1 - \frac{V}{\tilde{V}} \right) + 1 \right) \left(\tilde{\alpha} \frac{\partial C_L}{\partial \alpha} + \tilde{\beta} \frac{\partial C_L}{\partial \beta} \right) - \alpha \frac{\partial C_L}{\partial \alpha} + 2 \frac{V}{\tilde{V}} \left(\frac{V}{\tilde{V}} - 1 \right) \left(\alpha_0 \frac{\partial C_L}{\partial \alpha} \right) \quad (70)$$

the flap deflection β_1 for f_1 has been derived. The alternative control version f_2 with the rotor speed ω is derived in a similar manner as

$$\frac{\partial C_L}{\partial \beta} \beta_2 = \left(2 \frac{\omega}{\tilde{\omega}} \left(1 - \frac{\omega}{\tilde{\omega}} \right) + 1 \right) \left(\tilde{\alpha} \frac{\partial C_L}{\partial \alpha} + \tilde{\beta} \frac{\partial C_L}{\partial \beta} \right) - \alpha \frac{\partial C_L}{\partial \alpha} + 2 \frac{\omega}{\tilde{\omega}} \left(\frac{\omega}{\tilde{\omega}} - 1 \right) \left(\alpha_0 \frac{\partial C_L}{\partial \alpha} \right) \quad (71)$$

where zero wind speed and zero rotor speed should be avoided in order not to divide by zero. The variables $\tilde{\alpha}$, $\tilde{\beta}$, \tilde{V} , $\tilde{\omega}$ represents the point of linearization, these are subject to low pass filtering when introduced in HAWC2. To avoid writing up many similar equations the filtered values are indexed and the letter w_i is used to represent them

$$\tau \frac{\partial w_i}{\partial t} + w_i = [\alpha(t) \quad V(t) \quad \omega(t) \quad \beta(t)]^T \quad (72)$$

$$[w_1 \ w_2 \ w_3 \ w_4]^T = [\tilde{\alpha} \ \tilde{v} \ \tilde{\omega} \ \tilde{\beta}]^T \quad (73)$$

The time constant τ has to be determined for each controller for each of the turbines operation states.

3.3.2 SETUP OF CASES

The boom is given as an input value from the half chord point in HAWC2 also shown in Figure 24. The boom has length of 1.5 times the max chord height which is a value suggested in the work of McFadden et al [61] for mounting Pitot tubes on airplane wings and fuselages.

Tower shadow and wind shear is included. The equivalent fatigue load reduction in the flapwise blade root moment is investigated for turbulent wind at 10m/s in mean wind speed. The deformable trailing edge flap sections are 10% of the total blade length or 6.3 meter long.

The first investigation evaluates the f_1 controller at 60% and 90% rated rotor speed. The second investigation evaluates the f_2 controller at 60% and 90% rated rotor speed. The third investigation uses the f_2 controller for two and three flaps per blade at 90% rotor speed.

3.3.3 RESULTS AND DISCUSSION

Parameter sweeps of Pitot/flap position and time constants is conducted in Figure 25 and Figure 26 while calculating the equivalent flapwise blade root fatigue load reduction.

The **first investigation** uses a single flap 6.3 meters long 10% blade length and the f_1 based flap controller setup. In Figure 25 the 23% reduction is obtained when a -3dB cutoff frequency of $1/(2\pi 10s)=0.018\text{Hz}$ is used for the low pass filter which determines the magnitude of the residuals; $\tilde{\alpha}$, \tilde{v} , $\tilde{\omega}$, $\tilde{\beta}$.

At 90% rated rotor speed the flap and inflow sensor should be placed 45 meters from the blade root. At 60% rated rotor speed the flap should be placed 50-55 meters from the blade root.

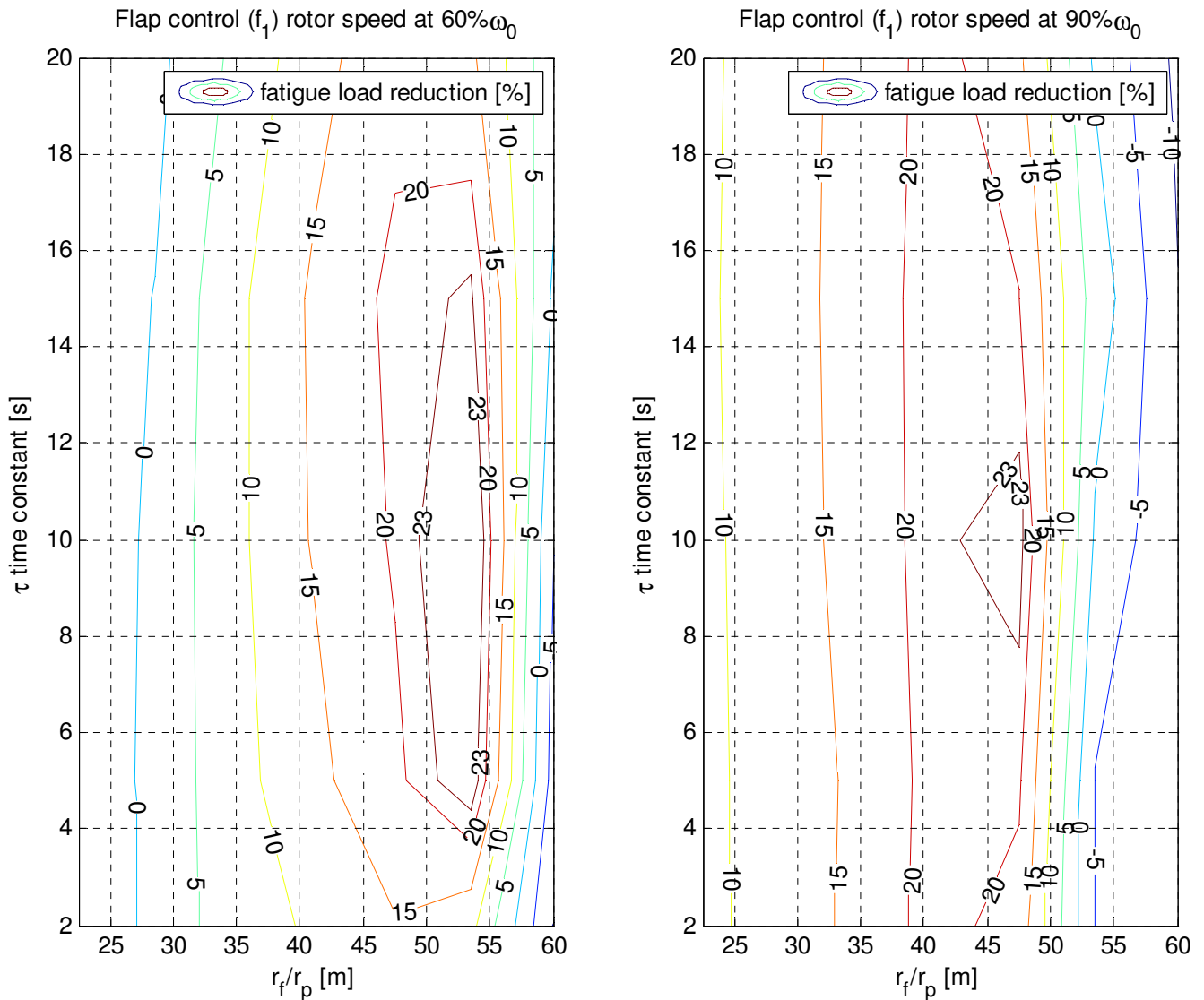


FIGURE 25 REDUCTIONS IN THE FATIGUE LOADS IN THE BLADE FLAPWISE ROOT MOMENT AS FUNCTION OF FLAP POSITIONS AND FILTER TIME CONSTANTS FOR THE f_1 FLAP CONTROLLER.

The moment is decreased with the square of the relative wind speed, while the torsional stiffness of the blade remains the same. For a torsionally stiff blade the optimal position to place the flap follows the maximum normal force in radial blade direction well. For a blade with less torsional stiffness the optimal position for the flap moves towards the blade root, see Andersen et al. [22]. It may be possible to reverse this trend if the torsional deflection becomes a part of the control model.

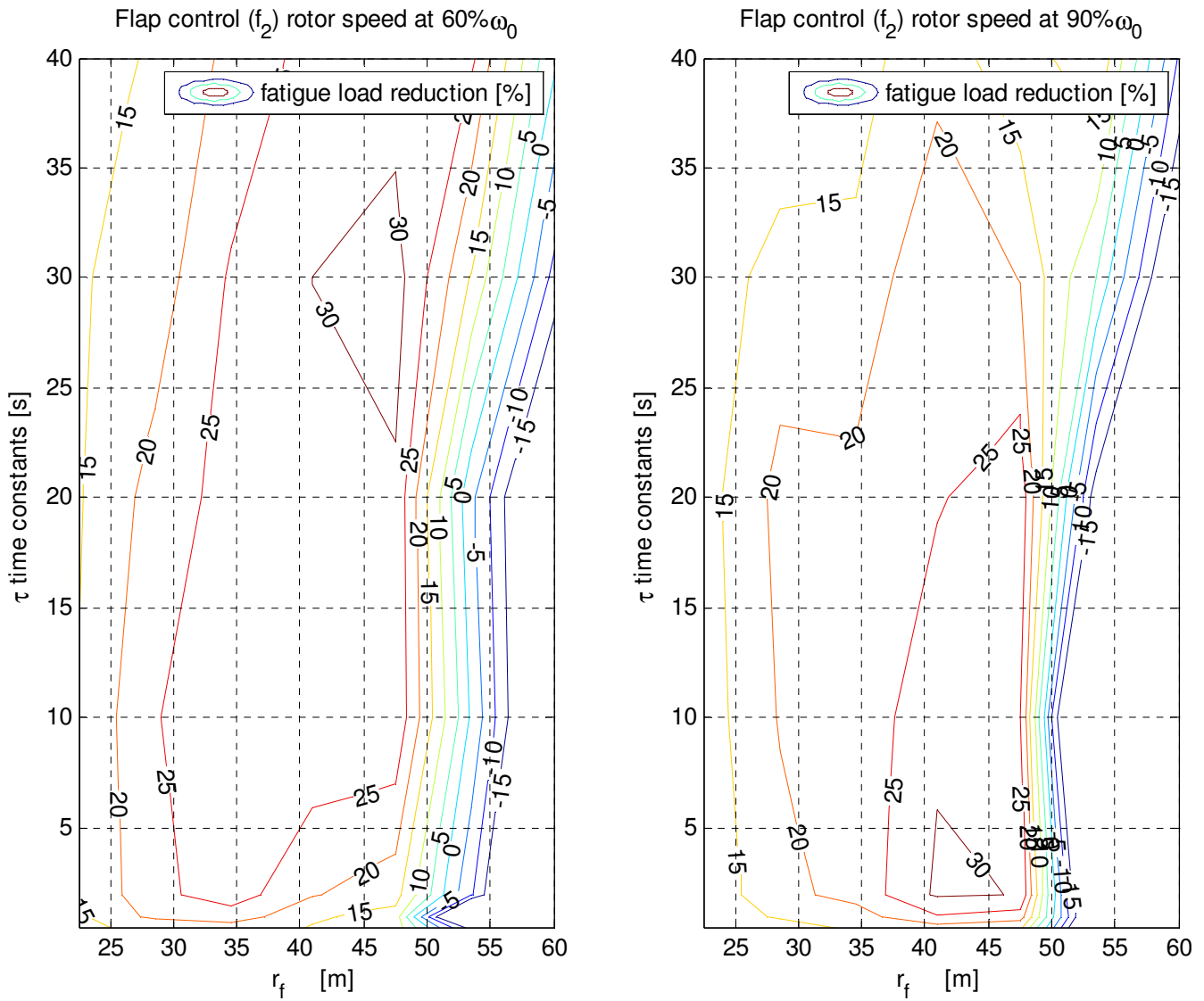


FIGURE 26 REDUCTIONS IN THE FATIGUE LOADS IN THE BLADE FLAPWISE ROOT MOMENT AS FUNCTION OF FLAP POSITIONS AND FILTER TIME CONSTANTS FOR THE f_2 FLAP CONTROLLER.

The **second investigation** uses the f_2 controller setup again with a single flap 6.3 meters long. In Figure 26 fatigue load reductions of 30% is obtained for a sensor and a flap placed 41-46 meters from the blade root for 90% rated rotor speed and 42-48 meters for 60% rated rotor speed. The time constant τ is a function of the rotor speed: $\tau=30s$ at 60% rated rotor speed and $\tau=4s$ at 90%. Typically the low frequencies contain the most energy. By adding a sensor which captures these frequencies well the flap will respond to these low frequency rotor speed variations, see Figure 27.

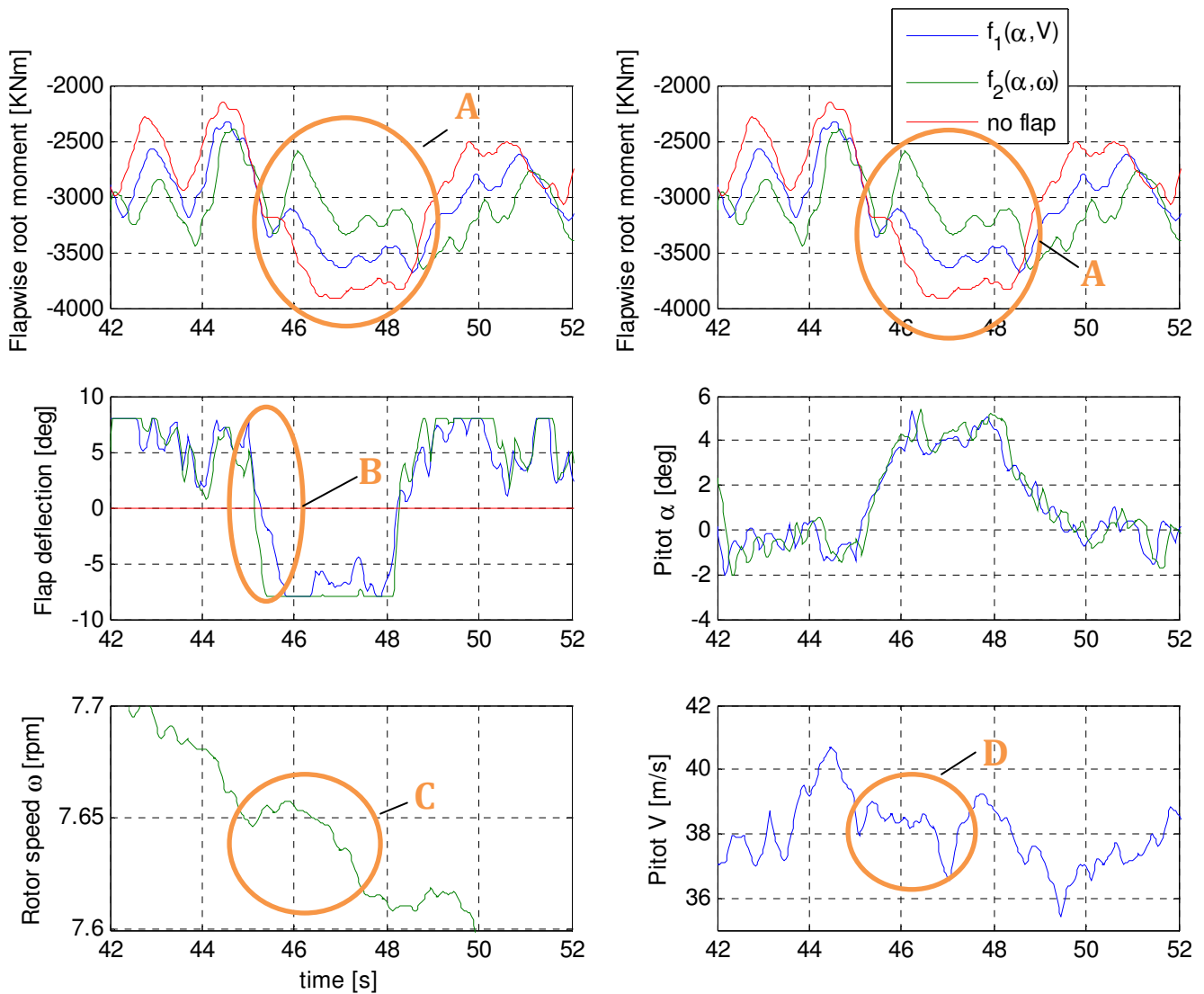


FIGURE 27 ILLUSTRATION OF FLAPWISE BLADE ROOT MOMENT AND FLAP DEFLECTION TIME SERIES COMPARISON BETWEEN NO FLAP AND THE TWO FLAP CONTROLLERS, INCLUDING THE ROTOR SPEED, PITOT INCIDENCE AND RELATIVE WIND SPEED SENSORS.

Notice in Figure 27 **(A)** the increase in blade root moment from $t=46\text{s}$ to $t=48\text{s}$ for both the *no-flap* and the f_1 controlled cases. The f_2 controlled case in **(A)** keeps a smoother green curve closer to a mean root moment from $t=46\text{s}$ to $t=48\text{s}$. The flap deflection **(B)** moves towards negative deflections faster for f_2 at $t=45\text{s}$ and it also stays at a near constant maximum negative deflection from $t=46\text{s}$ to $t=48\text{s}$ which is needed in order to maintain a smoother development in the blade root moment. The difference in sensor input between f_1 and f_2 can be seen in **(C)** and **(D)**. The Pitot tube **(D)** mounted locally on the blade does not capture the increase in thrust starting at $t=45\text{s}$ as well as the rotor speed sensor does **(C)**. Therefore the flap deflects faster for f_2 at **(B)** lowering the flapwise root moment in **(A)**. As part of future work it could be interesting to see how well a flap controller purely based on rotor speed performs.

The f_2 controller is reused in a **third investigation** where two and three flaps were used per blade instead of a single flap per blade. For three 6.3 meter long trailing edge flaps the same fatigue load reduction is 40% which is only 10% better than the single flap setup, depending on the cost of producing flap, sensor, transducers, data converters etc. it may be a lot to pay cost/benefit wise.

TABLE 3 LOAD REDUCTIONS, ACTUATOR AND SENSOR POSITION FOR ONE, TWO AND THREE FLAPS PER WIND TURBINE BLADE

	One flap 6.3m	Two flaps per blade 12m		Three flaps per blade, 19m		
	#1	#1	#2	#1	#2	#3
Pitot tube, flap [m]	44	34	46	30	43	54
Fatigue reduction	30%	37%		40%		

One flap can alleviate 30% fatigue loads the second flap only contributes with 7% and the third only an additional 3% extra compared to two flaps. It works well when combining different types of sensors like α and ω sensors in f_2 . This should be investigated further perhaps using other types of sensors like the strain gauge sensors. It may be possible to increase the effect of adding the second and third flap per blade.

3.3.4 CONCLUSION

A Pitot tube sensor type was implemented in HAWC2. The control based on incidence and relative wind speed from the Pitot type gave 23% load reduction for single flap. The flap had a length of 10% of the total blade length. An alternative controller based on the rotor speed sensor was tested; it gave 30% fatigue load reduction. The fact that the alternative controller based on the combination of various sensors performed 7% better fatigue load reduction wise pointed in the direction of looking into combining several sensors for the flap control, hence the motivation for the next section. Two and three flaps per blade using the alternative control version was also investigated, three flaps with a total length of 19 meters gave 40% fatigue load reduction in the flapwise blade root moment.

3.4 CONTROL BASED ON COMBINED SENSORS

In the previously chapter the turbulent mean wind speed was 10m/s and the controllers used either the strain sensors input or the Pitot measurements to control the flap. In the current work the two types of sensors will be combined in an effort to see if the reduction potential can be increased and other objectives such as power optimization in the constant tip-speed region for low wind speeds can be reached.

3.4.1 MODEL

In the current work two types of sensors are used to control the deformable trailing edge flaps. Where one is measuring the blade root moment, the other measures the local inflow, presumably using Pitot tubes, see Figure 28. Numerous studies focused on optimal placement, length and number of flaps for a blade. In the current work one, three and as much as five deformable trailing edge flaps per blade is used. The flaps are individually controlled.

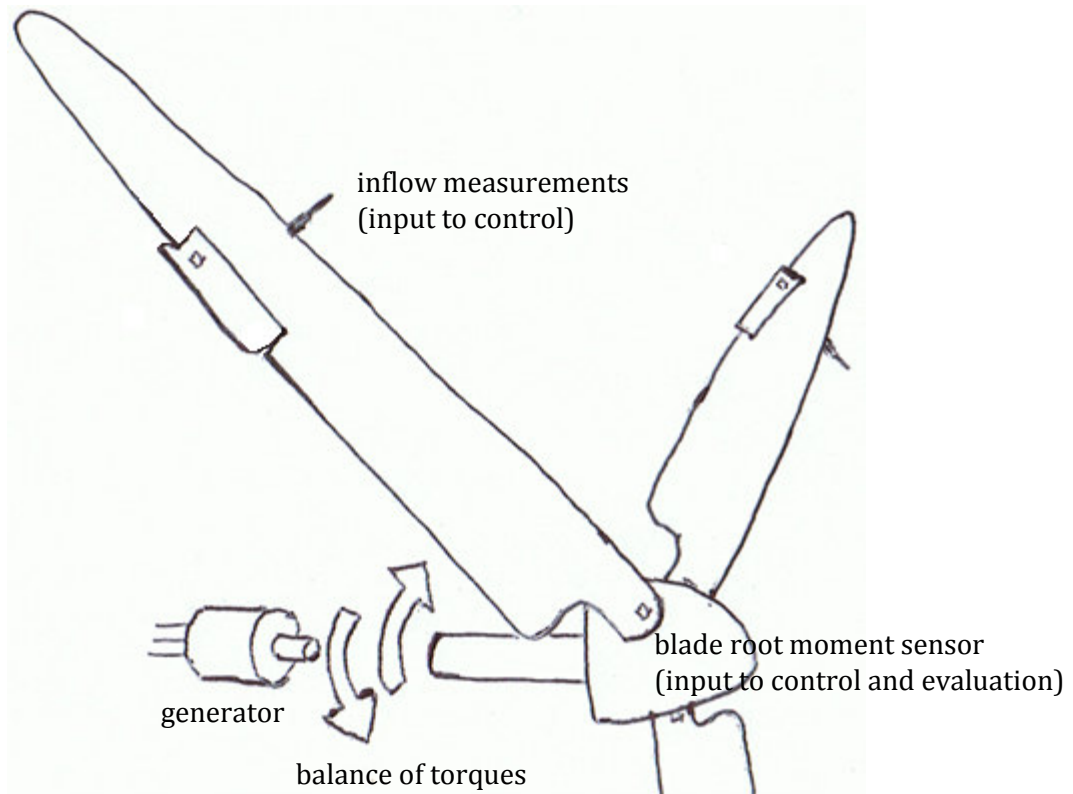


FIGURE 28 WIND TURBINE ACTUATORS AND SENSORS.

An overview of the control model will briefly be described below. Further details can be found in by Andersen et al [50]. The pitch and generator servo is modeled as a first order system. It is important to avoid high frequency drive train vibration especially the free-free drive train vibration, which is accomplished by applying a low pass filter on the rotor speed control sensor, see Figure 29. The sensitivity in the driving force with respect to pitch changes is not a constant. Therefore, pitch gain scheduling is used; see Hansen et al [62].

The flap controller reacts to changes in inflow, structural deformations and pitch motion. The contribution to the overall flap deformation from strain, Pitot tube and pitch is determined by a mixing rule. Although the overall aim is to use the pitch to handle low frequency rotor scale aerodynamics and the deformable trailing edge flaps to handle high frequency fluctuations locally on the blade, the different radial blade positions have different distinct features suitable for different combinations of flap actuators and control sensor input.

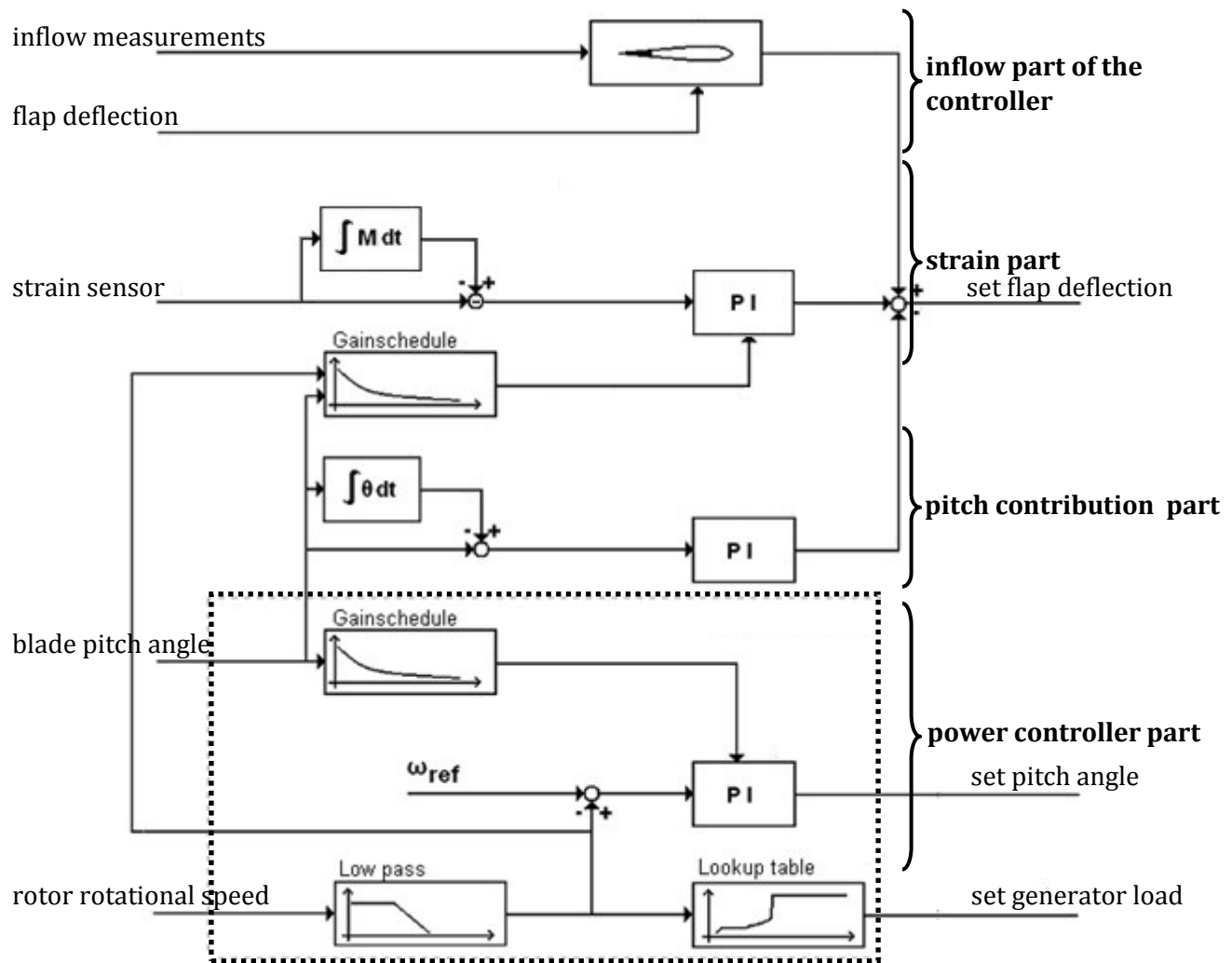


FIGURE 29 CONTROL DIAGRAM.

The **inflow part** of the flap controller is derived from the traditional blade element momentum theory, in which the aerodynamics is simplified by dividing a blade into a number of 2D cross sections.

The **strain part** of the controller consists of a filter and a gain very similar to what is described in Section 3.2.

The **pitch contribution** is taken into account in order to avoid that the flap counter-reacts the pitching motion, putting even more strain on the pitch servo.

A collective pitch mechanism is part of the traditional **power controller** which forms the foundation for the total wind turbine regulation. The traditional controller is taken from the work of Hansen et al [62] where the controller is build around a regulator which actuates the blade pitch using the rotational speed of the high speed shaft as input. In the work of Buhl & Andersen [63], the collective pitch is replaced by a cyclic pitch which works together with the current proposed deformable trailing edge flap controller.

Behind each commercial rotor a blueprint for the blade exists in the form of a given planform which again use a series of airfoils. The design of airfoil characteristics form a complex matrix of properties of which some are in conflict with others. Direct methods are basically interdisciplinary and multi-point and they allow direct use of integrated response parameters such as airfoil C_L and C_D directly as design objectives. In some cases the design incidence region is close to maximum C_L which gives lower rotor solidity. It is assumed that the designed incidence regions yields the highest power output, however, because of the stochastic nature of the wind, turbulence gusts and wind direction changes will always lead to some off-design operation due to non uniform inflow. For low wind speeds, at constant tip-speed, the flap control is designed to also target the local optimum load in an effort to extract the most power from the wind. When this control objective is active, the power optimization coefficient K_α is greater than 0. K_α is only in effect at the low wind speeds in the constant tip speed region.

3.4.2 SETUP OF CASES

Parameters like length scales and shear distortion for the turbulence is provided by IEC61400-1 and will be used at three different mean wind speeds 7m/s, 11m/s and 18m/s, with turbulence intensity at 14-18%. Ten minute turbulence time series based on Gaussian homogenous coherence cross-spectral models for the Shimozuka algorithms implemented in the Mann turbulence model is used. In all cases no yaw misalignment is used. Wind shear with a power coefficient of 0.14 seen at Høvsøre [64] is part of the simulation along with a potential tower shadow model.

The pitch speed is restricted a maximum of 8 °per second.

The flaps have no constraints on deflection rate. Experiments described in Chapter 4 have showed that the assumption not modelling the dynamics the actuator for piezoelectric materials is valid. For other flap prototypes this may not be so.

Combinations of 1, 3 and 5 flaps configurations per blade are tested see Table 4.

TABLE 4 FLAP CONFIGURATIONS TESTED WITH RESPECTIVE LENGH AND POSITION ON BLADE

	1 flap per blade	3 flaps per blade	5 flaps per blade
first flap	44.1-50.4m	26.9-33.2m	24.7-39.4m
second flap		39.9-46.2m	39.4-44.7m
third flap		50.9-57.2m	44.7-53.2m
fourth flap			53.2-59.3m
fifth flap			59.3-62.4m
Percent of total blade with flap	10%	30%	60%

3.4.3 RESULTS AND DISCUSSION

The model required numerous simulations, sweeping parameters and tuning gains and time constants similar to what has been described in the previous two sections using the Simplex algorithm [41]. The initial guess for time constants used for the Pitot tube or the strain sensor has been described in sections 3.3 and 3.2.

The 7m/s average turbulent wind case is shown in Figure 30. The controller operates in the variable speed region where pitching activity is zero.

The effect of using the power optimization coefficient is tested for this low wind speed case, using simulations. The first simulation does not target optimum power production only load reduction, hence $K_{\alpha}=0$ is shown in Figure 30 using the green line. The second simulation use $K_{\alpha}=1$ which mean the controller targets the optimal thrust and axial induction by using the designed incidence, which according to steady blade element momentum theory ensures optimal aerodynamic power conversion. This is shown in Figure 30 using the red line and the original controller is shown in blue.

Even though there is an increased power production at the expense of a slightly higher mean thrust, shown in Figure 30, the overall load reduction potential is still favorable when using flaps compared to the original pitch regulated power controller. According to Table 5 there is an increase in mean power production of 1% at 7m/s. Simulations indicate a decrease in load reductions for the $K_{\alpha}=1$ case compared to the $K_{\alpha}=0$ case. There is some tradeoff between power and load optimization, although both can be improved with the use of trailing edge flaps.

For comparison results with mean turbulent free wind speeds at hub height of 7m/s, 11m/s and 18m/s is shown in Table 5. Results at 7m/s mean wind speed is shown without and with the power optimized controller.

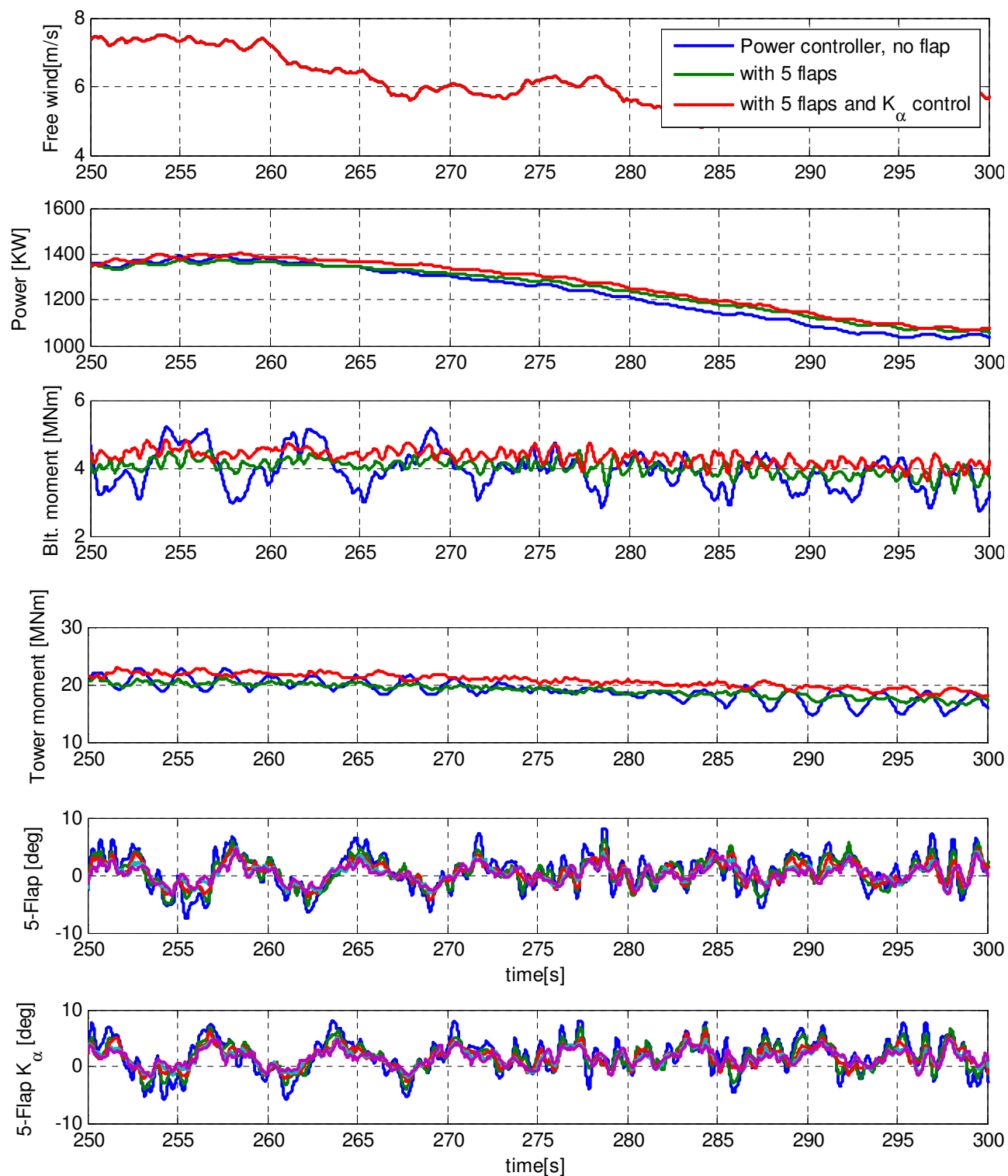


FIGURE 30 (FROM TOP DOWN) FREE WIND SPEED AT HUB HEIGHT, ELECTRICAL POWER, FLAPWISE BLADE ROOT MOMENT, TOWER ROOT MOMENT IN FLOWWISE DIRECTION, FLAP DEFLECTIONS WITHOUT POWER OPTIMIZATION AND WITH POWER OPTIMIZATION.

TABLE 5 COLLECTIVE PITCH RESULTS FOR COMBINED SENSOR CONTROL BASED ON 10 MINUTE TIME SERIES USING ONE, THREE AND FIVE FLAPS PER BLADE OR 10%,30% AND 60% OF BLADE LENGTH.

			<7m/s> $K_a = 0$	<7m/s> $K_a = 1$	<11m/s>	<18m/s>
Blade1, flapwise root moment	0 flap	[KNm]	1983	1983	4481	7662
	1 flap	[KNm]	1620 (18%)	1632(18%)	3101 (31%)	5913(23%)
	3 flaps	[KNm]	1151 (42%)	1184(40%)	2637 (41%)	4997(34%)
	5 flaps	[KNm]	1044 (47%)	1072(46%)	2570 (43%)	4429(42%)
Blade1, edgewise root moment	0 flap	[KNm]	5994	5994	6588	7074
	1 flap	[KNm]	5997 (0%)	6019(-0.4)	6525 (0.9%)	7099 (0%)
	3 flaps	[KNm]	6039 (-0.7%)	6042(-0.8)	6554 (0.5%)	7085 (0%)
	5 flaps	[KNm]	6005 (-0.2%)	6009(-0.2)	6745 (-2%)	7029 (0%)
Blade1, torsion root	0 flap	[KNm]	79.5	79.5	162.7	181
	5 flaps	[KNm]	80.0 (-0.6%)	82.2(-3%)	164.3 (-1%)	141 (22%)
Tilt moment	0 flap	[KNm]	1335	1335	2639	4615
	5 flaps	[KNm]	674 (50%)	647 (52%)	1460 (45%)	2368(49%)
Yaw moment	0 flap	[KNm]	1355	1355	2848	4984
	5 flaps	[KNm]	811 (40%)	763 (44%)	1554 (45%)	2575(48%)
Tower, flowwise root moment	0 flap	[KNm]	3752	3752	6558	11770
	5 flaps	[KNm]	2315(38%)	2380 (36%)	5113 (22%)	8855(25%)
Pitch rate - 1 flap	<i>% reduction</i>	[%]	-	-	1.8%	3.4%
Pitch rate - 3 flaps	<i>in standard</i>	[%]	-	-	6.8%	10%
Pitch rate - 5 flaps	<i>deviation</i>	[%]	-	-	18%	34%
Mean power prod. 0 flap		[KW]	1191	1191	4694	4991
Mean power prod. 1 flap		[KW]	1184 (-0.5%)	1199(+0.7)	-	-
Mean power prod. 3 flaps		[KW]	1183 (-0.7%)	1202(+0.9)	-	-
Mean power prod. 5 flaps		[KW]	1181 (-0.8%)	1204(+1%)	4682(-0.2)	5000(+0.2)

At 11m/s mean turbulent wind using one 6.3 meter long flap, the fatigue load in flapwise blade root moment is reduced 31%. For three flaps per blade the load reduction is 41%. The fatigue in the flapwise blade root moment is decreased 42% for 18m/s when using five flaps per blade. For all wind speeds the proposed controller show significant fatigue reductions for both blade flapwise and tower flowwise root moments.

The rate of pitching for the flap controllers are compared to the controller without flaps. In general the rate of pitching is decreased when using flaps, especially for high wind speeds.

Fatigue load reduction in tilt and yaw moments are also significant. Reductions are ranging from 40% - 50% for all three mean turbulent wind speeds investigated. Results are presented in Table 5 for the 5 flap case and a zoom of the time series from t=500s to t=600s can be seen in Figure 31.

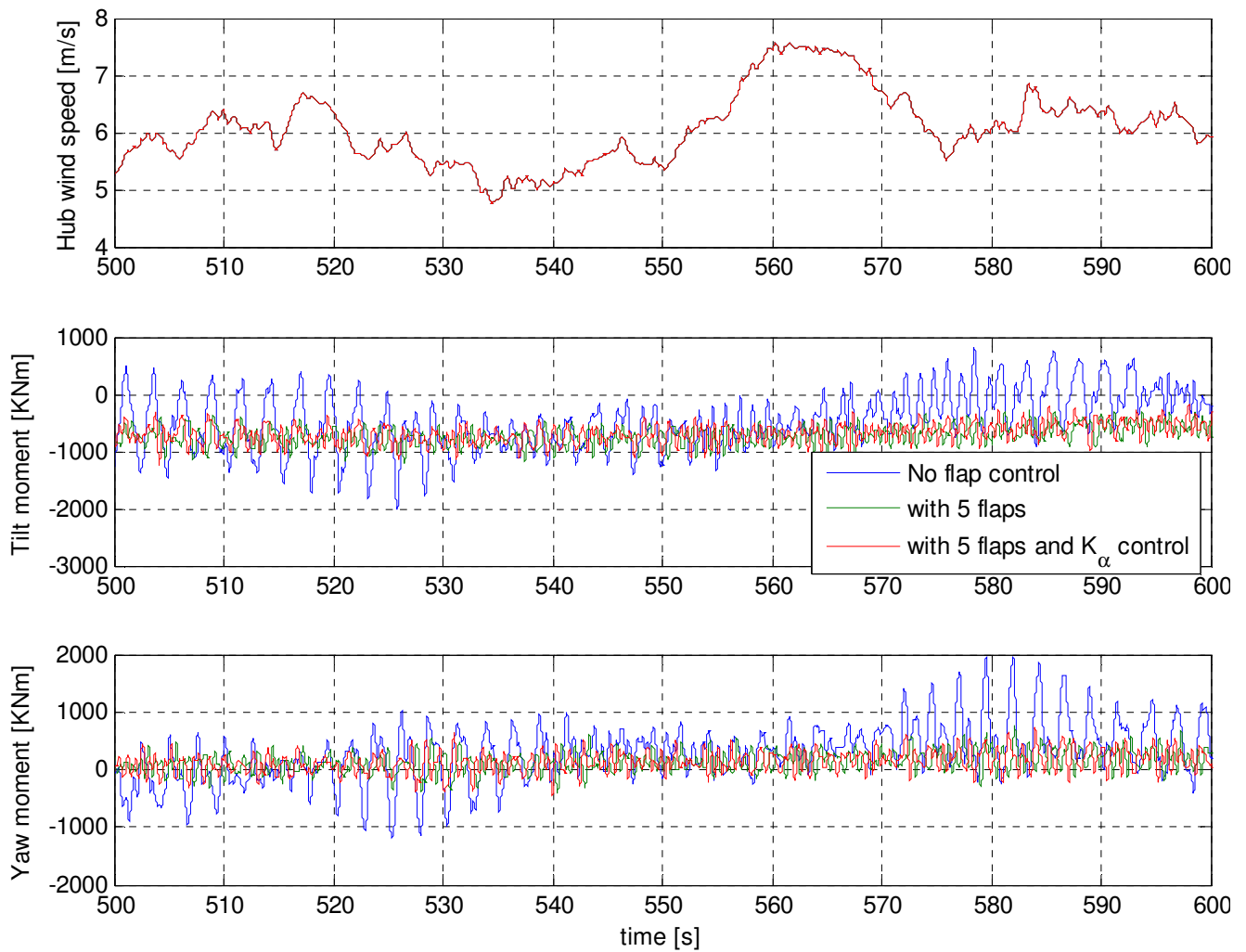


FIGURE 31 TIME SERIES OF FREE WIND SPEED AT HUB HEIGHT, TILT AND YAW MOMENTS. FLAP CONTROLLERS WITHOUT AND WITH POWER OPTIMIZATION IS COMPARED TO THE CASE WITHOUT A FLAP CONTROLLER.

Stability limits was investigated using this controller in the work of Buhl et al [65]. This study did not reveal instabilities using the combined sensor type controller under normal operation.

It is an interesting question how this method can be implemented on a real turbine. Having reliable and accurate wind turbine models should make the job of porting this controller to actual turbines easier.

3.4.4 CONCLUSION

In addition to a traditional pitch regulated wind turbine control, the deformable trailing edge flaps has been included. The proposed controller is designed for the 5MW UpWind reference turbine and tested in wind speeds ranging from cut-in to cut-out i.e. 4-25m/s. This range of wind speed is covered using three ten minute turbulent wind series. The sensors used to control the deformable trailing edge flap are a combination of Pitot tubes and strain gauges.

At 11m/s mean turbulent wind using one 6.3 meter long flap, the fatigue load in flapwise blade root moment is reduced 31%. For three flaps per blade the load reduction is 41%. The fatigue in the flapwise blade root moment is decreased 42% for 18m/s when using five flaps per blade. For all wind speeds the proposed controller show significant fatigue reductions for both blade flapwise and tower flowwise root moments.

The rate of pitching for the flap controllers are compared to the controller without flaps. In general the rate of pitching is decreased when using flaps.

The power yield is not affected in a significant way for the constant tip-speed control regime. In fact, an increase of 1% in power output was obtained for given control parameters.

So far the controllers from this and the previous sections have been designed and tested using homogeneous turbulent inflow, perhaps using different shears and random seeds for generating the 3D turbulent field.

As part of future work, the controller could be tested in a full IEC load case setup. Instead, the controllers have been tested using the dynamic wake meandering model, shown in the next section.

3.5 USING TRAILING EDGE FLAPS TO ALLEVIATE EFFECTS OF MEANDERING WAKES

Most new wind turbines are installed in clusters or near other turbines. Wind turbines located in wind farms experience inflow wind conditions which are substantially modified compared to the ambient wind field that apply for stand-alone wind turbines due to upstream emitted wakes, see Figure 32. The need for reliable and accurate prediction of the increased loadings due to wake operation has led to the dynamic wake meandering model [66].

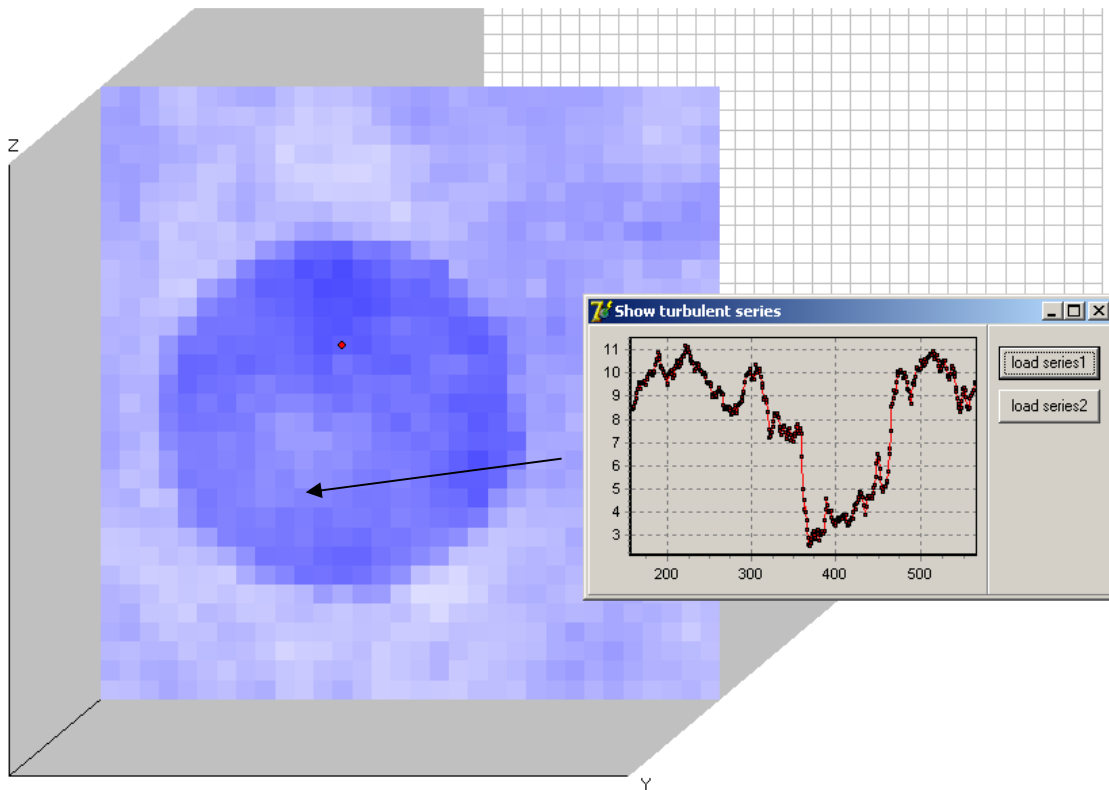


FIGURE 32 EXAMPLE OF TURBULENCE SERIES WITH MEANDERING DEFICIT FROM UPSTREAM TURBINE.

It is natural to investigate the deformable trailing edge flap potential when installed on a wind turbine which experiences the effect of one or several meandering wakes from upstream turbines.

3.5.1 MEANDERING WAKE MODEL

The basic physical mechanisms in the wake are part of the model, i.e. the velocity deficit, the meandering of the deficit and the added turbulence, all modeled as simple as possible in order to

make fast computations in HAWC2 [25]. The meandering wake phenomenon has implications not only for the power production of a wind farm, but also, and equally important, for the loading conditions of the individual turbines in the farm. A correct wind turbine load prediction requires both turbulence intensity and turbulence structure correctly described which is ensured by the dynamic wake meandering model complex. Load and production aspects are predicted, which is contrary to the traditional methods that typically focus on either load- or power prediction. As a consequence the proposed formulation opens for control strategies for the individual turbine.

Previously the influence of the wake was taken into account by introducing an increased effective turbulence. This increased turbulence depends on a number of parameters such as distance to the upstream turbine, turbine loading and ambient turbulence. A description of this methodology and the research behind it can be found in the work of Frandsen [67]. It is also at present the recommended method to take into account wake operation in the IEC61400-1 standard [68].

Further detailed modeling of the wake is needed is for advanced control developments based on individual pitch and flap control. It is important to be able to model correctly the influence of the ambient turbulence levels and in particular the very low turbulence levels observed on offshore sites. The underlying hypothesis in the dynamic wake meandering model is that the wake deficit from the upstream turbine, in combination with meandering of this deficit, is the major contributor to the increased loading; see the work of Madsen et al [69]. The detailed formulation of the meandering mechanism applied in the dynamic wake meandering model was described in Larsen et al [70]. However, the meandering of the wake, and its influence on the fatigue- and extreme loading on a downstream turbine, seems not to have been paid much attention, Ainslie [71] discusses the subject in more details and models the effect from wake meandering on mean wake deficits by correlating the wake meandering to the variability in the wind direction. The dynamic wake meandering model is constituted by three parts

- ➔ a model for computation of the quasi-steady wake deficit and its development downstream
- ➔ a model of the downstream wake meandering process
- ➔ a model of the wake added turbulence

For more detailed description of the wake model please consult the work of Madsen et al [66].

3.5.2 SETUP OF CASES

The deformable trailing edge flap is tested for a meandering wake situation in a wind farm or park. The 5 Mega Watt reference turbines are used. Flaps, sensors, controllers, turbulent inflow conditions and properties of the wind farm will be described in the following sub sections.

3.5.2.1 CONTROLLERS

Controller A is described in section 3.2, where the flap reacts to variations in the elastic deformations.

Controller B is described in section 3.3. The f_1 control keeps the lift constant using the incidence angle and the relative wind speed.

Controller type A and B can be considered building blocks which can be recombined in other configurations.

A new **controller type DMW** (Dynamic Meandering Wake), is used in this investigation. It combines the strain gauge control, where the aerodynamic forces are integrated along the blade, with the Pitot tube which provide the outer flap with rapid information about when a meandering wake is approaching. Controller DMW has two larger inner section controllers based on strain, the type A controller and an outer flap which is controlled through inflow measurements using a simplified version of the B controller.

The simplified type B controller use the measured incidence angle α and the flap deflection β

$$f_3(\alpha, \beta) = C_L = \frac{\partial C_L}{\partial \alpha} \alpha + \frac{\partial C_L}{\partial \beta} \beta \quad (74)$$

$$\frac{\partial f_3}{\partial \alpha} (\alpha - \tilde{\alpha}) + \frac{\partial f_3}{\partial \beta} (\beta - \tilde{\beta}) = 0 \quad (75)$$

The governing equation for the controller, f_3 , is a simplified version of f_1 described in Chapter 3.3. The residuals; $\tilde{\alpha}$, $\tilde{\beta}$ are based on the same time constants given by the rotor speed and radial location on blade.

3.5.2.2 CONTROL AUTHORITY

The effect of the flap control authority will be tested using different constrains on maximum flap deflection and by attaching flaps to 30% and 60% of the total blade length.

Tiny Deflection (T): The flap is constrained to deflections of +/- 2.5 degree, corresponding to C_L changes of +/- 0.075.

Standard Deflection (S): The flap is constrained to deflections of +/- 8 degree, corresponding to C_L changes of +/- 0.25. This has been the typical case used so far.

Large Deflection (L): The flap is constrained to deflections of +/- 12 degree, corresponding to C_L changes of +/- 0.37.

The tiny maximum deflection (T) is close to the maximum possible deflection of the piezoelectric flap and the standard maximum deflection (S) is valid for the rubber trailing edge flap prototypes tested so far. New prototypes may give larger maximum flap deflections which is the motivation for having the investigation of the large maximum deflection (L). It should be noted, that it is important the large flap deflections does not add additional acoustic noise through flow separation.

The flaps are ideal meaning the response is instantaneous, which may not be the case in real life.

The instantaneous flap response is probably valid for the piezoelectric prototype. Whereas the current rubber trailing edge flap has a 100-200ms first order type delay [15]. Chapter 3.2 contains an

investigation of the effect of adding two different types of delayed response to the control, see Figure 22. Type one is a queued type and two is a first order delayed type flap response.

3.5.2.3 WIND FARM TOPOLOGY

The distance between the turbines in the wind farm is given in rotor diameters, see Figure 33. There are indications that the fatigue load is a function of the distance between the turbines. This is the motivation for investigating several distances. The meandering wake requires some distance to fully develop consequently this investigation include wind turbine placed **D2.4**, **D6** and **D10** rotor diameters apart [72].

A uniform grid of turbines is used in the wind farm.

A wind turbine which is placed in the second row of turbines is used in the investigation. The turbine from the first row generates a meandering wake which affects the turbine standing the second row.

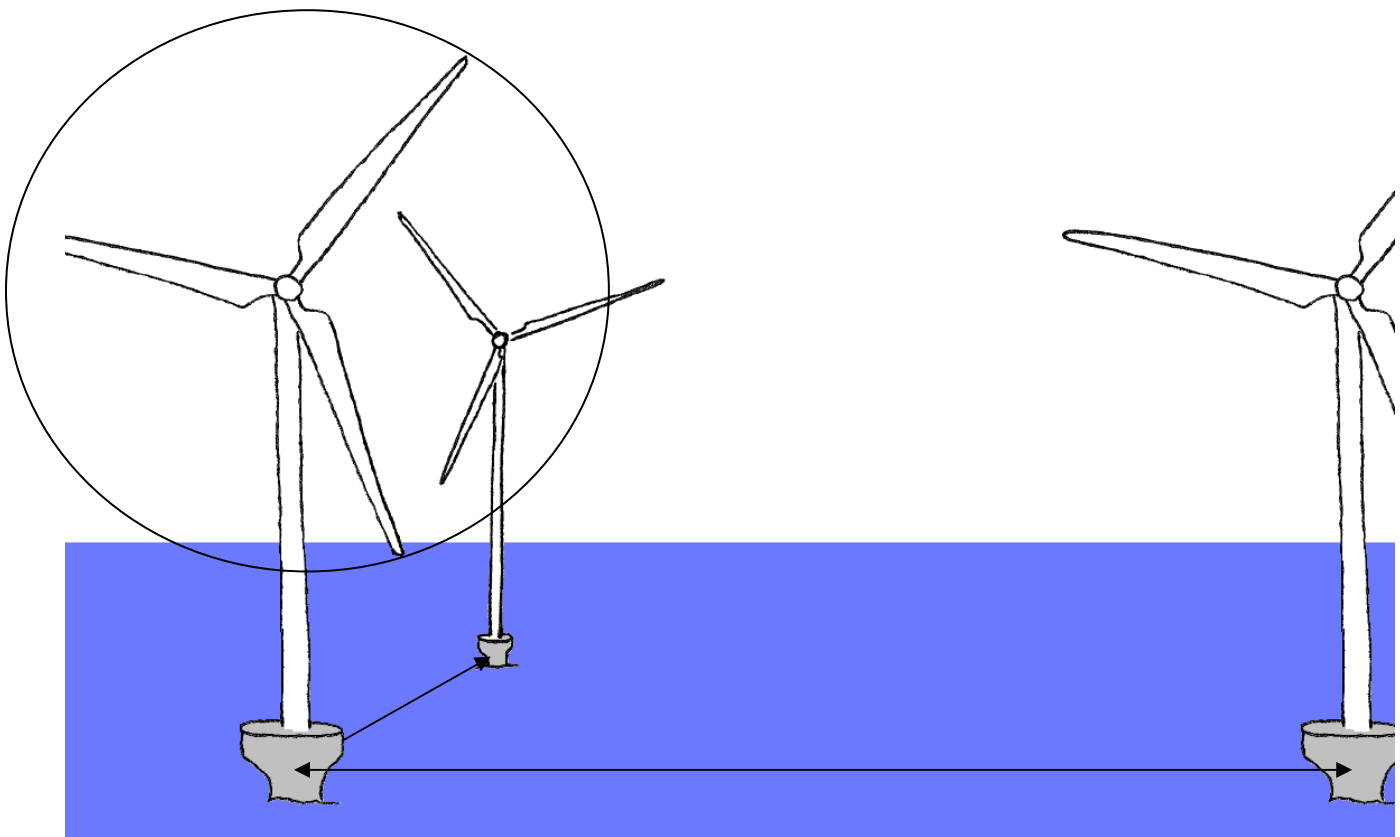


FIGURE 33 DISTANCES BETWEEN TURBINES IN AN OFFSHORE WIND FARM IS MEASUED IN ROTOR DIAMETERS.

The distance D2.6 corresponds to 333 meters between the turbines. The distance D6 is 768 meters and finally D10 is 1280 meters.

3.5.2.4 AMBIENT TURBULENCE

The mean turbulent wind speed of 11m/s is close to rated power making
 For the **onshore (ON)** conditions an ambient turbulence intensity of 10% is used.
 For **offshore (OFF)** conditions the ambient turbulence intensity is lower 6%.

3.5.2.5 FLAP AND SENSORS

A configuration with 3 flaps per blade is tested. The basic flap configuration is shown in Figure 34. Two versions of the flap configuration were used, see Table 6. Version one has to total of 60% of the blade equipped with active trailing edge flaps, and version two uses 30% but with similar control input. Version one uses more flap material and has therefore gotten the letter **(E)** for presumable Expensive and the second configuration using half the flap length is called **(C)** for Cheaper.

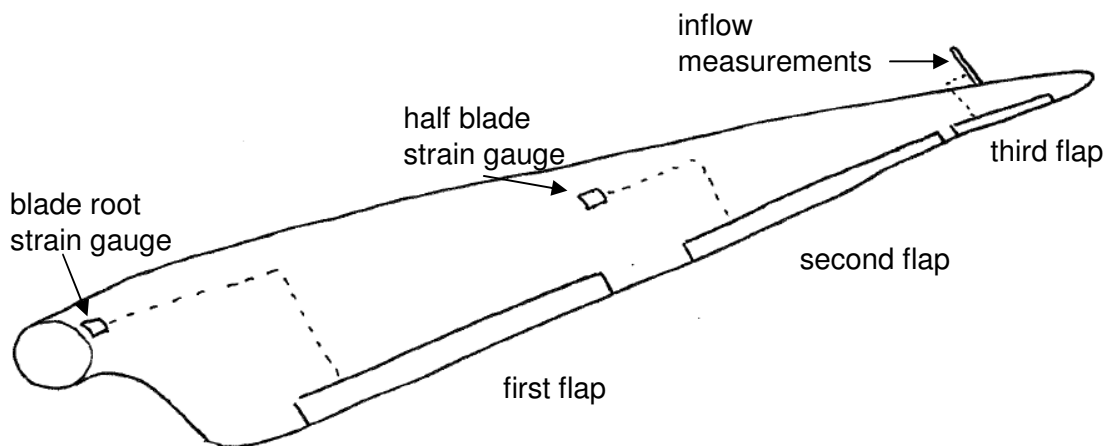


FIGURE 34 FLAP CONFIGURATION FOR TYPE D CONTROLLER.

Two strain gauges and a Pitot tube provide input for the controller type DMW. The stain gauges are placed in the root section and at the half blade point where they control the two inner flaps. The Pitot tube controls the outer flap and it is placed 7 meters from the blade tip.

TABLE 6 TWO VERSIONS OF THE 3 FLAP CONFIGURATIONS

	first flap	second flap	third flap	total length
Version one DWM (E)	15.8-28.4m	33.0-52.0m	53.6-59.9m	37.8m
Version two DWM (C)	28.4-34.7m	44.1-50.4m	53.4-59.9m	18.9m

3.5.3 RESULTS AND DISCUSSION

Fatigue loads in flapwise blade root moment, yaw moment and the aerodynamic torque is compared. Different maximum flap deflection constraints are used. Two different ambient turbulence intensities are used, which corresponds to onshore and offshore conditions. The fatigue is calculated with material parameter 4, typical for steel, for yaw and torque. For calculating fatigue loads in the flapwise root moment, the material parameter 10 is used which is typical for glass fiber materials.

Fatigue loads for the **flapwise blade root moment** is presented in Table 7.

Fatigue loads for the **yaw moment** is presented in Table 8.

Fatigue loads for the **aerodynamic torque** is presented in Table 9.

TABLE 7 FATIGUE LOAD REDUCTIONS IN FLAPWISE BLADE ROOT MOMENT USING THE DWM DEFORMABLE TRAILING EDGE FLAP CONTROLLER. PERCENT REDUCTIONS ARE IN BRACKETS.

blade flapwise root moment	D2.4 (ON)	D6 (ON) ^[H]	D10 (ON)	D6 (OFF) ^[H]
no flap	4181 ^[J]	5428 ^[J]	7715 ^{[J] [K]}	3097
DMW (T) (E)	3449 (18%) ^{[A] [E]}	4535 (16%) ^[E]	6429 (17%) ^[E]	2425 (22%)
DMW (S) (E)	2606 (38%) ^{[B] [D0] [G]}	2766 (49%) ^[G]	2343 (70%) ^[G]	1484 (52%)
DMW (S) (C)	3029 (28%) ^{[D1] [F]}	3834 (29%) ^[F]	5103 (34%) ^[F]	2179 (30%)
DMW (L) (E)	1847 (56%) ^{[C] [D2] [G]}	2157 (60%) ^[G]	2091 (73%) ^[G]	1167 (62%)

TABLE 8 FATIGUE LOAD REDUCTIONS IN YAW MOMENT USING THE DWM DEFORMABLE TRAILING EDGE FLAP CONTROLLER. PERCENT REDUCTIONS ARE IN BRACKETS.

yaw moment	D2.4 (ON)	D6 (ON) ^[H]	D10 (ON)	D6 (OFF) ^[H]
no flap	3517 ^[K]	4066 ^[K]	3416 ^[K]	2462
DMW (T) (E)	2549 (28%) ^[D]	3049 (25%)	2505 (26%)	1682 (31%)
DMW (S) (E)	1652 (53%) ^[D0]	1836 (55%)	1582 (54%)	985 (60%)
DMW (S) (C)	2343 (33%) ^[D1]	2753 (32%)	2224 (35%)	1539 (37%)
DMW (L) (E)	1393 (60%) ^[D2]	1692 (58%)	1647 (52%)	888 (64%)

TABLE 9 FATIGUE LOAD REDUCTIONS IN AERODYNAMIC TORQUE USING THE DWM DEFORMABLE TRAILING EDGE FLAP CONTROLLER. PERCENT REDUCTIONS ARE IN BRACKETS.

aerodynamic torque	D2.4 (ON)	D6 (ON)	D10 (ON)	D6 (OFF)
no flap	979 ^[K]	1454 ^[K]	1430 ^[K]	654
DMW (T) (E)	922 (6%)	1399 (4%)	1342 (6%)	639 (2%)
DMW (S) (E)	814 (17%)	1354 (7%)	1216 (15%)	524 (20%)
DMW (S) (C)	887 (9%)	1262 (13%)	1292 (10%)	553 (15%)
DMW (L) (E)	818 (16%)	1264 (13%)	1279 (11%)	508 (22%)

RESULTS FOR ONSHORE TURBINES PLACED 2.4 ROTOR DIAMETERS APART

[A] The flap, which has the smallest maximum flap deflection (**T**), can reduce the fatigue loads in the flapwise blade root moment by 18%.

[B] The standard maximum flap deflection (**S**) can reduce the fatigue loads in the flapwise blade root moment by 38% which is twice as effective compared to the tiny maximum deflection.

[C] The maximum flap deflection (**L**) can change the lift coefficient by $C_L = \pm 0.35$, it can also reduce the fatigue loads by nearly three times as much as the three degree (**T**) maximum deflection.

[D] The yaw moment is affected by all blades. The fatigue loads in the yaw moment is alleviated by $3 \times 3 = 9$ flaps which probably explains the quite significant load reduction of 28% for the flap which is constrained to only ± 2.5 degree deflections (**T**).

[D1] [D0] When doubling the overall flap length from 30% to 60% of the blade length (100% increase) the fatigue load reduction for the blade root moment is increased from 28% to 38% (10% points increase). Whereas, the fatigue load reduction for the yaw moment is increased from 33% to 53% (20% points increase).

[D0] [D2] When doubling the maximum possible flap deflection from 8 to 12 degrees (50% increase) the additional fatigue load reduction in the flapwise blade root moment is increased from 38% to 56% (18% points increase). Whereas, the fatigue load reduction for the yaw moments is increased from 53% to 60% (7% points increase).

[D0] [D1] [D2] This suggests that depending on which type of loads that is considered critical the research efforts could be different. Should research efforts be used to make large flaps affordable or should the flap have a greater deflection range or perhaps perform faster deflections. If all can be achieved then naturally this is preferable, but often this is not possible.

COMPARING RESULTS FOR ONSHORE TURBINES AT 2.4, 6 AND 10 ROTOR DIAMETERS

[E] The load reduction potential is somewhat unaffected by the distance between the turbines when flaps are constrained to ± 2.5 degree deflection (**T**).

[F] The load reduction potential is decreased percentagewise for the 30% flap length (**C**) configuration when going from turbines placed 2.4 towards 10 rotor diameters.

[G] The load reduction potential is increased significantly percentagewise for the standard (**S**) and the large (**L**) maximum constrained flap deflection when going from turbines placed 2.4 towards 10 rotor diameters.

OFFSHORE TURBINES PLACED 6 ROTOR DIAMETERS APART

[H] The fatigue load reduction potentials for offshore turbines are slightly higher compared to an onshore wind turbine with a similar setup. The result of 10 minute simulated time series for an offshore wind turbine is shown in Figure 35. In Figure 35 the green curves represents the offshore wind turbine with the three flaps and the blue curve represents the same turbine without flaps. Notice how blue curves appear to be fluctuating much more than the green indicating greater load fluctuations.

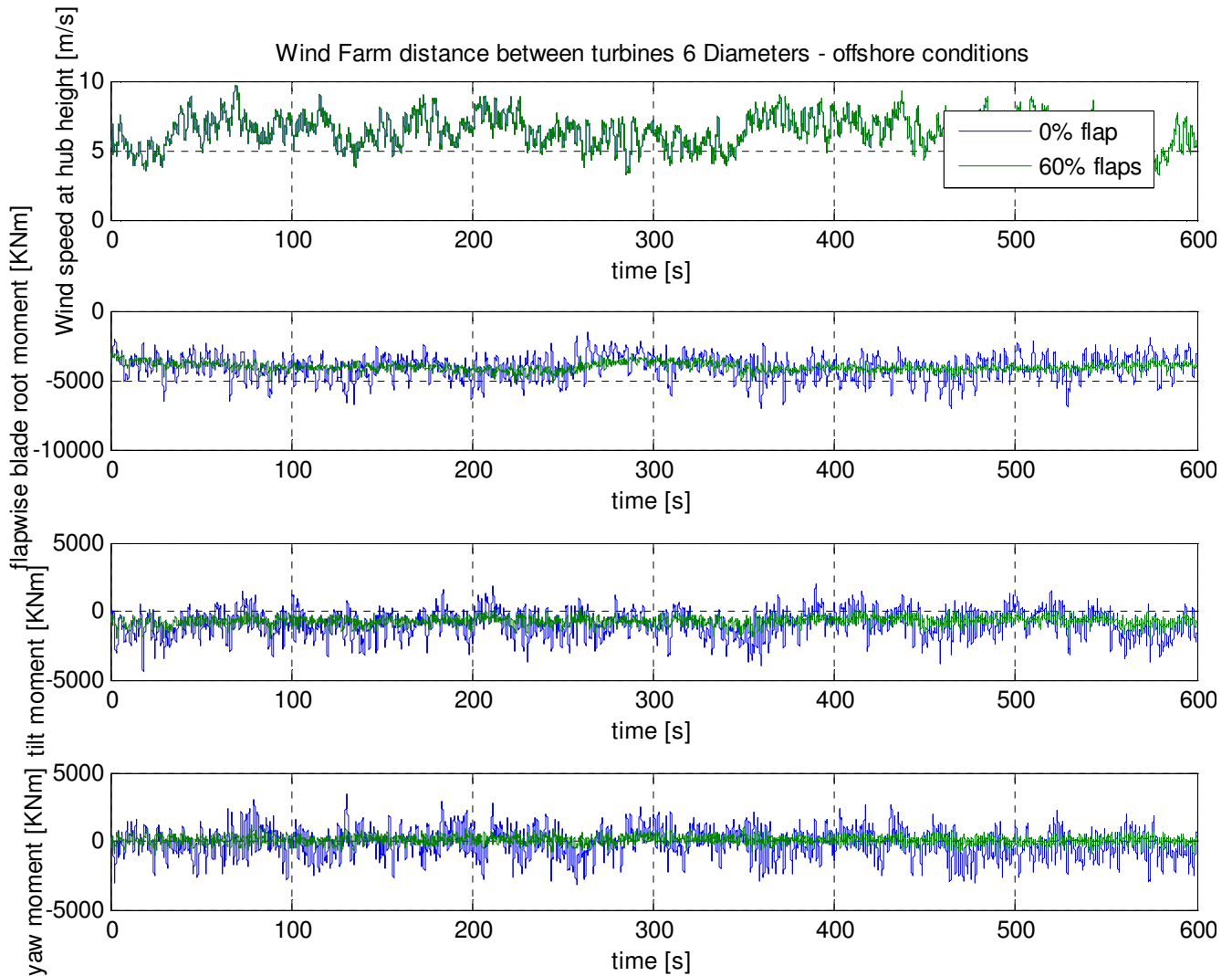


FIGURE 35 SIMULATED LOADS ON AN OFFSHORE TURBINE PLACED IN A WIND PARK. FROM TOP TO BOTTOM WIND SPEED AT HUB HEIGHT, FLAPWISE BLADE ROOT MOMENT, TILT MOMENT AND YAW MOMENT. FLAPS ARE CONSTRAINED TO A MAXIMUM OF +/- 12 DEGREES.

IN GENEREL

[J] The fatigue loads increases as the distance between the turbines becomes larger than 2.4 rotor diameters in the wind farm. This is because it takes some time for the meandering wake to fully

develop and cause additional fatigue damage to downstream wind turbines [72]. At some number of rotor diameters between the turbines a maximum fatigue load was expected.

[K] For yaw moment and aerodynamic torque fatigue loads the worst distance is 6 rotor diameters. Whereas, the worst fatigue load for the flapwise root moment is at 10 rotor diameters.

There are three ways of increasing the control authority, either through a longer flap (blade spanwise direction), a bigger flap (chordwise direction) or through a bigger maximum deflection.

Significant load reductions, up to 73%, is seen when using deformable trailing edge flaps to alleviate the effects of meandering wakes in wind farms. There are even significant load reductions for the case where the flap is constrained to ± 2.5 degrees. This changes the lift coefficient by ± 0.075 .

3.5.4 CONCLUSION

The fatigue load reduction potential of deformable trailing edge flaps for a wind turbine in the second row of a wind farm has been investigated. The load reduction potential of the deformable trailing edge flap has been found to be a function of the distance between the turbines, the turbulence intensity and the control authority of the flap.

The distances between the turbines are 2.4, 6.0 and 10.0 rotor diameters. Onshore and offshore ambient turbulence intensities have been used.

The control authority of the flap was investigated. The flap deflection was constrained to ± 2.5 , ± 8 and ± 12 degrees, which corresponds to $\Delta C_L = \pm 0.075$, $\Delta C_L = \pm 0.25$ and $\Delta C_L = \pm 0.35$ respectively. The control authority in terms of the ability of the flap to shift the aerodynamic forces is an important parameter to consider for any flap prototypes. The load reduction could be 18%, 38% and 56% depending on the flap being able to shift the lift coefficient, ΔC_L , by 0.075, 0.25 or 0.35.

A significant load reduction, up to 70%, is seen when using a deformable trailing edge flap constrained to ± 8.0 degree flap deflections. Load reduction of up to 28% for the flap which is constrained to ± 2.5 degree deflections has been achieved.

3.6 CHAPTER ENDNOTE

The potential of the deformable trailing edge flaps with regard to reducing fatigue loads primarily in the flapwise blade root moment has been investigated in Chapter 3. The active flaps have been mounted on 10%, 20%, 30% and 60% of the blade length.

Four different controller and sensors concepts were investigated in Chapter 3. Controller A used a sensor based on a strain gauge to control the flap. Controller B used a Pitot tube to measure the dynamic inflow to control the flap. A combination of stain and inflow sensors has been combined with a traditional collective pitch variable rotor speed power controller. This is called controller type C. Finally a controller has been tested for wind farms. This controller is called controller type DMW (Dynamic Wake Meandering).

Some of the results from section 3.2 to 3.5 have been compiled in Table 10 for comparison. D2.4, D6 and D10 correspond to the number of rotor diameters between the turbines in the wind farm.

TABLE 10 FATIGUE LOAD REDUCTIONS IN PERCENTAGES FOR THE EQUIVALENT FLAPWISE BLADE ROOT MOMENT WHEN USING 10%, 30% AND 60% ACTIVE FLAPS PER BLADE AND CONTROLLER TYPES A, B, C AND DMW.

Chapter	turbulent mean wind speed	controller type	one flap 10% of blade	flaps in total 30% of blade	flaps in total 60% of blade
3.4	7m/s	Type C	18%	42%	47%
3.4	7m/s ⁽⁶⁾	Type C	-	36%	-
3.2	10m/s	Type A	25%	37%	-
3.3	10m/s	Type B	30%	40%	-
3.4	11m/s	Type C	31%	41%	43%
3.5 ⁽⁷⁾	11m/s D2.4	Type DMW	-	28%	38%
3.5	11m/s D6	Type DMW	-	29%	49%
3.5	11m/s D10	Type DMW	-	34%	70%
3.5	11m/s D6 ⁽⁸⁾	Type DMW	-	30%	52%
3.4	18m/s	Type C	23%	34%	42%

The controllers were tested in a typically wind farm scenario, where turbines sometimes are subject to meandering wakes from upstream turbines. A turbine, placed in the second row in the wind farm, was equipped with three flaps per blade. The smart controller, type DMW, could alleviate the fatigue loads by as much as 70% in some cases.

Overall the results presented in Chapter 3 suggest that the deformable trailing edge flap is useful for fatigue load alleviation in the blade flapwise root moment. The fatigue loads have furthermore been investigated for the yaw moment, tilt moment and the torque, the deformable trailing edge flap can also reduce the fatigue loads significantly for these.

⁽⁶⁾ Power optimization coefficient $K_{\alpha} > 0$ with Type C proposed controller.

⁽⁷⁾ The dynamic wake meandering model has been used for all the results in Chapter 3.5.

⁽⁸⁾ Results are based on offshore turbulent conditions.

It is important to investigate the response time of the flap. In fact, determining the control authority of the flap has to be done to fully uncover the potential of the deformable trailing edge flap. Results from Chapter 3.2 indicate that time constants greater than 200ms can reduce the load reduction potential up to 50%. In Chapter 3.5 three different constraints were placed on the maximum deflection of the flap, proving this to be an important parameter. The load reduction could be 18%, 38% and 56% depending on the flap being able to shift the lift coefficient, C_L , by 0.075 , 0.25 or 0.35 .

PART II - EXPERIMENTS

CHAPTER 4

WIND TUNNEL EXPERIMENTS

The previous chapter investigates the fatigue load reduction potential of the deformable trailing edge flap mounted on the five Mega Watt reference turbine used in the UpWind project. Simulations showed it was important to determine the flap response time and the change in aerodynamic forces. In some cases the control authority of the flap is insufficient. There are three ways to alleviate this.

- increase the maximum deflection
- increase the length of flap (blade spanwise direction)
- increase the size of the flap (in chordwise direction, for now 10% of the chord is used)

The possibility to change the maximum deflection of the flap has a lot to do with which type of flap is used. The piezoelectric flap is constrained to the deflection offered by the ceramic material. The rubber trailing edge flap [15] deflects when pressure in the cavities is altered. The rubber flap can change the maximum deflection by using an increased air or hydraulic pressure. Tests conducted in December 2009 in the Velux wind tunnel with the rubber trailing edge flap showed an increased maximum deflection when 8 bar pressure was used instead of 6 bar.

Increasing the flap in spanwise direction is easy when doing simulations. However a longer flap is assumed to cost more, which is why so much effort has been made to always show where to place the flap on the blade to get the most load reduction.

When increasing the size of the flap in chordwise direction, the flap becomes heavier which is generally undesirable for stability issues, response times and cost. The rubber flap looks promising, especially if light and robust materials can be used. The next chapter will go into more detail with experiments conducted using the piezoelectric flap.

To further extend the investigation, two wind tunnel experiments using unimorph piezoelectric benders⁽⁹⁾ were carried out at Risø DTU. Results from an open loop experiment described by Bak et al [12] have been used to prepare for a closed loop experiment, which has been carried out in this PhD work. The open loop experiment was used to investigate an electrical model for the closed loop control. Chapter 4.1 describes the open loop control and Chapter 4.2 describes the closed loop experiment.

The wind tunnel setups for both experiments can be found in Appendix C.

Wind tunnel testing was carried out in the VELUX wind tunnel, which is of the closed return type with an open test section having a cross section of 7.5x7.5 m and a length of 10.5 m. The cross section of the quadratic jet blowing into the test section is 3.4x3.4 m. The maximum flow velocity is $U=40$ m/s giving $Re=1.66 \times 10^6$ for the airfoil. The airfoil section was mounted 1.7 m from the tunnel floor and 3.2 m from the nozzle outlet. End plates were fixed to the stand at the ends of the airfoil section to limit 3D flow effects. The VELUX test setup was developed and verified [74]. Turbulence is estimated to 1% at 40 m/s, which is high compared to traditional wind tunnels. The 2D wind tunnel test using a Risoe-B1-

⁽⁹⁾ Thunder^(TM) TH-6R <http://www.faceinternational.com/>

18 airfoil [75] developed for wind turbines with pitch regulation and variable rotor speed and equipped with a trailing edge flap was conducted.

The basic airfoil had a chord length of 600mm, spanwidth of 1900mm and a relative thickness of 18%. At the trailing edge of the non-deformable airfoil actuators were glued to the pressure side. The actuators were Thunder elements. The elements have a stainless steel substrate as the main beam, a piezoceramic layer and an aluminum top layer. Formally, this actuator is referred to as a unimorph piezoelectric bender. The aluminum layer serves principally as a means for soldering lead wires. Applying voltage between -450V to 700V the actuator would deflect between 3.5mm to the piezoceramic side and 1.5mm to the side with the stainless steel. The attached Thunder element near the trailing edge added an additional 60mm to the chord length, which in total became 660mm long. For more detail please refer to Bak et al [12].

Four strain gauges were mounted on the trailing edge flap, two on the suction side and two on the pressure side. Of the four gauges the second strain gauge was mounted near the flap root on the airfoil pressure side and 790mm from the centerline, see Appendix D.

4.1 PRE-DESCRIBED FLAP MOTION EXPERIMENT

To obtain knowledge for the closed loop experiment results from an earlier wind tunnel experiment described by Bak et al. [12] was investigated. This test contained steady state tests and dynamic tests in terms of step changes and sinusoidal changes in the flap deflection and sinusoidal pitching of the whole airfoil superimposed with sinusoidal changes in the flap deflection. All tests were carried out with prescribed pitch and flap deflections. Thus, the tests did not contain any sensing of the flow and corresponding actuation of the flap. This test was designed to investigate the concept and provided information on two fronts for the future work with smart rotors:

- i. The aerodynamic performance in terms of lift, drag and moment have been used as input for the dynamic stall model necessary when investigating the load reduction potential of the trailing edge flaps while conducting aeroservoelastic load simulations on full scale turbine.
- ii. The first experiment gave valuable insight into the response of the flap when imbedded in an electrical circuit. Although the response time is considered fast and reliable, there have been concerns regarding the depolarization of the piezoelectric material when operating exclusively at voltages close to the high or low limits. It turned out that the flap showed non-symmetric characteristics in the response in deflection depending on the flap bending up or down. There were concerns whether or not the power amplifier would be able to provide enough power during rapid peak to peak flap deformations. Finally, the extent of the aerodynamic feedback to the electrical system had to be investigated.

Although the electrical modeling is not part of the first experiment, the results from the experiment provided the data needed for the second flap experiment conducted in July 2009. The transfer function between the control volts and flap deflection will be provided through an electrical model. The turbulence intensity is relatively high in the VELUX wind tunnel and initial studies revealed that imperfections in the piezoelectric material of the Thunder actuator combined with high frequency Volt

excitation caused the actuator to expire more rapidly, consequently the turbulence in the wind tunnel measured in front of the airfoil is examined.

4.1.1 ELECTRIC MODEL

The control of the flap can be modeled in two ways. Either it can be modeled by establishing a mathematical model described by physics or by system identification via experimental data. In the following a crossover between the two modeling principles is proposed, in which, the laws of physics provides the foundation for the electric model and the measurements from the first measurement campaign is used to tune the coefficients of the physical model.

The input voltage is amplified by a factor K_{amp} which is 200. The electrical system consists of several parts: the amplifier, the flap and transducers. Internally and outside the amplifier the electronics can be modeled using a series of resistors, capacitors and inductances represented by the symbols R, C and L respectively.

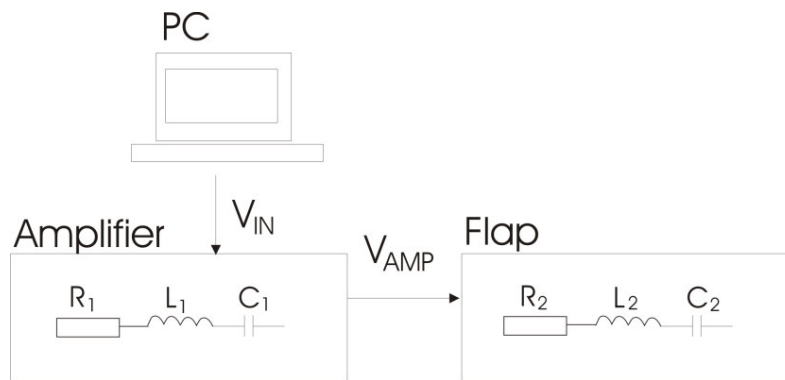


FIGURE 36 ILLUSTRATION OF THE ELECTRICAL CIRCUIT.

The general circuit, shown in Figure 36, can be written up as a single R-L-C component circuit. The voltage delivered by the amplifier to the circuit is called V_{AMP} and the voltage from the personal computer is called V_{IN} . The resistance, inductance and capacitance for the total circuit is described by

$$R = R_1 + R_2 \quad (76)$$

$$L = L_1 + L_2 \quad (77)$$

$$C = \frac{1}{\frac{1}{C_1} + \frac{1}{C_2}} \quad (78)$$

The equivalent electrical system can be described as a second order dynamical system, where a serial R-L-C circuit is used to model the unsteady electric effects. The governing electric equation with a piezoelectric actuator is written as

$$L \frac{\partial^2 q}{\partial t^2} + R \frac{\partial q}{\partial t} + \frac{1}{C} q - EN - K_{AMP} V_{IN} = 0 \quad , \quad (79)$$

The electric charge is q , and the feedback from the aerodynamic loads N to the electric system is assumed proportional with a factor E . The aerodynamic feedback could play a role when determining the magnitude of the control signal needed to control the flap. Figure 37 gives an indication of the magnitude of the aerodynamic feedback.

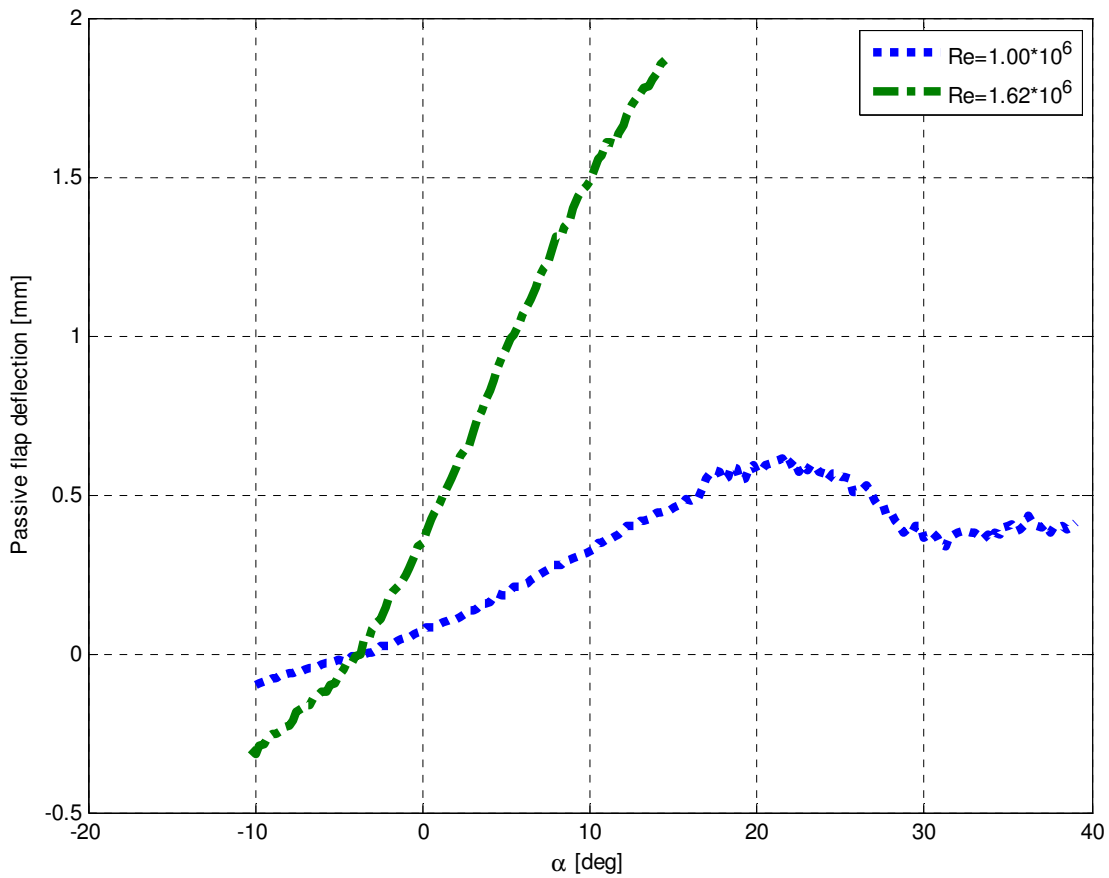


FIGURE 37 MEASURED PASSIVE FLAP DEFLECTION AS FUNCTION OF INCIDENCE ANGLE AT $RE=1.00 \times 10^6$ (25M/S) AND $RE=1.62 \times 10^6$ (40M/S).

The figure shows the flap deflection, strain gauge number two, as function of incidence angle for two different wind speeds. If the passive of flap deflection had been zero for all incidences, it would be safe to disregard the work done by the aerodynamic forces.

At 40m/s the passive flap deflection has a range of more than 2mm for incidence angles ranging from -10° to 15° . The 2mm passive deflection corresponds to applying several hundred volts actively. However, the 2mm passive deflection is caused by the aerodynamic force feedback over 25 degrees incidences.

The tests are primarily conducted at 25m/s or one million in Reynolds number, using \pm one degree harmonic pitch motion. Hence the aerodynamic feedback, E , is assumed zero in the electrical model.

A note should be made concerning the maximum velocity used is 40m/s in the experiments. The blade tip speed velocity can easily reach 80m/s for most turbines giving four times the aerodynamic feedback in loads.

It is assumed that the Thunder actuator has the same electrical characteristics as a capacitor. The applied voltage drop over the capacitor (V_C) is given by

$$V_C = \frac{q}{C} \quad (80)$$

As a first approximation the quasi steady β deflection has a linear dependency of the applied voltage drop over the capacitor given by the proportional constant K_p . This linear approximation represents the simplest link between the electric model and the mechanical flap deflection angle.

$$\beta = V_C K_p \quad (81)$$

4.1.2 TESTING THE ELECTRIC MODEL

To give an example of how the model can be compared to the measurements from the first measurement campaign, the first derivative of the electrical charge corresponds to the current measured in milliamps see Figure 38. Both the voltage out V_{AMP} and the current is measured from the amplifier. The inductance L has a very small value and could be neglected when aiming at reducing loads in low frequency range. In the following example the personal computer sends out square waves V_{IN} ranging from $-0.75V$ to $1.15V$ at $0.47Hz$ and the current in the circuit is compared between the measured and the modeled values.

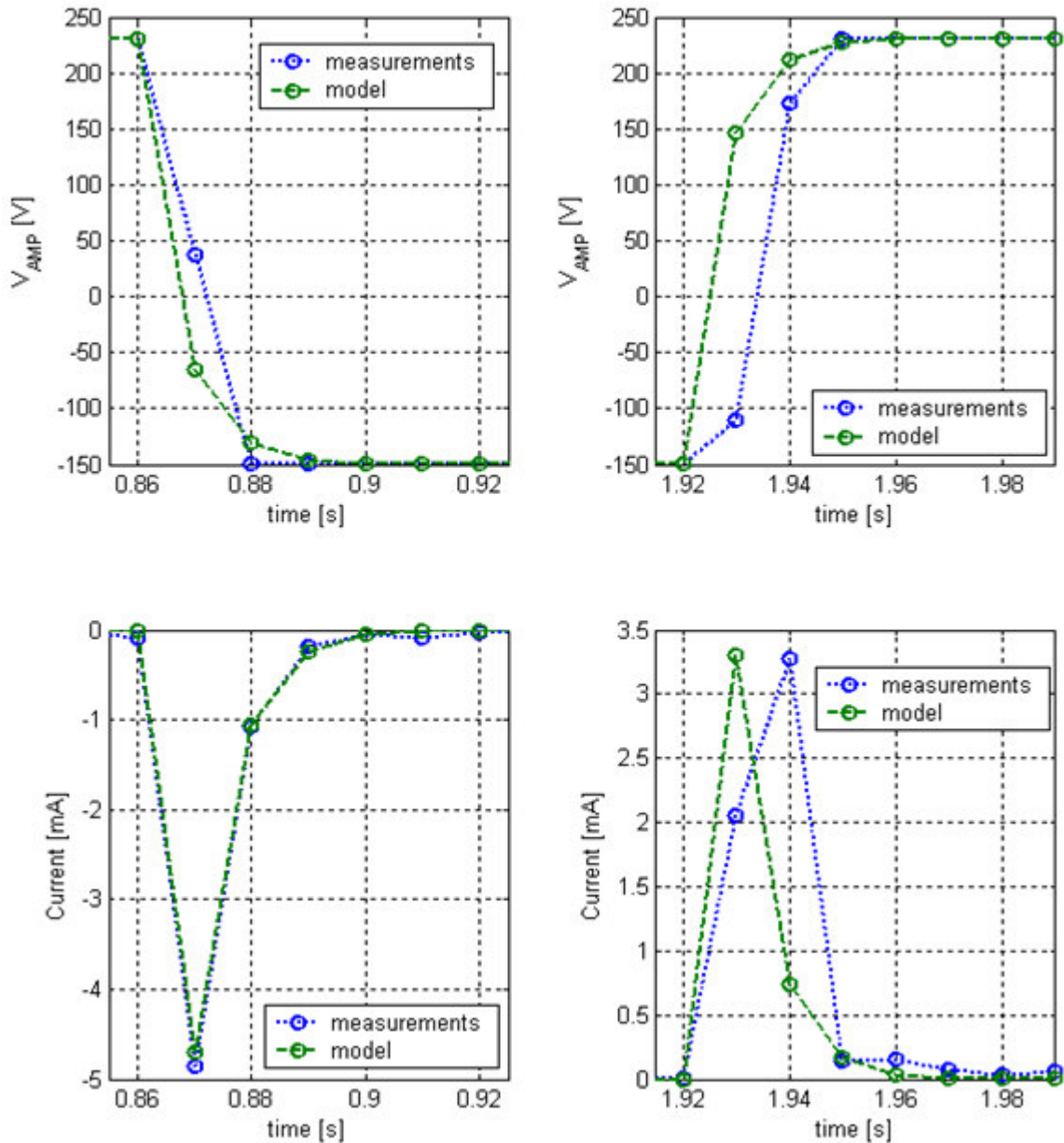


FIGURE 38 0.47HZ STEP CHANGE IN FLAP DEFLECTION APPLIED VOLTAGE -150V TO 230V (LEFT) FLAP DOWN IN STEP (RIGHT) FLAP UP IN STEP.

A simple relation between the electrical side and the mechanical flap deflection is proposed in Equation (81). It is not obvious why the flap deflection should be proportional to the flap voltage, but it is an useful first order approximation. Polarization of the crystal structures and the crystal alignment is often used when describing the complex physics inside the piezoceramic layers. The polarization of the crystal structure is not constant but shifts, especially when the flap is operated in extreme volt ranges over a period of time. This causes the crystals to re-align diminishing the obtainable deflection in that volt range, the phenomenon is sometimes referred to as depolarization. The effect of

depolarization is not pronounced in the previous experiment using square 0.47Hz flap step waves, because the amount of applied volt is relatively low -150V to 230V and there is also a constant shift between positive and negative values. The proportional relation between the electrical applied volt and the mechanical flap deflection (four Strain Gauges are used for determination of deflection; SG1-SG4 see Appendix D) for the 0.47Hz square wave experiment is shown in Figure 38 and Figure 39.

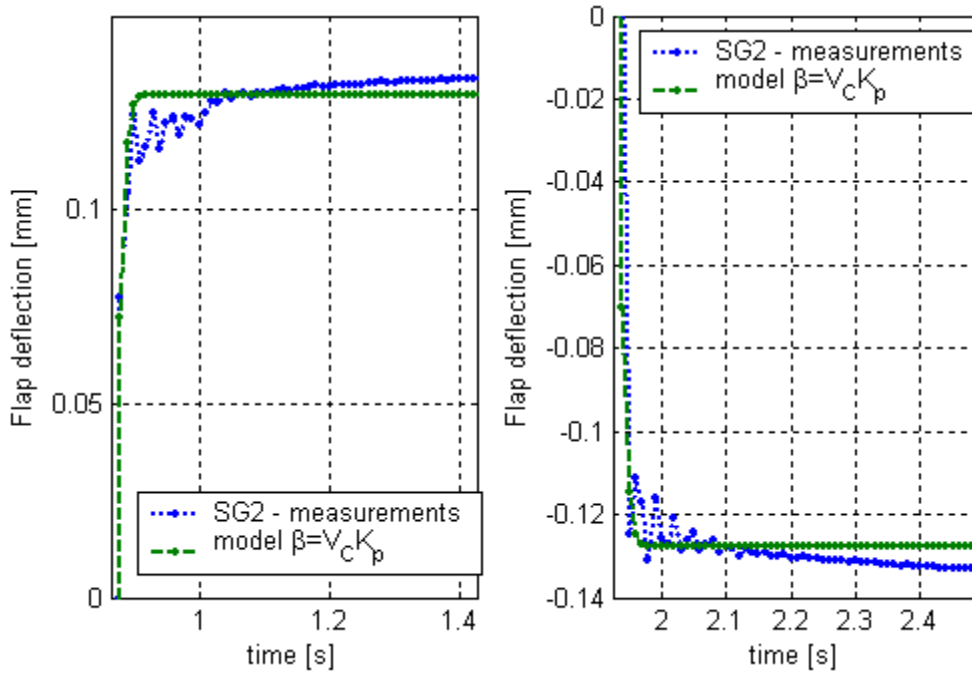


FIGURE 39 PROPOSED MODEL RELATION BETWEEN VOLT AND FLAP DEFLECTION COMPARED TO STRAIN GAUGE MEASUREMENTS (LEFT) FLAP DOWN IN STEP (RIGHT) FLAP UP IN STEP.

An interesting behavior of the flap shown in Figure 39 is the asymptotic drifting after the step in the measured flap deflection, can be seen at $t > 1s$ for flap down and $t > 2.1s$ for flap up. This drift is not captured by the proposed proportional relation between volt and flap deflection, however, the simple model captures the fast first order effect, and will therefore be used in the closed loop experiment.

The proportional gain K_p has a given value. Rather than listing this proportional gain for all the experiments conducted and attempting to give a mean value applicable for all future cases, this gain will remain a parameter to be determined in the following closed-loop experiment.

The constants for the electrical components also have finite values, but again rather than listing the best fitted values, it will up to the user to determine these values when conducting a future experiment.

4.1.3 WIND TUNNEL TURBULENCE

Commonly the VELUX wind tunnel is used to measure quasi steady loads. When attempting to do real time closed loop control, the dynamics of the flow in the wind tunnel becomes an important factor. A

normalized power spectrum of the wind speed from a Pitot tube close to the jet inlet in the open test section, Figure 40, shows the various frequencies.

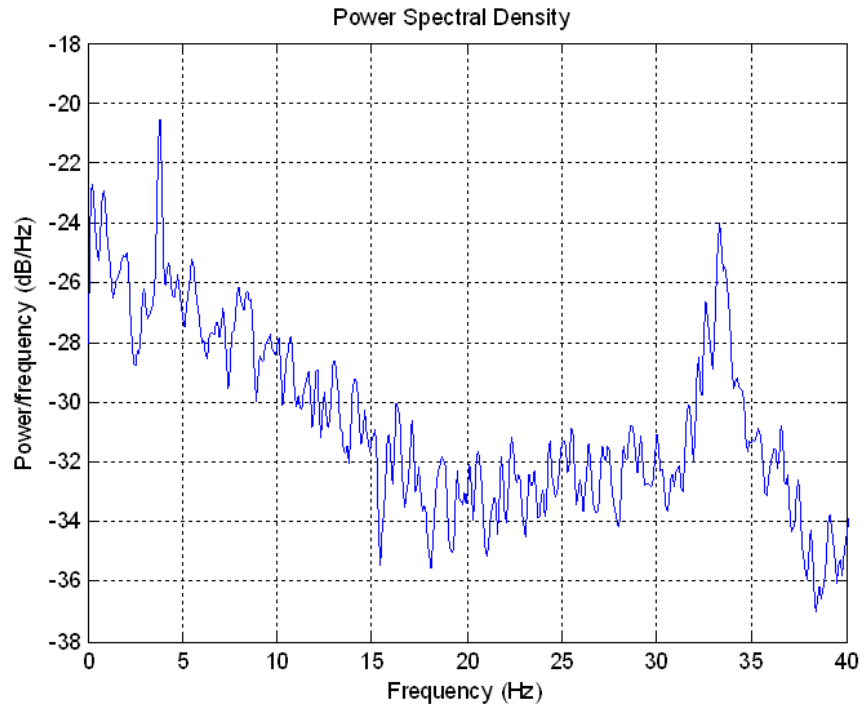


FIGURE 40 NORMALIZED POWER SPECTRUM OF THE FREE WIND SPEED MEASURED AT 25M/S IN THE VELUX WIND TUNNEL.

In particular the peak in the power spectrum at 4Hz is distinct for the VELUX wind tunnel at 25m/s. This specific 4Hz oscillation is the eigenfrequency of the air in the closed loop tunnel, and can be calculated based on the speed of sound and the total length of the wind tunnel. A simple low frequency filter will be added in the closed loop experiment to remove these frequencies.

4.1.4 CONCLUSIONS OF THE RE-EXAMINATION OF THE FIRST EXPERIMENT

The following have been achieved:

The electrical model was not part of the original data analysis for the first experiment. An electric model is suggested which links the control volt to the amplifier and the deflection of the trailing edge flap. This link is needed for the second experiment which includes a closed-loop controller.

A low pass filter will be applied to the control sensor, in an effort to remove unwanted tunnel related frequencies distinct to the VELUX tunnel.

4.2 CLOSED LOOP EXPERIMENT

The aim of this experiment is to show that the deformable trailing edge controller can alleviate fluctuating loads. On a real turbine this is caused by the elastic fluctuations and the turbulent inflow. For the current experiment the disturbance primarily comes from the pitching of the profile and the general wind tunnel turbulence. The controller is not aware of the pitching motion of the airfoil. The scope of the current work is to experimentally test and demonstrate the concept and the potential of using adaptive trailing edge flap in an active closed loop using different sensing techniques. In the field of smart control much focus is given to the design of the actuator. This is natural, but numerical algorithms, sensors and the control is just as important for the overall design. To give an example no matter how much time have gone into the design of the flap, it will fail, if the sensor fails. Two types of sensors are investigated in the experiment, the variable length Pitot tube sensor and the airfoil pressure tap at 12% chord distance from the leading edge, the Δp sensor shown in Figure 41. Like the first pre-described flap motion experiment the second active control close-loop experiment gave a wealth of results which can be seen in the work of Andersen et al [23].

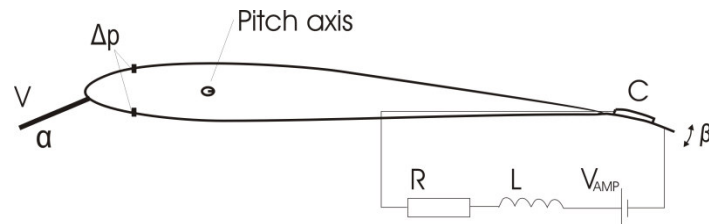


FIGURE 41 ILLUSTRATES CONTROL SENSORS AND THE EQUIVALENT ELECTRIC SETUP.

Investigations are primarily conducted at $Re = 1.0 \times 10^6$, however, two variable frequency pitch experiments are conducted at $Re = 1.6 \times 10^6$. The excitation frequencies used in the experiment correspond to the periodic 1P rotational frequency and the first blade flapwise eigenfrequency of a larger Mega Watt wind turbine. These frequencies contribute significantly to the overall wind turbine dynamics and simulations indicate that the flap is able to alleviate fatigue loads at these frequencies well.

4.2.1 EXPERIMENTAL DESIGN

The blade from a two Mega Watt wind turbine is used as reference to scale the experimental model with a first flapwise eigenfrequency around one hertz, a chord of 1.335 meter (18% thickness) at 75% blade length with a total span of 45 meters. Rated rotor speed of the blade is 0.22Hz (at nominal wind speed 9m/s) which gives a third periodic excitation frequency (3P) close to 0.66Hz. The characteristic velocity is 50m/s. The experimental blade uses the reduced frequency number to scale the dynamics, see Table 11. The reduced frequency is

$$k = \frac{\omega c}{2V} \quad (82)$$

where k is the reduced frequency, c the chord length in meters, ω the angular frequency of unsteady phenomena's in rad/s and V the free wind speed in m/s. In Table 11 the scaling from the reference test turbine to the wind tunnel blade test section is shown.

TABLE 11 SCALING THE DYNAMICS OF THE REFERENCE TURBINE TO THE EXPERIMENTAL SETUP

	reference turbine	experimental model	experimental model
Chord	1.335m	0.66m	0.66m
characteristic velocity	50m/s	25m/s	40m/s
1P load	0.22 Hz	0.22 Hz	0.36 Hz
3P load	0.66 Hz	0.66 Hz	1.07 Hz
1. flapwise eigenfrequency	1 Hz	1.01 Hz	1,62 Hz
Reynolds number (Re)	4.0×10^6	1.0×10^6	1.6×10^6
k (1P)	0.02	0.02	0.02
k (3P)	0.06	0.06	0.06
k (1 flapwise eigenfrequency)	0.08	0.08	0.08

The actuators and the Risø-B1-18 profile used in the experiment is the same as for the first experiment, in which the trailing edge of the non-deformable airfoil actuators were glued to the pressure side. Approximately 25% of the flap was broken probably due to poor storage of the airfoil between the first and the second experiment.

Preliminary tests of the actuators were conducted at Risø by Buhl et al [76] which involve calibration of the strain gauges. The actuator was powered using a Trek PZD700 m/s (200mA) amplifier operating in ranges between -350V to 650V which was slightly less than the first experiment with pre-described flap motion. The controller algorithm was implemented using the programmable automation controller CompactRIO from National Instruments. The CompactRIO was developed by National Instruments and is basically an embedded system, which has a Field-Programmable Gate Array (FPGA) with a real-time 400 MHz Freescale MPC5200 processor which executes LabVIEW Real-Time applications.

Figure 42 gives an overview of the electrical side of the setup in ten points. The airfoil **(1)** has a deformable trailing edge flap **(2)**, which is powered by the **(3)** Trek power amplifier, which again receives a control signal from a PC **(9)**.

On the sensor side the Pitot tube **(4)** has four transducers **(7)** P_6 for absolute pressure, P_1 - P_2 for the center hole in the Pitot tube (not used for control), P_3 - P_4 horizontal holes for the sideslip incidence (not used for control), P_5 - P_6 pressure difference vertical holes (used for control). Two delta pressure taps $\Delta P_{12\%}$, $\Delta P_{50\%}$ **(5)** mounted near the 12.5% chord points measured from the leading edge of the airfoil provides an alternative way of controlling the deformable trailing edge flap. Transducers for the delta pressure taps **(6)**. The transducers have a common 24V power supply **(8)**.

Data are all logged and some are also used by the real time control **(10)** algorithm.

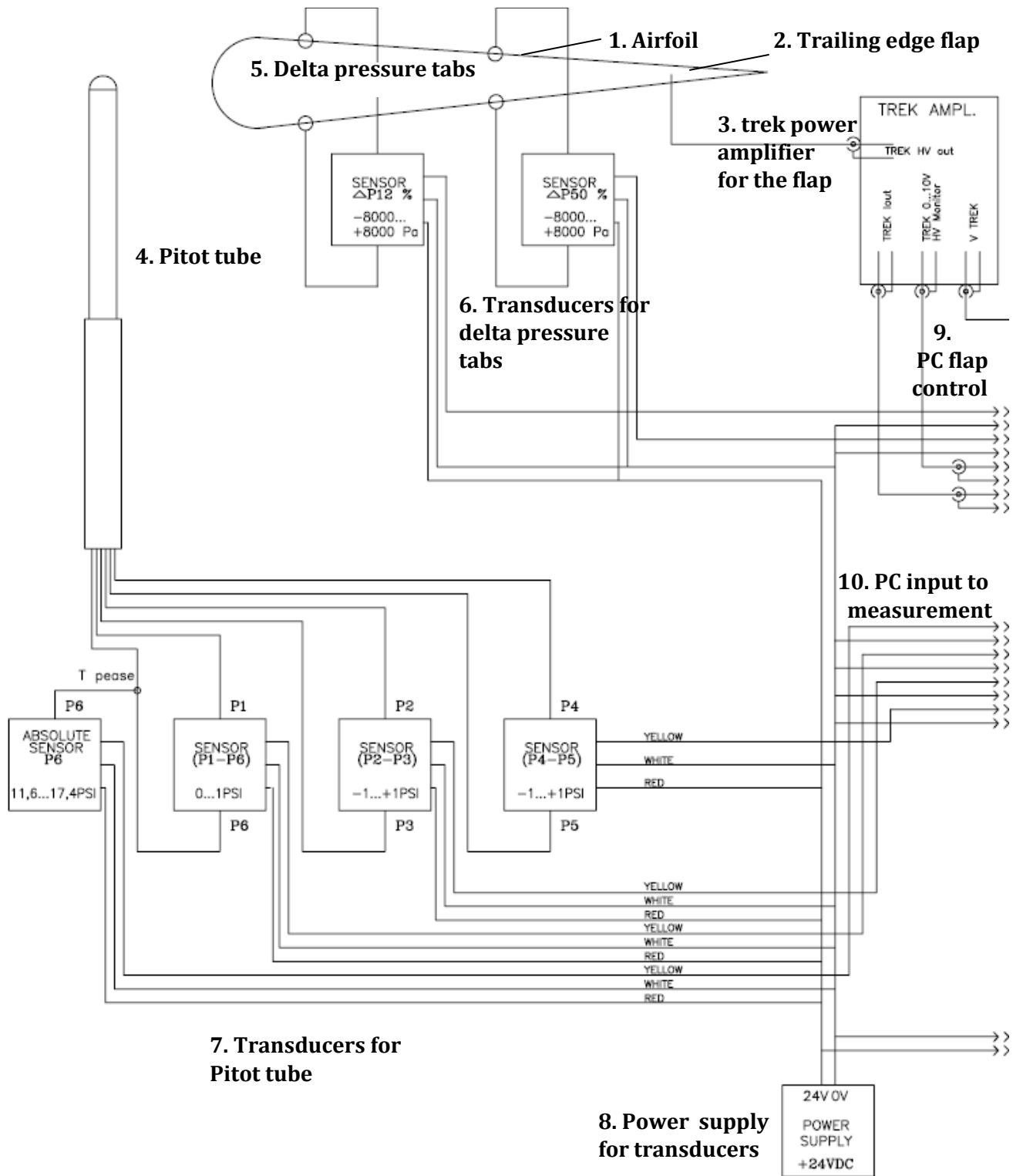


FIGURE 42 DIAGRAM FOR SENSORS AND AMPLIFIER.

CompactRIO is based on a Reconfigurable I/O (RIO) interface technology using LabView. The first LabView program was proposed in the work of Andersen et al [77]. The control algorithm can be broken down in three parts, a filter, an offset and a gain. Two sources of input exist for the controller either through the five-hole Pitot tube $P4-P5$ sensor or through the $\Delta P12\%$ sensor. The filter is a typical first order low frequency pass filter (Butterworth). The offset is given by a running mean sensor value with the purpose of scaling the voltage range so the flap performs using the full voltage range. A proportional gain K_p determines the voltage level sent to the flap actuator through the power amplifier.

4.2.2 PITOT TUBE SENSORS FOR CONTROL INPUT

A variable length Pitot tube was mounted at the leading edge 400mm from the airfoil centerline and used as sensor input for the flap active control. The retractable Pitot tube was tested in three different lengths 330, 580 and 830mm corresponding to 0.50c, 0.88c and 1.26c measured from the point of attachment near the airfoil leading edge, see Figure 43.

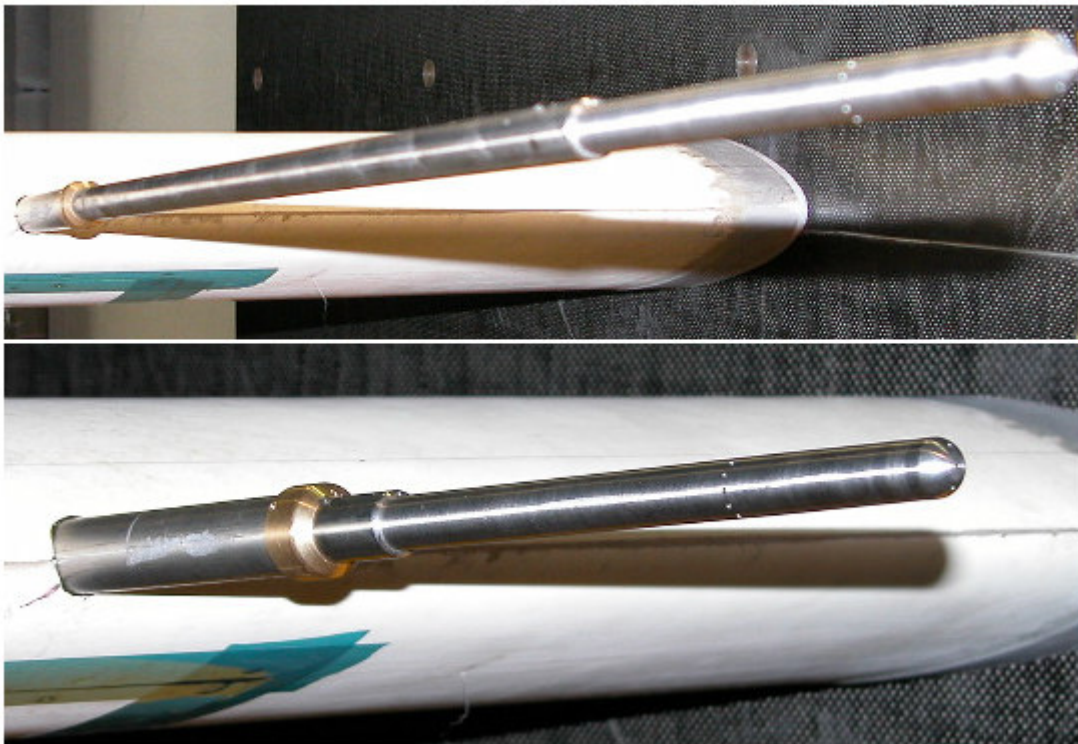


FIGURE 43 (UP) PITOT TUBE FULLY ELONGATED 830MM (DOWN) PITOT TUBE SHORTEST 330MM.

Basic Pitot tube theory was applied to the sensor readings. For high Reynolds number flow past a sphere with sphere diameter as characteristic flow length, the pressure distribution for potential flow by Brown et al [78] is

$$P_{\theta} - P_{\infty} = \frac{1}{2} \rho U^2 \left(1 - \frac{9}{4} \sin^2 \theta \right) \quad (83)$$

where pressure at angle θ is P_{θ} see Figure 44, static pressure is P_{∞} , fluid density ρ .

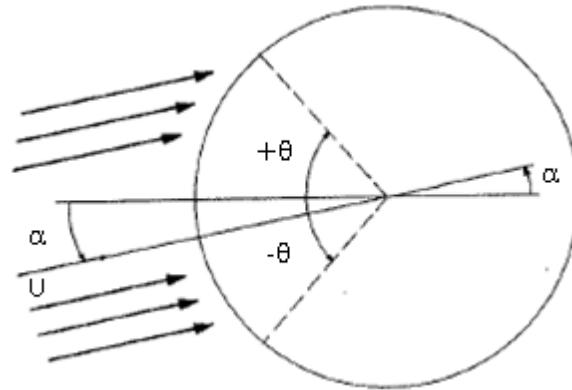


FIGURE 44 SKETCH OF FLOW AROUND A SPHERE, INDICATING INCIDENCE AND PRESSURE TAPS.

By simple normalization with regard to $p = P / \frac{1}{2} \rho U^2$ the two pressure tube holes at angle $\pm \theta$, can be written as

$$p_{+\theta} - p_{\infty} = 1 - \frac{9}{4} \sin^2(\theta + \alpha) \quad (84)$$

$$p_{-\theta} - p_{\infty} = 1 - \frac{9}{4} \sin^2(\theta - \alpha) \quad (85)$$

combining the two pressure tube tap equations

$$\Delta p = p_{+\theta} - p_{-\theta} = -\frac{9}{4} \sin(2\theta) \sin(2\alpha) \quad (86)$$

As illustrated in Figure 42, the two pressure taps for the Pitot tube is labeled sensor $P4$ and $P5$, the difference between the two taps will from now on be referred to as $p4-5$. The sphere surface angle was measured to $\theta = 38.8^\circ$, isolating the incidence angle gives the flowing equation

$$\alpha = -\frac{1}{2} \sin^{-1} \left(p_{4-5} \frac{4}{9} \frac{1}{\sin(2\theta)} \right) \quad (87)$$

The incidence measured with the Pitot tube has been compared with the airfoil pitch motor in Figure 45. The figure illustrates divergence for high incidence angles above 15° . This is due to the influence of the airfoil, which is mostly felt by the Pitot tube when it 330 mm long.

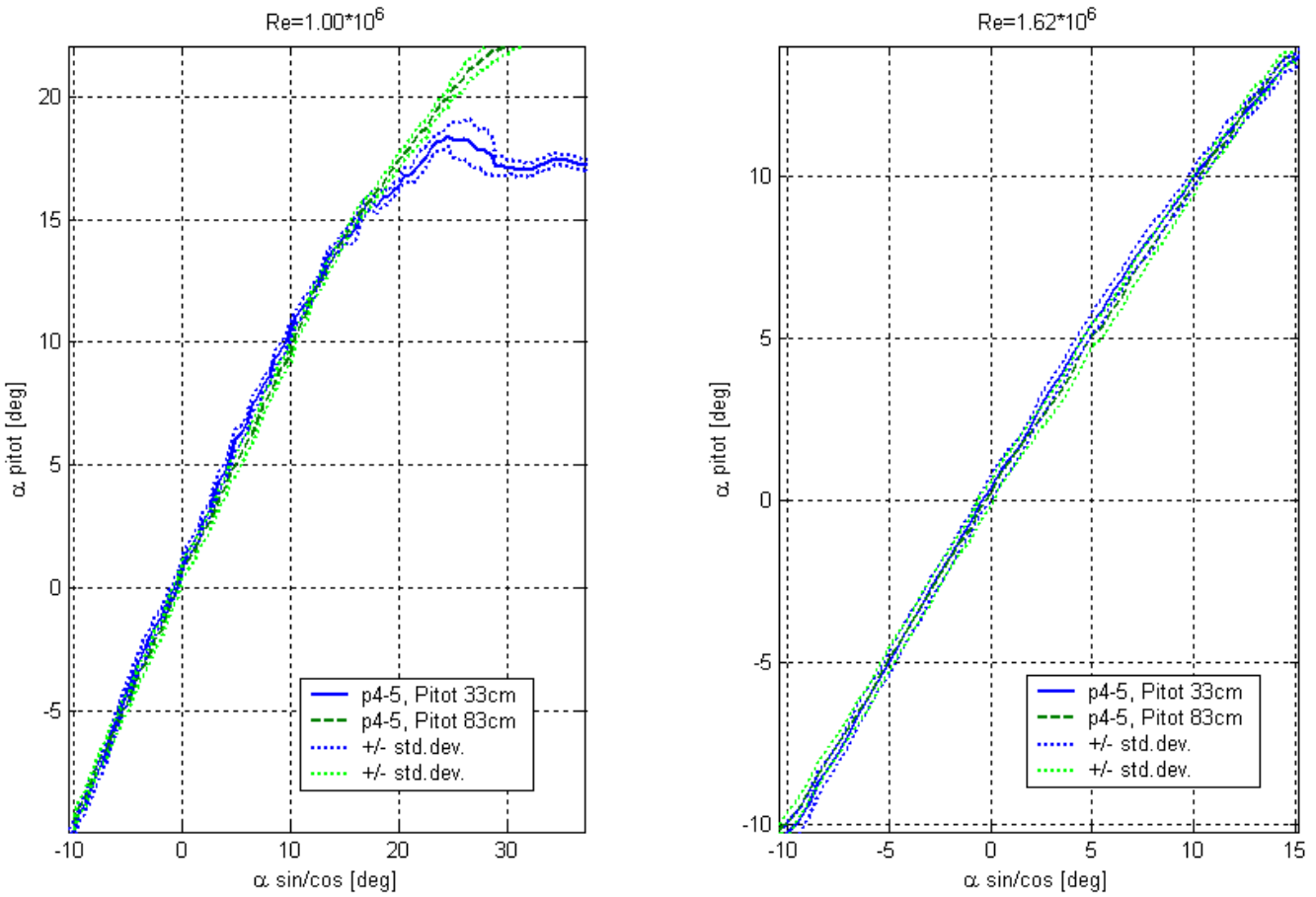


FIGURE 45 SHORT AND LONG PITOT TUBE COMPARED WITH AIRFOIL INCIDENCE SENSOR, (LEFT) $Re=1.0 \cdot 10^6$ (RIGHT) $Re=1.6 \cdot 10^6$. IN AVERAGE THERE ARE 500 MEASUREMENTS PER BIN AND FOUR BINS PER DEGREE INCEDENCE.

For the unsteady measurements the eigenmotion of the Pitot tube will appear in the measured incidence signal due to the pitching of the airfoil. However, as the airfoil pitch rate is known the eigenmotion contribution can be determined.

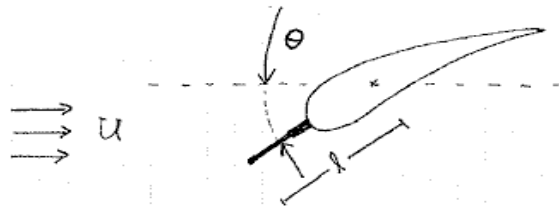


FIGURE 46 AIRFOIL WITH PITOT TUBE AND PITCH ANGLE.

Consider an airfoil like Figure 46 where the pitch angle is given by the harmonic function

$$\theta(t) = \sin(\omega t + \varphi) \quad (88)$$

in which the phase angle is φ , and ω is the pitching rate in radians per second. When the profile pitches downwards there will be a pitch rate given by

$$\frac{\partial\theta(t)}{\partial t} = \dot{\theta}(t) = \omega \cos(\omega t + \varphi) \quad (89)$$

As the distance from pitch axis to tip of Pitot tube is l , the incidence due to airfoil eigenmotion α_i will be

$$\alpha_i = \tan^{-1}\left(\frac{\dot{\theta}l}{U}\right) \approx \frac{\dot{\theta}l}{U} = \frac{\omega l}{U} \cos(\omega t) = \frac{\omega l}{U} \sin\left(\omega t - \frac{\pi}{2}\right) \quad (90)$$

so there is a 90 ° phase angle shift between the geometric incidence and the incidence which is due to the eigenmotion of the airfoil. The overall effect of the eigenmotion is shown in Andersen et al [23] for the fully elongated and the shortest possible Pitot tube, the 830mm and 330mm respectively. No effort was made to remove the eigenmotions from the control sensor signal. The typical magnitude of α_i for 330mm and 830mm Pitot tube at five different reduced frequencies can be seen in Table 12.

TABLE 12 MAGNITUDE OF THE AIRFOIL EIGENMOTION, α_i , FOR FIVE REDUCED FREQUENCIES AND TWO PITOT TUBE LENGTHS. UNITS ARE IN DEGREES.

k	0.021	0.041	0.062	0.083	0.139
330mm Pitot tube, α_i=	1.8 ⁰	3.5 ⁰	5.1 ⁰	6.9 ⁰	11.7 ⁰
830mm Pitot tube, α_i=	3.0 ⁰	5.8 ⁰	8.7 ⁰	11.7 ⁰	19.6 ⁰

For a long Pitot tube with a the fast the harmonic pitch, compared to a short Pitot tube with a show harmonic pitch there should be a significant difference in the phase lags between measured incidence and actual incidence. The load reduction potential is expected to be affected by any phase lags including the effect of the airfoil eigenmotion.

4.2.3 AIRFOIL DELTA PRESSURE TAP SENSOR FOR CONTROL INPUT

Analysis using unsteady thin airfoil potential flow theory suggests that measurement of the pressure difference between the airfoil suction and pressure side at a single chordwise position is a good estimation of the unsteady lift. Gaunaa [29] derived a model applicable for airfoils equipped with active control devices which can be described by unsteady deformable camberlines. The unsteady pressure difference over the airfoil is closely related to the integral lift force hence the unsteady lift will be estimated using a single pressure difference measurement. This principle for smart rotor control was described by Gaunaa & Andersen [52].

In order to evaluate the load reduction potential for the proposed sensor and control method, simulations with the same 2D setup as in the original work of Buhl et al [13] was used. Simulations and re-examination of the first measurement campaign both suggested placing the pressure difference flap control sensor close to 12% from the leading edge. A delta pressure difference taps was mounted

on the airfoil at the 12% chord point, measured from the leading edge, and 340mm from the airfoil centerline. In Figure 47, results from the prescribed flap motion experiment conducted with harmonic trailing edge flap deformations at the reduced frequency $k=0.02$ close to minus two degree incidence is shown.

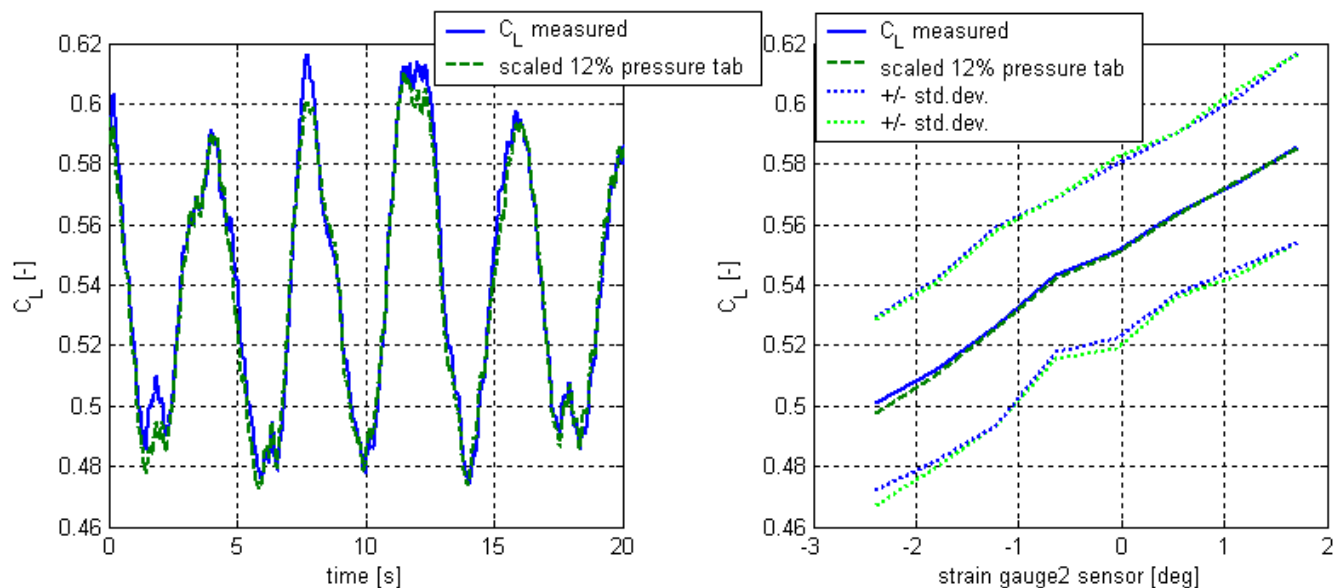


FIGURE 47 (LEFT) TIME SERIES WITH INTEGRAL C_L COMPARED TO AIRFOIL 12% DELTA PRESSURE TAPS CONTROL SENSOR (RIGHT) BINNED INTEGRAL C_L AND AIRFOIL 12% DELTA PRESSURE TAPS FOR COMPARISON. ON AVERAGE THERE ARE 200 MEASUREMENTS PER BIN AND 16 BINS PER DEGREE FLAP ANGLE.

The integrated lift coefficient is shown and compared to the 12% airfoil pressure tap control sensor scaled using a proportional factor at a set offset. Figure 47 illustrates a near perfect correlation between integrated C_L and 12% airfoil delta pressure point value. Furthermore for the reduced flapping frequency at $k=0.02$ the assumption of disregarding unsteady aero-, mechanical- and electric-dynamics is valid. The standard deviation in measured and integrated C_L is large; around 0.03, see Figure 47 (right). This is assumed to be an effect of the high wind tunnel turbulence level.

4.2.4 ACTIVE CLOSED-LOOP FLAP CONTROL RESULTS

After having investigated the sensor signals, the focus shifts towards the controller. The first results presented in this section involve variations in the fatigue load reductions when applying different low frequency filters to the control input signal. Next, results from a comparison between different controllers, sensors and control gains will be presented. Hereafter, the performance of the controller will be tested at different incidences, followed by investigations conducted using variable frequency pitch excitation and finally system phase lags will be identified and presented.

4.2.4.1 THE SIGNAL FILTER

All wind tunnels are subject to turbulence and this turbulence will, when untreated, pass directly through the controller to the trailing edge flap deflection.

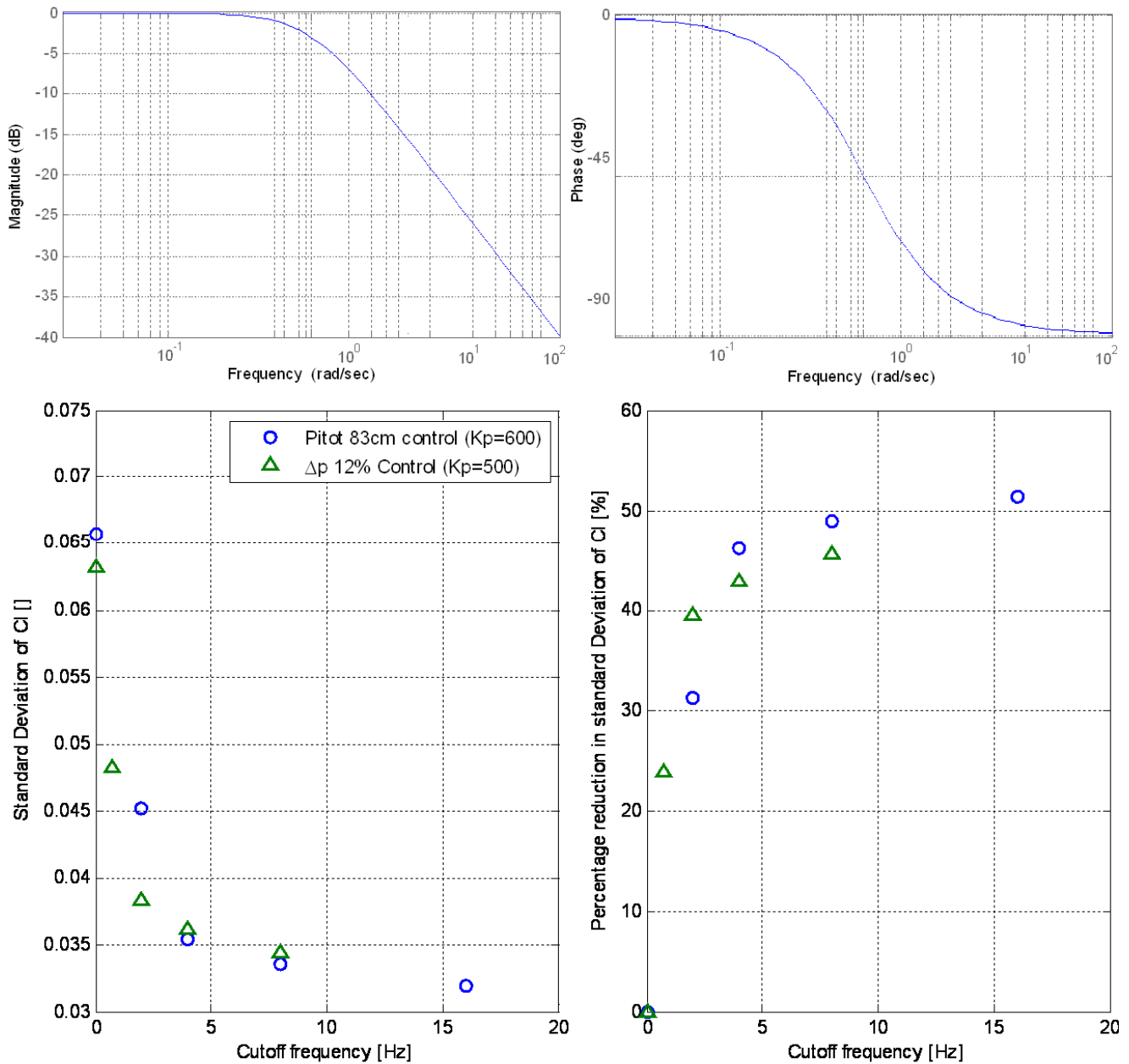


FIGURE 48 (UP) FIRST ORDER LOW FREQUENCY PASS FILTER (LEFT) AMPLITUDE AND (RIGHT) PHASE RESPONSE (DOWN) LOAD REDUCTION POTENTIAL AS FUNCTION OF CUTOFF FREQUENCY FOR THE LOW FREQUENCY PASS FILTER (LEFT) STANDARD DEVIATION OF C_L (RIGHT) PERCENTAGE REDUCTION FROM UNCONTROLLED CASE.

A scaled model, not previously described, was made¹⁰. This model has four ceramic piezoelectric elements attached, these four piezoelectric elements can move according to aero-elastic simulated HAWC2 [25] trailing edge flap deflections. This very crude model has shown a clear tendency to cause damage to the Thunder actuators when the input signal has high frequency content. Both the power amplifier and imperfections in the piezoelectric material has been under suspicion. This undocumented observation along with the high frequency content in the Velux tunnel, in particular at 4Hz shown in Figure 40 Chapter 4.1, has lead to adding a low-pass, Butterworth type, first order filter in the control.

The frequency response and phase shift of the filter are shown in Figure 48, along with fatigue load reduction plotted against filter cutoff frequency. The default filter cutoff frequency is 4Hz which offers some protection against high frequency tunnel disturbances without introducing too much phase lag for the investigated reduced harmonic pitching frequencies. Although 4Hz is the default value used, some experiments perform a parameter sweep of this parameter.

¹⁰ The model can still be seen at the author's desk

4.2.4.2 COMPARISON OF CONTROLLERS USING DIFFERENT SENSOR INPUT

Initially the active control experiment had two parameters which needed to be estimated, the filter cutoff frequency and the proportional gain K_P linking the electric and the mechanical side of the experiment. Figure 49 combines the K_P parameter investigation using the active controller with four different types of sensor input, the three different Pitot tube lengths 330mm, 580mm, 830mm and the 12% airfoil pressure tap sensor. Load reductions are calculated for 3 minute series, $Re=1.0 \times 10^6$ at the reduced pitching frequency $k=0.0625$. The difference in peak to peak incidence for the harmonic pitch motion is 2 degrees.

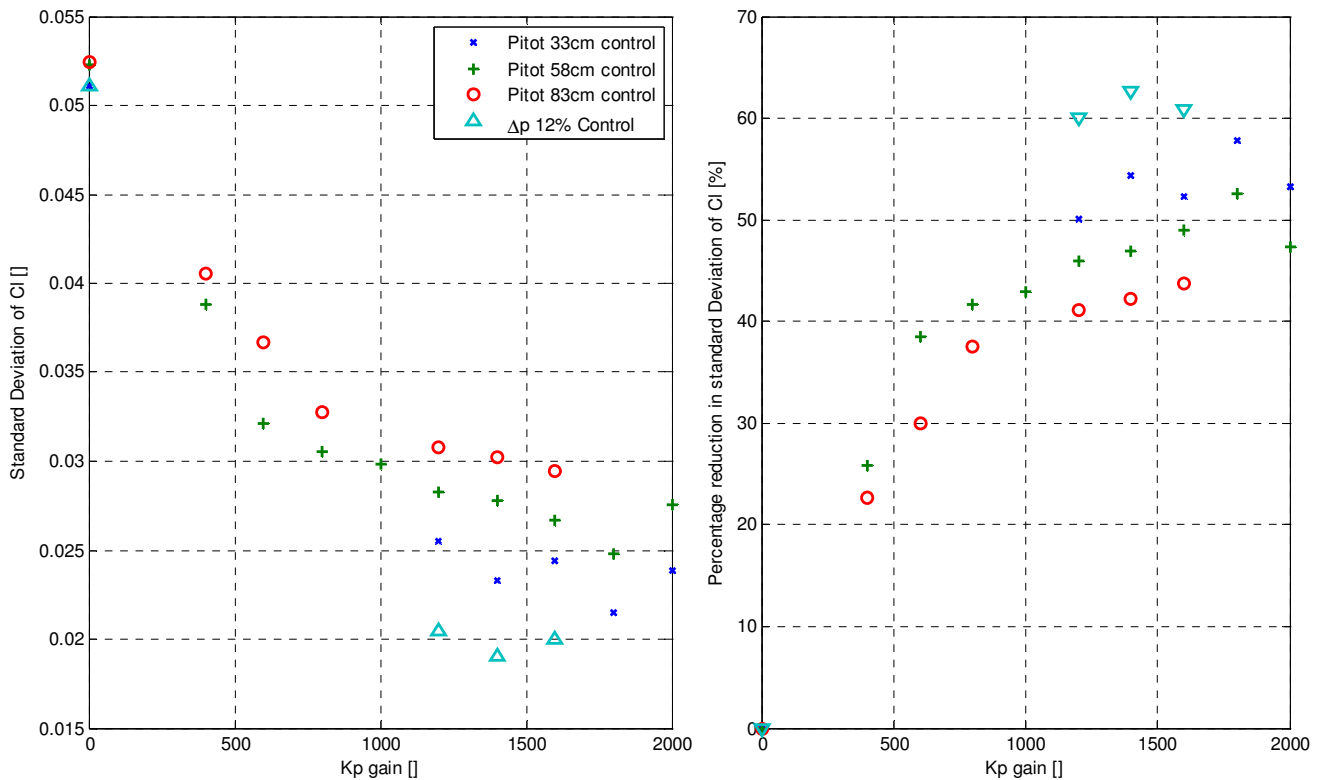


FIGURE 49 VARYING CONTROL GAINS FOR LOAD REDUCTION USING DIFFERENT CONTROL SENSORS (LEFT) STANDARD DEVIATION VALUES (RIGHT) PERCENT REDUCTIONS COMPARED TO THE CASE WITH NO CONTROLLED FLAP.

The effect of the airfoil eigenmotion, previously described, is a reason for the difference in load reductions for the Pitot tube controllers. For instance at $K_p=1200$ in Figure 49 the long Pitot tube gives 41% reduction and the short Pitot tube gives 50% reduction. In Table 12 the reduced frequency of 0.062 gives a difference in phase angle from 5.1° to 8.7° depending on using the short or the long Pitot tube. It is likely that the Pitot tube would perform better than the 12% chord airfoil pressure tap as control input, if the effect of the airfoil eigenmotion was removed from the Pitot tube signal. This remains to be seen in some future work. A mechanism developed in LabView restrained the amplifier from exceeding the range from -350 to 650 Volts. This protective mechanism has the side effect that the flap response becomes a square wave for K_P gains greater than 1000. Six different gains have been chosen for the closed loop flap controller. This is shown in Figure 50, where the controller

attempts to keep the lift close to constant while the airfoil is subject to a harmonic reduced pitching frequency $k=0.02$.

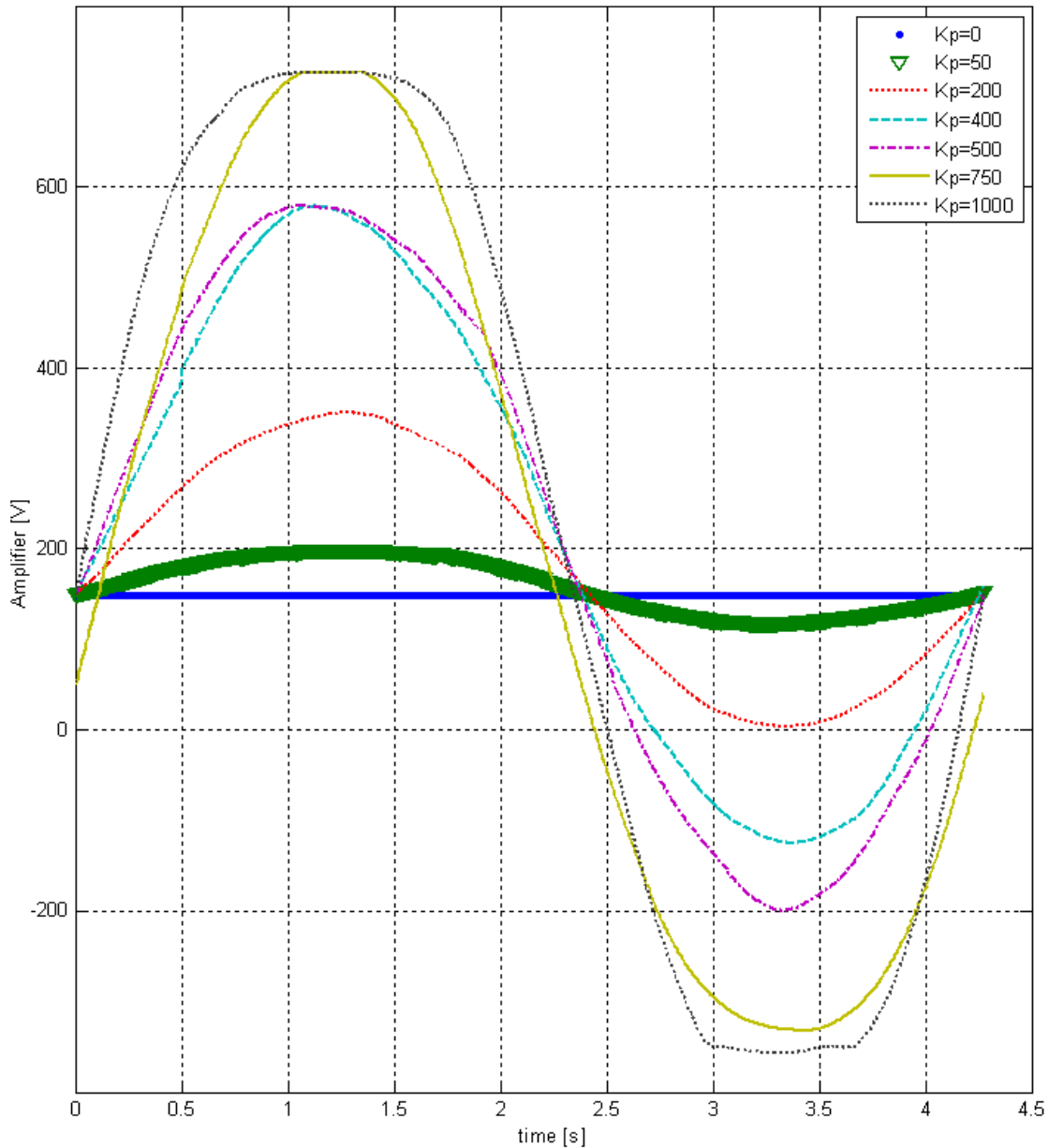


FIGURE 50 CONTROL USING THE SHORT PITOT TUBE AND VARYING THE PROPORTIONAL GAIN.

While the effect of the harmonic reduced pitching frequency is removed using the active flap control, it is important to understand that the load reduction obtained using the square wave signal may exceed that of a truly stochastic disturbance. If the control is too slow in responding, a square wave will catch up with a harmonic disturbance. However, if the pitch motion decided half cycle to change direction the square wave flap motion would need more time to adapt compared to a non square wave control using low K_P gains. Another reason that the square wave control performs better is that it

compensates the lack of flap control authority caused by the, approximately 25%, piezoelectric flap elements being broken. The results in Figure 49 should be analyzed with this in mind, especially gains greater than 1800 have a near perfect square form.

4.2.4.3 CONTROL PERFORMANCE AT DIFFERENT INCIDENCES

The flap control is intended for a variable speed pitch regulated wind turbine. The flaps have to be able to perform at the near constant incidence when the wind turbine is operating in low wind speed at optimum tip-speed ratio, but also at lower incidences when the turbine is power regulating during high wind speed operation. The results shown in Figure 51, illustrates that the flap control performs well for a range of incidences basically throughout the attached flow regime of the airfoil. The difference in peak to peak incidence for the harmonic pitch motion is 2 degrees.

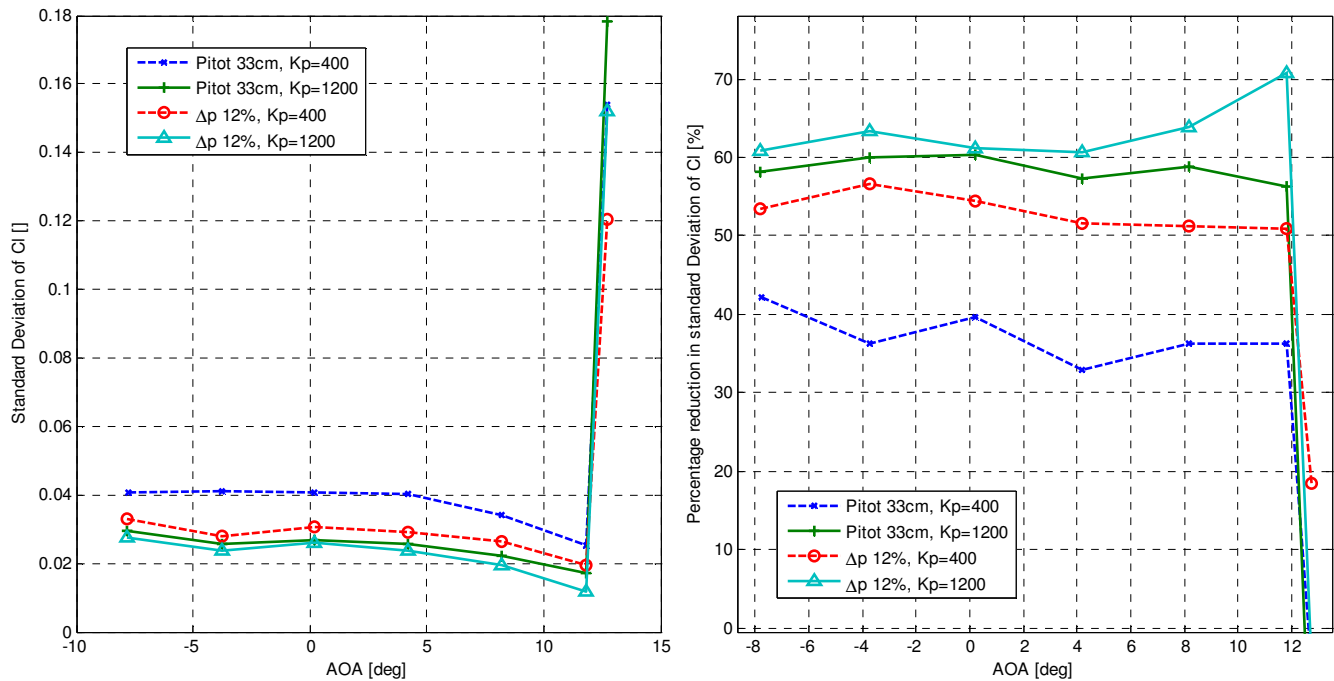


FIGURE 51 EFFECT ON THE LOAD REDUCTION POTENTIAL BY VARYING THE INCIDENCE FOR DIFFERENT CONTROL SENSORS FOR $RE=1.0 \times 10^6$ AND AT A REDUCED PITCHING FREQUENCY OF 0.0625.

There is a tendency of slightly greater load reductions at incidences close to stall for the 12% airfoil pressure tap sensor with high gain. However, once the stall regime is reached the flap no longer performs well in terms of reducing the loads. This feature could very well be incorporated in a future smart blade airfoil control integrated design. Another striking feature is the fact that the 12% airfoil pressure tap sensor performs better than the retracted Pitot tube sensor for all incidences in the attached flow regime.

4.2.4.4 VARIABLE FREQUENCY PITCH MOTION

To investigate the flap response of the airfoil which were not purely sinusoidal in pitch with constant frequency, a test was carried out, where a sinusoidal pitch motion with varying frequency was used.

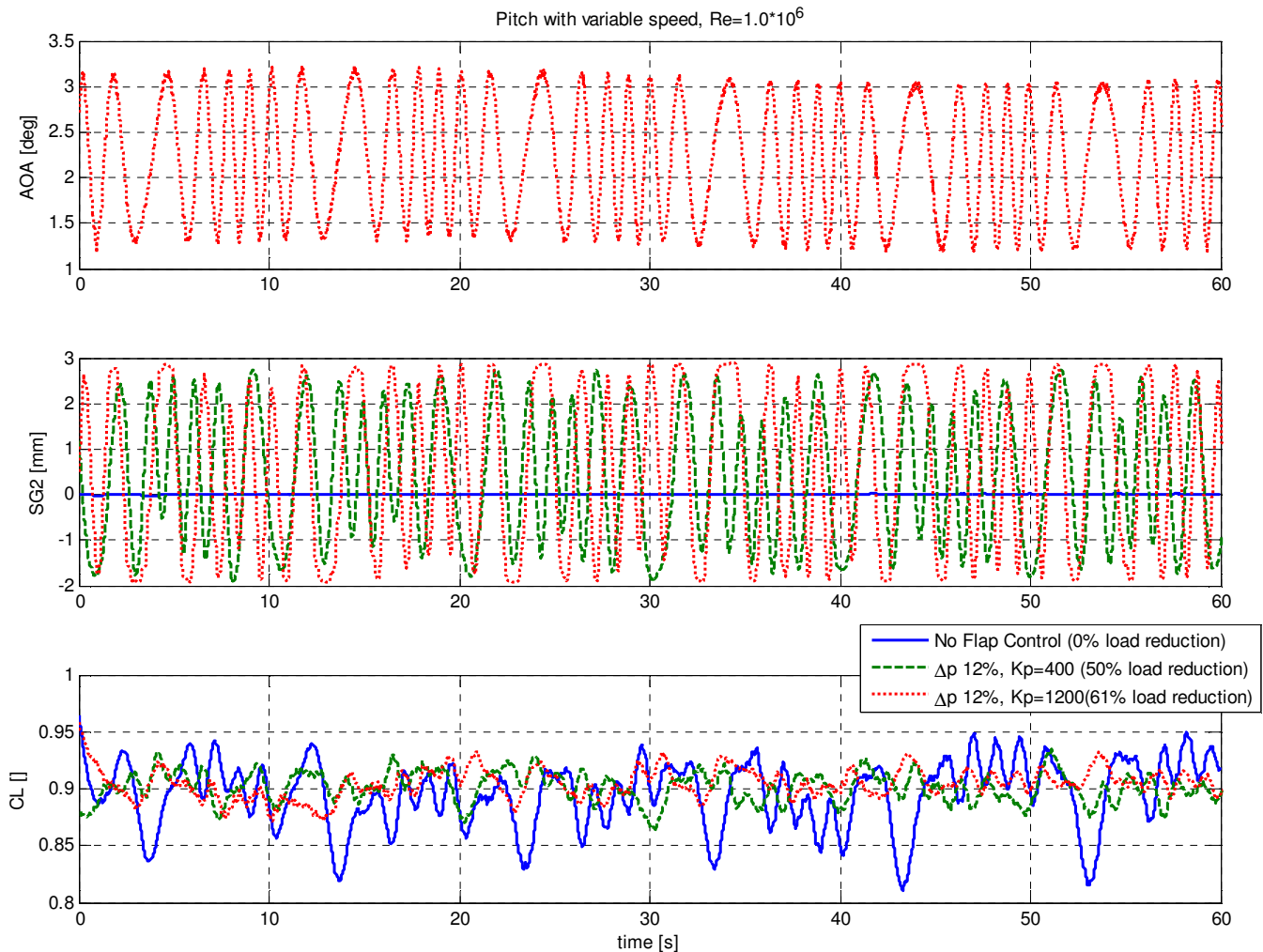


FIGURE 52 (TOP) VARYING FREQUENCY OVERLAID HARMONIC PITCHING SIGNAL, (MIDDLE) STRAIN GAUGE SIGNAL FROM STRAIN GAUGE 2 SENSOR, (BOTTOM) CL SIGNAL COMPARISON BETWEEN NO CONTROL AND CONTROLLERS USING THE $\Delta P12\%$ SENSOR.

The frequency ranges covered by the superposed pitch actuator corresponds to frequencies from 0.22Hz (1P) up to and well beyond the flapwise eigenfrequency. This correspond to the reduced frequencies from $k=0.013$ to $k=0.139$ with 1.90° peak to peak pitch amplitude, where the low frequency performed almost quasi-steady oscillations. The sensor/actuator system was tested for flow conditions containing several frequencies due to different distinct frequencies in the turbulence intensity in the wind tunnel and in the pitching motion of the airfoil. In Figure 52 3 one minute extracts are shown; one for the uncontrolled case with the lift coefficient variation to give an impression of the variation in load and two with the active closed loop controller active. There is a 61% reduction in the

standard deviation of the C_L signal for the three minute series. Although a variable airfoil pitch rate is used, the pitch motion cannot be considered stochastic, when using high gains K_P typically above 1000, the control offers greater load reduction as the flap motion has a square step shape than when using lower gains typically 400. Because the overall superposed pitch motion is harmonic the aggressive or high proportional gain for the flap control forces the flap to quickly follow the harmonic pitch motion. If the motion is truly stochastic there may be lift overshoots caused by the use of too high gains. In a future experiment the possibility to generate turbulence, perhaps using a grid, may be an interesting option.

4.2.4.5 PHASE LAGS IN THE LOOP

Spectral analysis was applied to five experiments at various reduced pitching frequencies. Without the active control the phase shift at airfoil pitching frequency was calculated using a phase transfer function in a post processing tool called WinDap¹¹ used at Risø-DTU, and converted into milliseconds. The references used for the phase shifts are the airfoil pitch motion and the control signal from the PC. A harmonic pre-described flap motion experiment from the first VELUX measurement campaign has also been analyzed. In Table 13 the phase lags from the five pre-described pitch motion experiments and one pre-described flap motion experiment have been compiled and tabulated to give an overview of the system time lags.

TABLE 13 PHASE LAGS IN MILLISECONDS FOR SENSORS, AMPLIFIER AND FLAP DEFLECTION

Reduced pitching frequency, $k=$	0.139	0.083	0.062	0.041	0.021	<mean>
Airfoil pitch ¹²	0	0	0	0	0	0
$\Delta p_{12\%}$ - control sensor	5	5	5	5	5	5
C_L - integrated value	35	25	30	30	30	30
$\Delta p_{50\%}$ - control sensor	35	35	35	40	40	37
Pitot tube 330mm – control sensor		55	60			58
Pitot tube 580mm – control sensor		70	70			70
Pitot tube 830mm – control sensor	85	80	80	80	80	81
Reduced flapping frequency, (Please note, taken from the first VELUX measurement campaign)	$k= 0.040$					<mean>
Control signal-out ⁶						0
V_{AMP} (Flap up)						20
Strain gauge 2 (Flap up)						25
V_{AMP} (Flap down)						10
Strain gauge 2 (Flap down)						15

¹¹ 'WinDap' is a post processing tool for measurements and simulations performed in HAWC2 among others.

¹² Phase zero reference point or 0°

The table contains two sets of phase lags. The top part of Table 13 focuses on comparing the time it takes to register changes in the control sensors from the airfoil pitch motion. The pitch signal is used as a reference or zero phase. The bottom part of Table 13 focuses on the electrical part of the experiment, using the signal-out as reference time or zero phase. The table gives an estimate of the time between the airfoil pitch motions or the control signal out to a given sensor starts registering the change. To give an example of how to use Table 13, focus on the “ C_L – integrated value” at the reduced pitching frequency $k=0.139$, the table field gives a delay time of 35 milliseconds. This is the time it takes from the pitch motion peak to the C_L integrated value peak. Table 13 shows that the eigenmotion of the Pitot tube plays a significant role in introducing phase lags in the control; in average it takes the fully elongated Pitot tube 16 times longer to determine the change in input signal compared to the 12% airfoil pressure tap sensor.

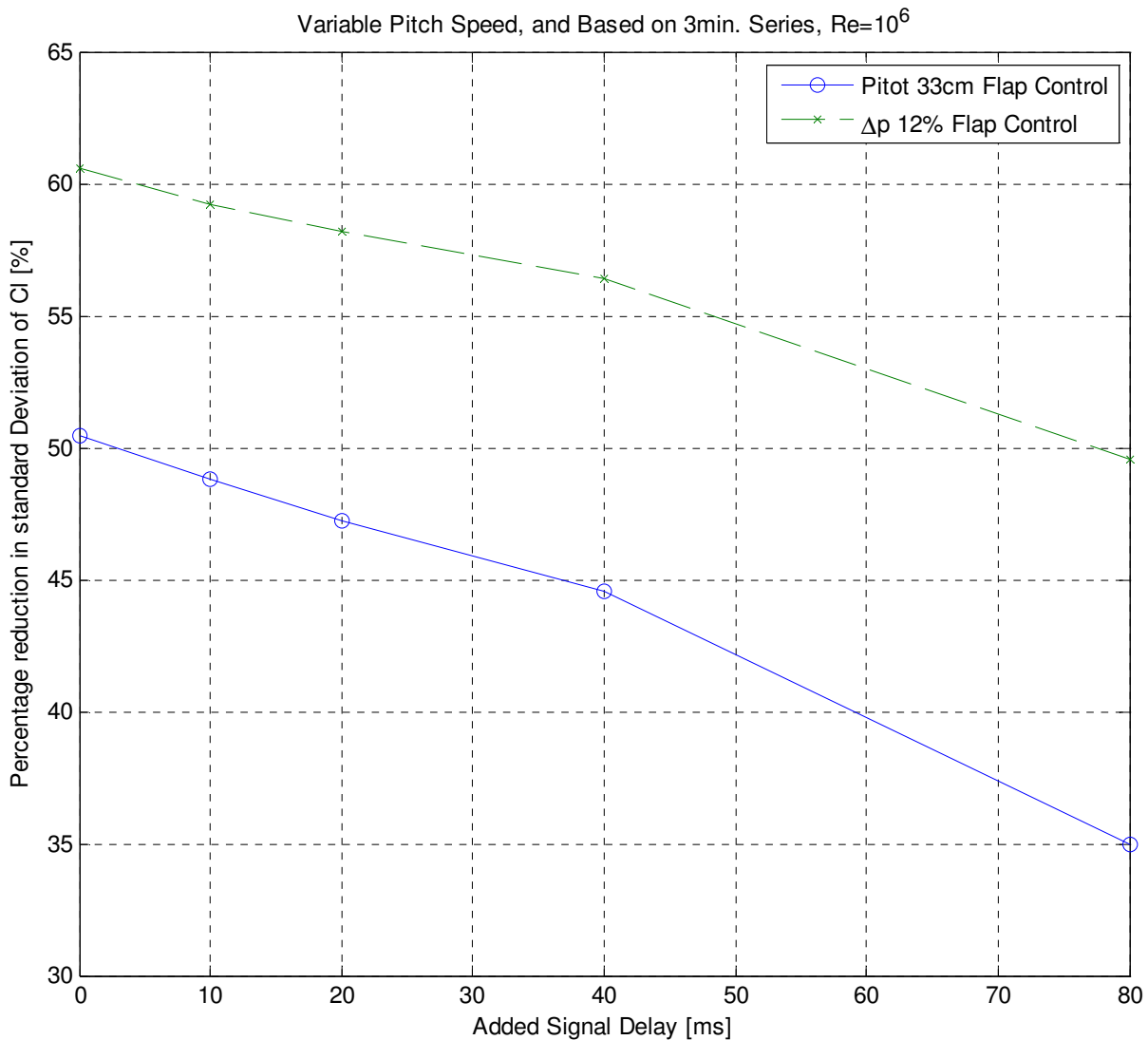


FIGURE 53 LOAD REDUCTION POTENTIAL AS FUNCTION OF ADDED SIGNAL DELAY.

During the second measurement campaign in VELUX an extension to the active control algorithm made it possible to add additional delays in the control loop. This modification made it possible to investigate how much the load reduction potential depended on a fast response and how robust it is to additional signal delays. An extension to the variable frequency pitch actuation experiment, shown in Figure 52, in the form of a time delay parameter have been implemented and signal delays ranging from 0ms to 80ms for the 330mm Pitot tube sensor control and the 12% airfoil pressure taps sensor control can be seen in Figure 53. Both types of control experience a drop in percentage load reduction, however the Pitot tube drops almost 50% more in percent points compared to the 12% airfoil pressure tap control when introducing 80ms added signal delay into the system.

4.2.5 CONCLUSIONS OF THE SECOND EXPERIMENT

The closed loop experiment was successfully setup. The experimental setup included sensors, controllers and a deformable trailing edge flap.

The flow angle from the Pitot tube and a pressure difference at 12% chord taken from the leading edge was measured. The airfoil was harmonically pitched at different frequencies to approximate the unsteady environment for an airfoil section on a wind turbine. A controller which consists of a low pass filter and a proportional gain was used. The airfoil pitching motion was not used by the controller, thus only sensing the change in incidence. The objective for the controller was to keep the lift constant.

The main findings are

- The flow angle from the Pitot tube correlates with the airfoil incidence.
- A pressure difference between suction and pressure side at 12% correlates with the lift.
- The control algorithm based on the Pitot tube and the pressure difference was able to control the flap well when the objective is to minimize the standard deviation in lift.
- Reductions in the standard deviation of the lift coefficient greater than 60% has been achieved for the 12% chord airfoil pressure tap setup for both constant and varying frequency sinusoidal motion.
- Reductions in the standard deviation of the lift coefficient greater than 50% have been achieved for the Pitot tube setup for both constant and varying frequency sinusoidal motion.
- No effort was made to remove the eigenmotion of the Pitot tube. It is likely that the Pitot tube would perform better than the active control based on the 12% chord airfoil pressure tap control sensor if a system was devised which removed the effect of the Pitot tube eigenmotion.
- When adding additional time delays around 80ms the load reduction potential dropped from above 60% to just below 50% for the 12% pressure tap sensor. Whereas, the Pitot tube sensor dropped to 35% from 50%, showing slightly more sensitivity to additional signal delays.
- An overview of which components in the sensor-transducer-controller-amplifier-actuator-aerodynamic-reponse chain of events has been provided in Table 13.

It should be noted that the load reductions obtained in this experiment should be higher if the flap had had more control authority. Approximately 25% of the flap was broken probably due to poor storage of the airfoil between the first and the second experiment.

5.1 CONCLUSION AND RECOMMENDATIONS

The work carried out over the past three years within this PhD has contributed to new knowledge both experimentally and model wise. This has been emphasized through discussions internationally, presentations at conferences with the industry.

Three milestones were formulated in the introduction.

- **Milestone one.** Derive two aerodynamic models for the deformable trailing edge flap which take into account viscosity and effects of the near wake.
- **Milestone two.** Design and formulate control algorithms for the trailing edge flaps for use on full scale wind turbines.
- **Milestone three.** Conduct a 'proof of concept' closed-loop control wind tunnel experiment. Two new types of sensor inputs for the controller were used.

The first, second and third milestones has been reached.

MODEL (milestone one and two)

On the modeling side a new dynamic stall model has been developed. The model predicts the unsteady aerodynamic forces and moments on an airfoil section undergoing arbitrary motion in heave, lead-lag, pitch and trailing edge flapping. For the separated flow region this dynamic stall model becomes a crossover between the inviscid model of Gaunaa [29] and the model of Hansen et al [30] which include the effect of flow separation.

The near wake model originally proposed by Beddoes [38], investigated by Madsen & Rasmussen [37] was extended by the work of Wang & Coton [40] and implemented in the aeroservoelastic tool HAWC2 [25]. An improved approximation to the analytical trailed vorticity filament is proposed through several indicial terms with optimized coefficients.

The potential of the deformable trailing edge flaps with regard to reducing the equivalent fatigue load were investigated. The effect of flaps mounted on 10%, 20%, 30% and 60% of the total blade length was investigated.

Three different controller and sensors concepts were investigated. Controllers based on strains as input were investigated to control the flap. Also Pitot tubes, measuring the dynamic inflow, were used to control the flap. Finally a combination of strain and inflow sensors has been combined with a traditional collective pitch variable rotor speed power controller.

Simulations conducted on the five Mega Watt reference turbine from the UpWind project suggest that fluctuations in the blade root moment due to turbulent inflow conditions can be reduced 40% when three flaps per blade are used which corresponds to 30% of the blade length.

The controllers were tested in a typical wind farm scenario, where turbines are subject to meandering wakes from upstream turbines. A turbine, placed in the second row in the wind farm. The smart control, represented by the deformable trailing edge flaps, provided an additional equivalent load reduction in the flapwise root moment of 60%.

EXPERIMENT (milestone three)

The closed loop experiment was successfully setup. The experimental setup included sensors, controllers and a deformable trailing edge flap.

The flow angle from the Pitot tube and a pressure difference at 12% chord length from the leading edge was measured. The airfoil was harmonically pitched at different frequencies to approximate the unsteady environment for an airfoil section on a wind turbine. A controller which consists of a low pass filter and a proportional gain was used. The airfoil pitching motion was unknown by the controller, thus only sensing the change in incidence and airfoil pressure difference. The objective for the controller was to keep the lift constant.

The main findings were

- The flow angle from the Pitot tube correlates with the airfoil incidence.
- A pressure difference between suction and pressure side at 12% chord length correlates with the lift.
- The control algorithm based on the Pitot tube and the pressure difference was able to control the flap well for the chosen operational incidence range when the objective is to minimize the standard deviation in lift.
- Reductions in the standard deviation of the lift coefficient greater than 60% has been achieved for the 12% chord airfoil pressure tap setup for both constant and varying frequency sinusoidal motion.
- Reductions in the standard deviation of the lift coefficient greater than 50% have been achieved for the Pitot tube setup for both constant and varying frequency sinusoidal motion.
- When adding additional time delays in the neighborhood of 80ms, the load reduction potential dropped from above 60% to just below 50% for the 12% pressure tap sensor. The Pitot tube sensor dropped to 35% from 50%, showing slightly more sensitivity to additional signal delays. No effort was made to remove the eigenmotion of the Pitot tube.

FUTURE WORK

Stability and model prediction style controllers which integrate more advanced models have not been investigated in this work. This still remains an important research area for future work. Model validation was carried out during the past three years but remains a research area which could get more attention in general. Comparison with other aeroelastic codes which has a model for the deformable trailing edge flap is important. Corporation between Delft Technical University and Risø DTU has carried out a comparison between two different flap models [79] however more work needs to be done in this field. Full load cases for onshore and off-shore modern megawatt size turbines needs to be conducted, the tools for conducting these experiments have now become available through the work conducted in milestone one and three.



FIGURE 54 PICTURE FROM THE VELUX WIND TUNNEL. (FROM TOP LEFT) RENE MØLLER, KASPER CLEMMENSEN, PER HANSEN, CHRISTIAN BAK (FROM BOTTOM LEFT) PETER BJØRN ANDERSEN, MAC GAUNAA, THOMAS BUHL.

The work presented here is part of the ADAPWING II project sponsored by The Danish Council for Independent Research | Technology and Production Sciences¹³.

¹³ in Danish; Det frie forskningsråd, teknologi og produktion

APPENDIX

Appendix A: Gaunaa's shape integrals.

Appendix B: C_M comparison.

Appendix C: Wind tunnel setup drawings and photos.

Appendix D: Strain gauge number 1-4 sensor placements for wind tunnel experiments.

APPENDIX A: GAUNAA'S SHAPE INTEGRALS

The following equations are to be found in the work of Gaunaa [29].

$$F_y = \int_{-1}^1 \int_{-1}^1 y \cdot \ln \left(\frac{(x - \varepsilon)^2 + (\sqrt{1 - x^2} - \sqrt{1 - \varepsilon^2})^2}{(x - \varepsilon)^2 + (\sqrt{1 - x^2} + \sqrt{1 - \varepsilon^2})^2} \right) d\varepsilon dx \quad (\text{A.1})$$

$$F_{dydx} = \int_{-1}^1 \int_{-1}^1 \frac{\partial y}{\partial X} \ln \left(\frac{(x - \varepsilon)^2 + (\sqrt{1 - x^2} - \sqrt{1 - \varepsilon^2})^2}{(x - \varepsilon)^2 + (\sqrt{1 - x^2} + \sqrt{1 - \varepsilon^2})^2} \right) d\varepsilon dx \quad (\text{A.2})$$

$$G_y = \int_{-1}^1 x \int_{-1}^1 y \cdot \ln \left(\frac{(x - \varepsilon)^2 + (\sqrt{1 - x^2} - \sqrt{1 - \varepsilon^2})^2}{(x - \varepsilon)^2 + (\sqrt{1 - x^2} + \sqrt{1 - \varepsilon^2})^2} \right) d\varepsilon dx \quad (\text{A.3})$$

$$G_{dydx} = \int_{-1}^1 x \int_{-1}^1 \frac{\partial y}{\partial X} \ln \left(\frac{(x - \varepsilon)^2 + (\sqrt{1 - x^2} - \sqrt{1 - \varepsilon^2})^2}{(x - \varepsilon)^2 + (\sqrt{1 - x^2} + \sqrt{1 - \varepsilon^2})^2} \right) d\varepsilon dx \quad (\text{A.4})$$

$$H_y = -2 \int_{-1}^1 y \frac{\sqrt{1 - \varepsilon^2}}{\varepsilon - 1} d\varepsilon \quad (\text{A.5})$$

$$H_{dydx} = -2 \int_{-1}^1 \frac{\partial y}{\partial x} \frac{\sqrt{1 - \varepsilon^2}}{\varepsilon - 1} d\varepsilon \quad (\text{A.6})$$

where ε and x are non-dimensional variables. Whereas, y and X have dimensions.

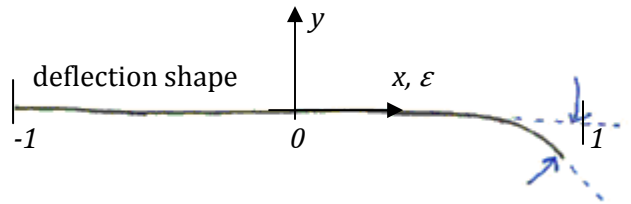


FIGURE A.1 TRAILING EDGE FLAP SHAPE.

APPENDIX B: C_M COMPARISON

This Appendix shows a comparison between the original implementation of the C_M model from Andersen et al [21] and the corrected one shown in Equation (10).

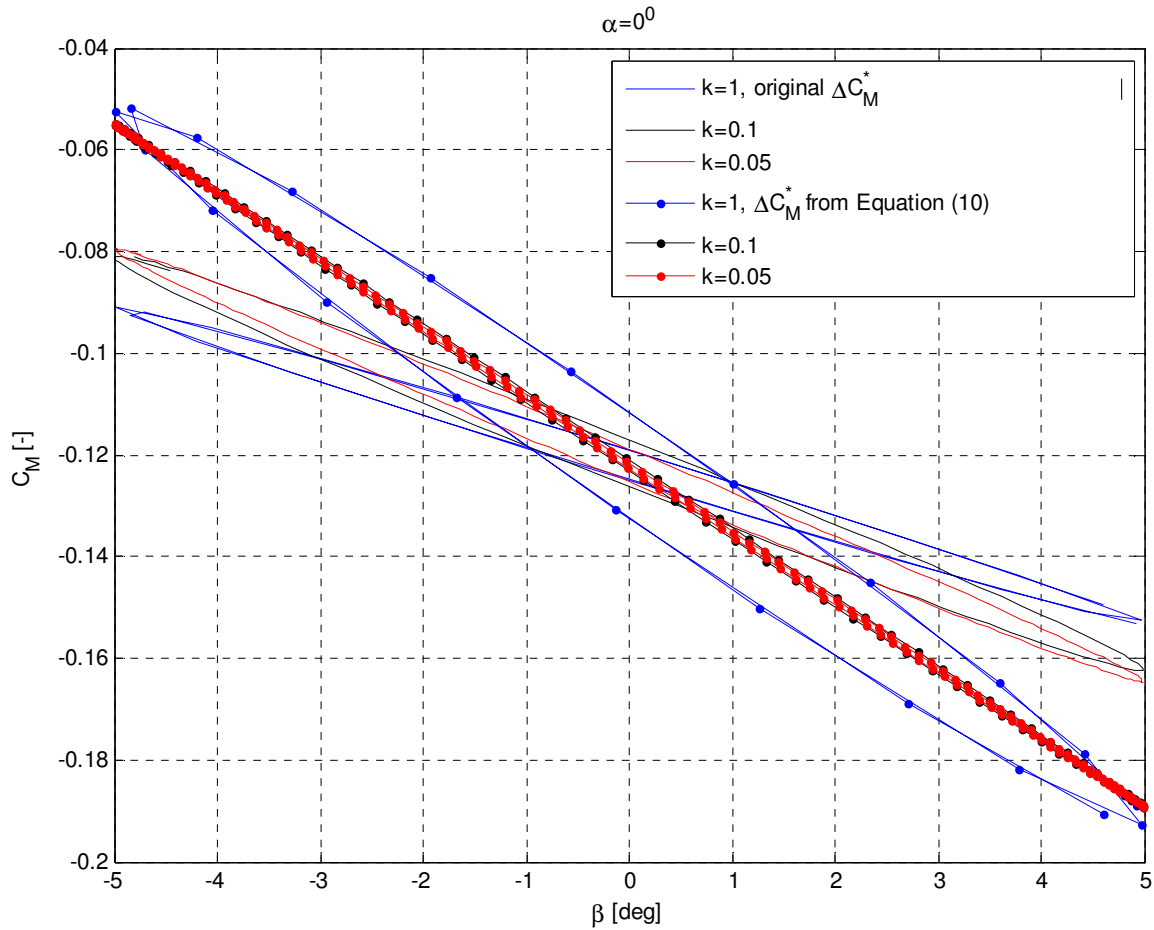


FIGURE B.1 C_M LOOPS COMPARED FOR DIFFERENT REDUCED FREQUENCIES AT ZERO INCIDENCE. THE ORIGINAL VERSION IS ANDERSEN ET AL [21] WHICH HAVE BEEN COMPARED WITH EQUATION (10).

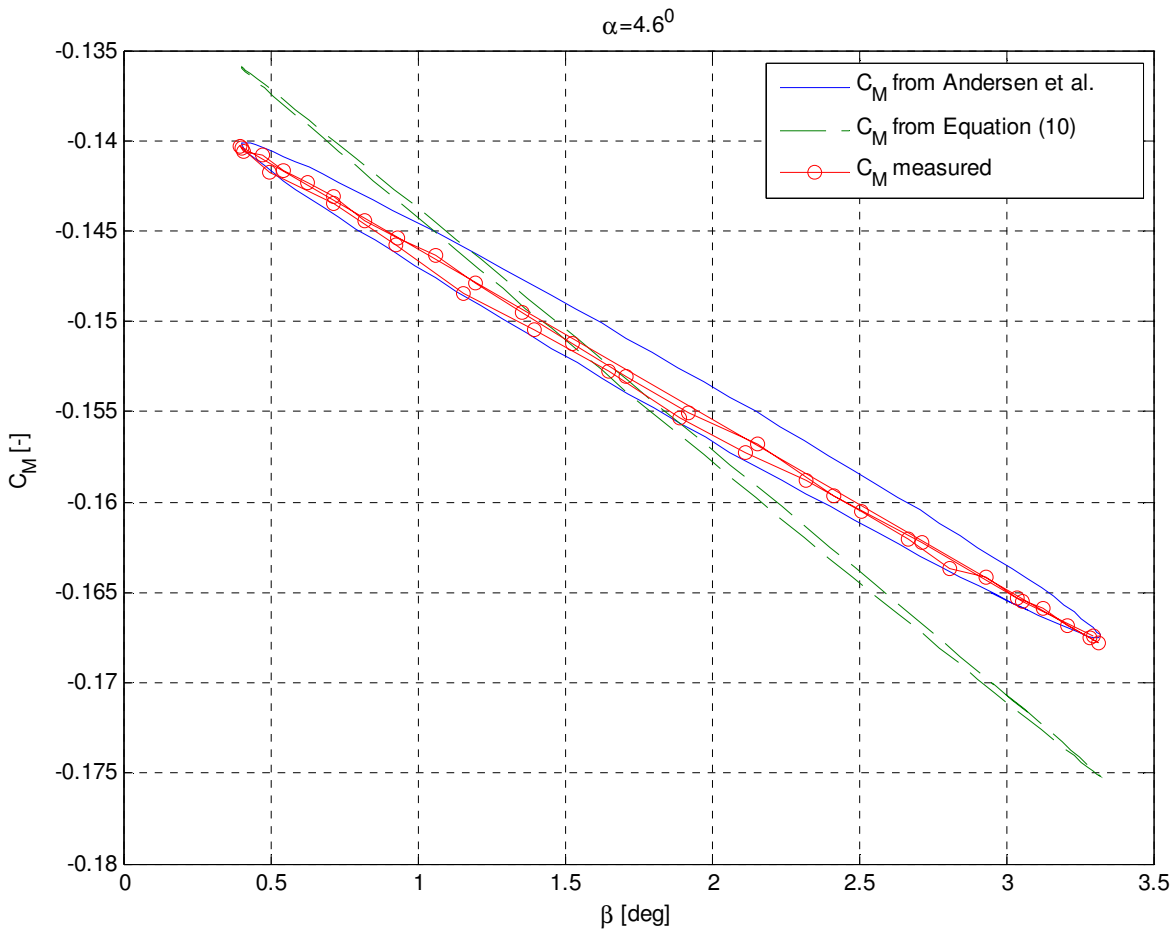


FIGURE B.2 C_M FOR THE TWO MODELS COMPARED WITH MEASUREMENTS. THE ORIGINAL VERSION IS ANDERSEN ET AL [21] (BLUE LINE) WHICH HAVE BEEN COMPARED TO EQUATION (10) (GREEN LINE).

The measured values are assumed to under predict the change in moment due lack of pressure sensors near the trailing edge flap. Recent unpublished CFD calculations have shown that the area near the trailing edge has an increased suction hump when flapping downwards which gives an increase in the moment (and vice versa). This would explain why the measured values do not come closer to the calculated C_M values using Equation (10).

APPENDIX C: WIND TUNNEL SETUP DRAWINGS AND PHOTOS

The VELUX wind tunnel is of the closed return type with an open test section with a cross section of 7.5×7.5 m and a length of 10.5 m, Figure C.1. The cross section of the jet blowing into the test section is 3.4×3.4 m. The maximum flow velocity is 42 m/s.

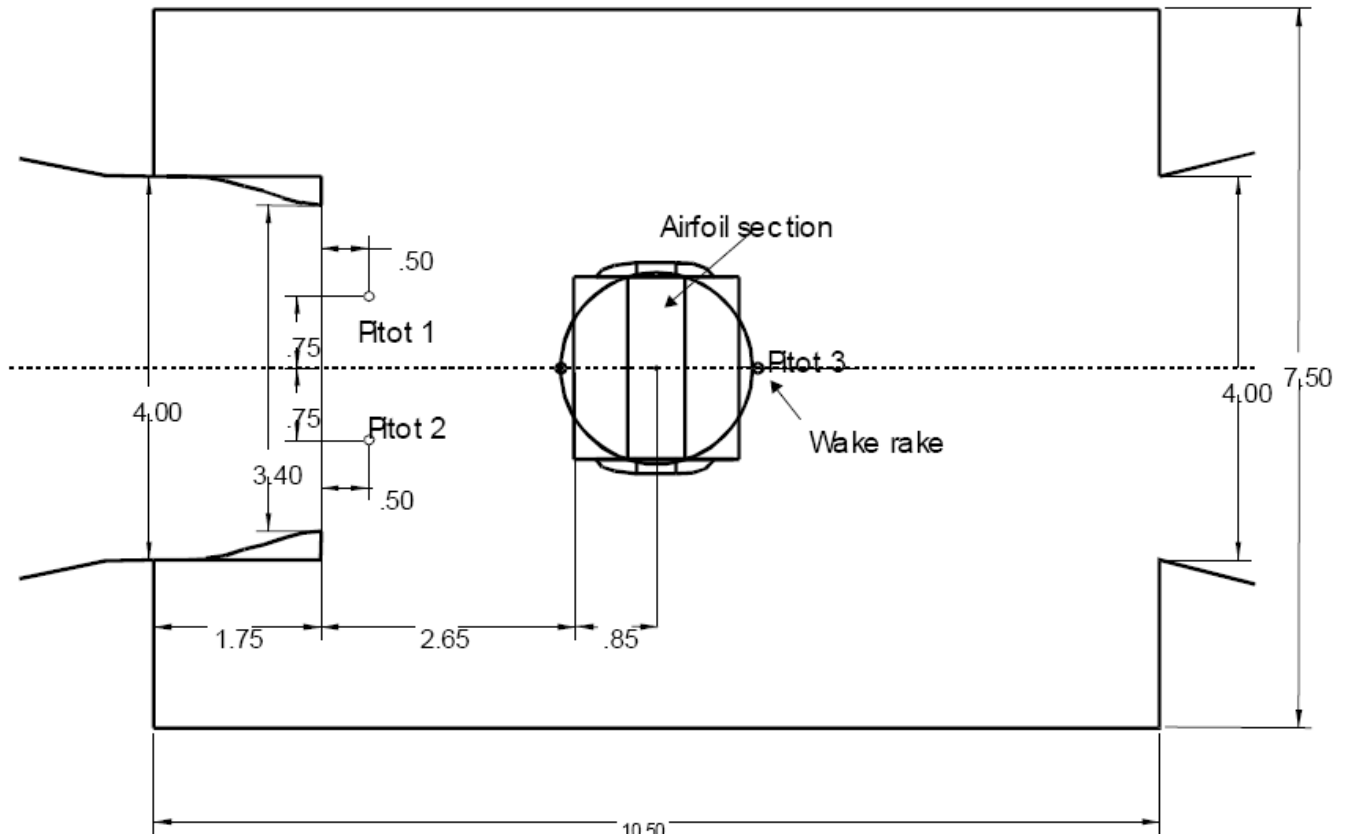


FIGURE C.1 THE WIND TUNNEL TEST SECTION WITH THE TEST STAND SEEN IN A TOP VIEW WITH THE FLOW COMING FROM THE LEFT.



FIGURE C.2 THE TEST SECTION WITH THE TEST STAND AND THE WAKE RAKE DOWNSTREAM OF THE AIRFOIL SECTION.

The wake rake consisted of 53 total pressure probes and five static tubes. The vertical span was 0.456 m, Figure C.2. The distance between the airfoil trailing edge and the wake rake was 0.7 airfoil chords and the centre of the wake rake was placed at the height of the trailing edge at 0° incidence and behind the centre line of the airfoil section.

The controller uses four separate pressure taps organized in a 2x2 taps system, 2 taps are mounted on the airfoil at 12% and 2 other taps at 50% illustrated in Figure C.3.

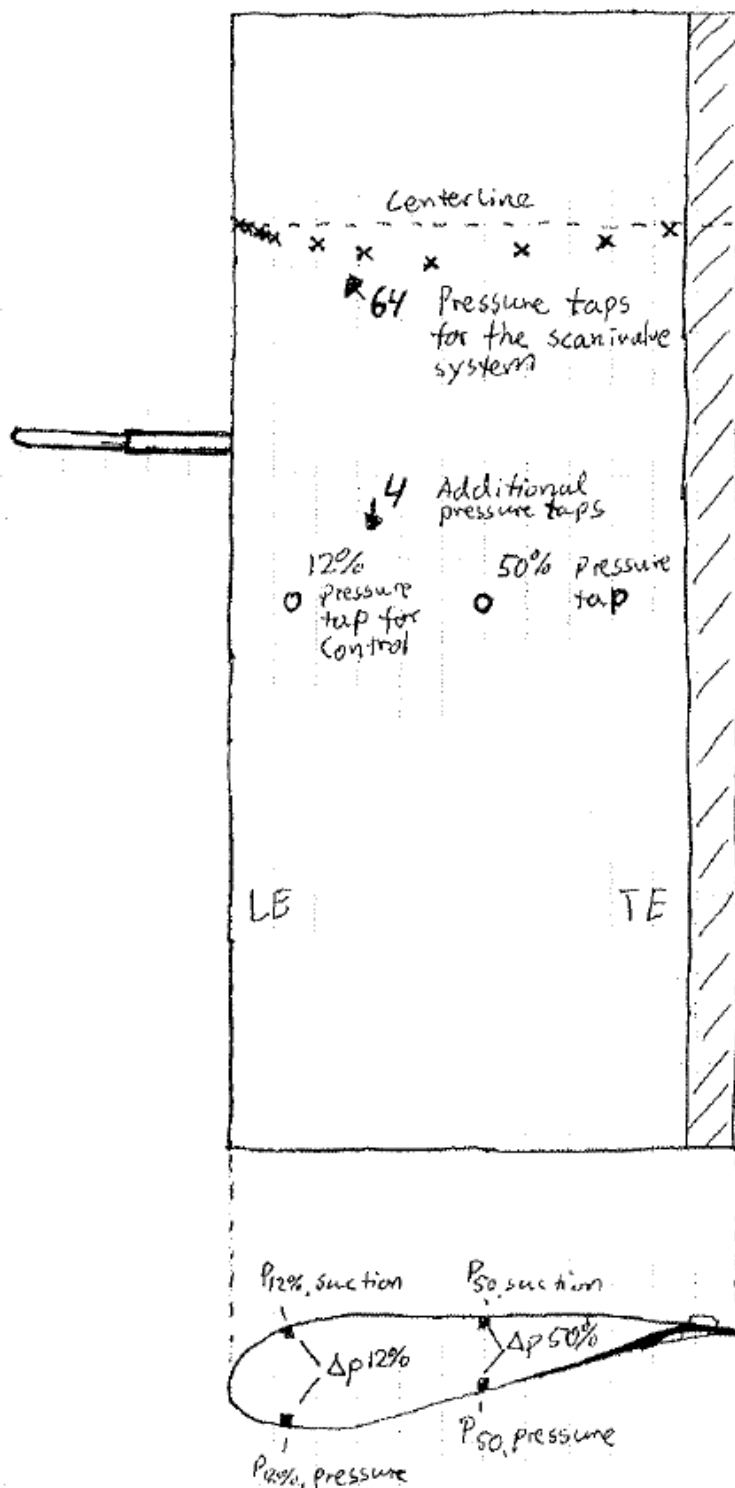


FIGURE C.3 ILLUSTRATES 64 PRESSURE TAPS USED TO INTEGRATE LIFT ACCURATELY USING THE SCANIVALVE SYSTEM AND THE 4 PRESSURE TAPS ORGANIZED 2 BY 2 AT 12% AND 50% USED TO APPROXIMATE LIFT, THE TWO PRESSURE TAPS AT 12% IS FURTHERMORE USED BY THE CONTROL ALGORITHM.

APPENDIX D: STRAIN GAUGE SENSOR PLACEMENT ON AIRFOIL

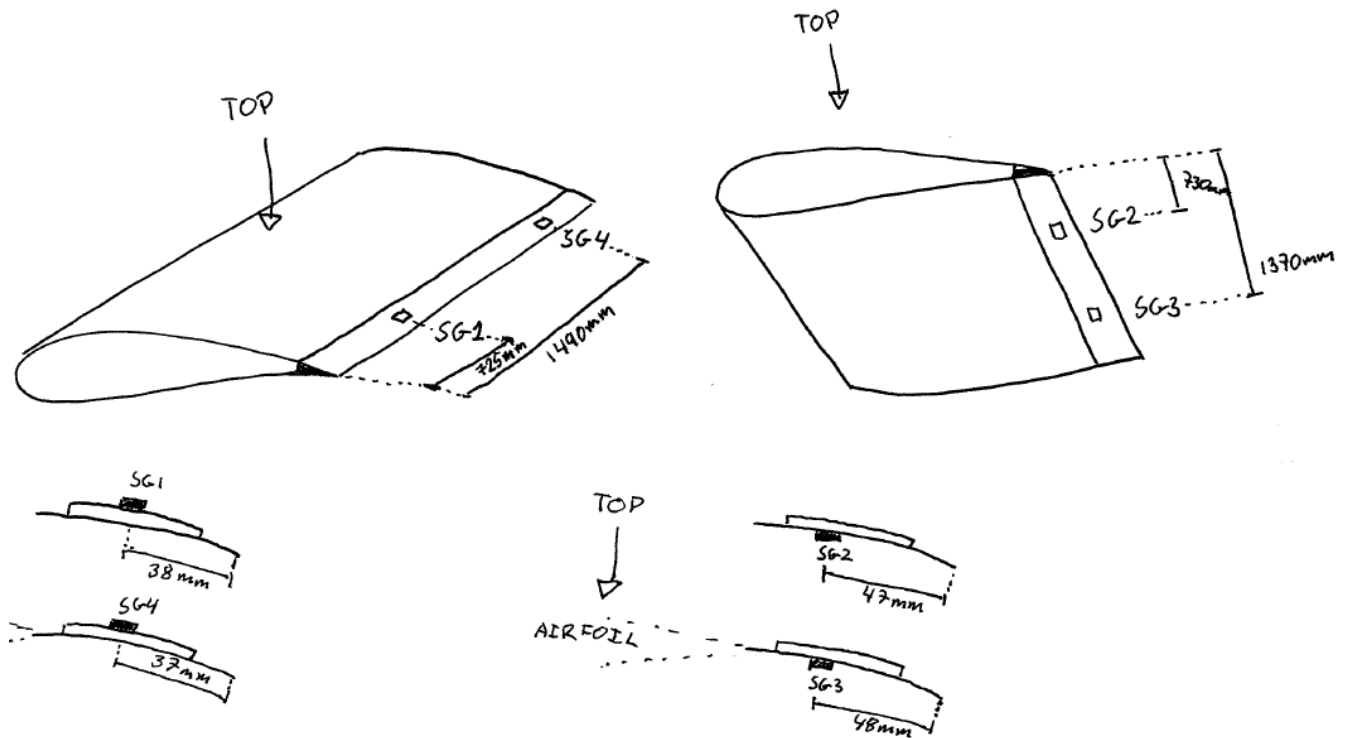


FIGURE D.1 ILLUSTRATES STRAIN GAUGE ONE TO FOUR AND WHERE THEY ARE PLACED ON THE TRAILING EDGE FLAP OF THE RISOE B1-18 AIRFOIL TEST SECTION. "TOP" INDICATES SUCTION SIDE AT NORMAL ATTACHED FLOW INCIDENCES.

BIBLIOGRAPHY

1. BOSSANYI, E. A.; ***Developments in Individual Blade Pitch Control***. Wind Energy, Vol. 6 issue 3, p. 229-244, 2003.
2. LARSEN, T. J.; MADSEN, H. A.; THOMSEN, K.; ***Active Load Reduction Using Individual Pitch, Based on Local Blade Flow Measurements***. Wind Energy, Vol. 8 issue 1, p. 67-80, 2004.
3. LIANGA, Y.; TAYAA, M.; KUGAB, Y.; ***Design of diaphragm actuator based on ferromagnetic shape memory alloy composite***. Proceedings Vol. 5054. Smart Structures and Materials: Industrial and Commercial Applications of Smart Structures Technologies, p. 45-52, 2003.
4. YEN, D. T.; VAN DAM, C. P.; SMITH, R. L.; COLLINS, S. D.; ***Active Load Control for Airfoils Using Microtabs***. Journal of Solar Energy Engineering, 2001, Vol. 123, No. 4, p. 282-289, 2002.
5. VAN DAM, C. P.; CHOW, R.; ZAYAS J.R.; BERG D. A.; ***Computational investigation of small deploying tabs and flaps for aerodynamic load control***. Journal of Physics, Conference series: The Science of Making Torque from Wind. **75** (012027). 2007.
6. STUART, J. G.; WRIGHT, A. D.; BUTTERFIELD, C. P.; ***Considerations for an Integrated Wind Turbine Controls Capability at the National Wind Technology Center: An Aileron Control Case Study for Power Regulation and Load Mitigation***. AWEA Windpower. Denver, Colorado 1996. p. 13.
7. VAN DAM, C. P.; CHOW, R.; ZAYAS, J. R.; BERG, D. E.; ***Computational Investigations of Small Deploying Tabs and Flaps for Aerodynamic Load Control***. The Science of Making Torque from the Wind. Lyngby, Denmark: J. Phys.: Conf. Series, Vol. 75, No.1. August 2007.
8. KERHO, M.; HUTCHERSON, S.; BLACKWELDER, R. F.; LIEBECK, R. H. ***Vortex Generators used to Control Laminar Separation Bubbles***. Journal of Aircraft, Vol. 30, No. 3, p. 315-9, 1993.
9. MOREAU, E.; BENARD, N.; JOLIBOIS, M.; TOUCHARD, G.; ***Airflow Control by Plasma Actuators: Last Significant Results at the University of Poitiers***. 2nd European Conference for Aerospace Sciences. 2007.
10. BASUALDO, S.; ***Load alleviation on wind turbine blades using variable airfoil geometry***. Wind Engineering, vol. 29, no. 2, 2005.
11. TROLDBORG, N.; ***Computational study of the Risø-B1-18 airfoil with a hinged flap providing variable trailing edge geometry***. Wind Engineering, vol. 29, no. 2, 2005.
12. BAK, C.; GAUNAA, M.; ANDERSEN, P. B.; BUHL, T. HANSEN P.; CLEMMENSEN, K.; ***Wind tunnel test on wind turbine airfoil with adaptive trailing edge geometry***. 45. AIAA aerospace sciences meeting and exhibit. Reno, NV (US): 2007.

13. BUHL, T.; GAUNAA, M.; BAK, C.; **Potential Load Reduction Using Airfoils with Variable Trailing Edge Geometry.** Journal of Solar Energy Engineering, Vol. 127, p. 503-516, November 2005.
14. BUHL, T.; BAK, C.; GAUNAA, M.; ANDERSEN, P. B.; **Load alleviation through adaptive trailing edge control surfaces: ADAPWING overview.** European Wind Energy Conference and Exhibition. Milan (IT) 2007. p. 23.
15. MADSEN, H. A.; BUHL, T.; NA, L.; ANDERSEN, P. B.; BAK, C.; GAUNAA, M.; HANSEN, M. H. **Design and test of a controllable rubber trailing edge flap.** 2009 European Wind Energy Conference and Exhibition. Marseille (FR),: EWEC 2009 Proceedings online, p. 1 page EWEC, 2009. 16-19 Mar, 2009.
16. BARLAS, T.K.; KUIK, G.A.M.; **State of the art and prospectives of smart rotor control for wind turbines.** The Science of Making Torque from the Wind. Lyngby, Denmark: J. Phys.: Conf. Series, Vol. 75, No.1. August 2007.
17. LACKNER, M.A.; KUIK, G.A.M.; **A Comparison of Smart Rotor Control Approaches using Trailing Edge Flaps and Individual Pitch Control.** 47rd AIAA Aerospace Sciences Meeting and Exhibit. Orlando, Florida, NV: AIAA Paper 2009-685. 2009.
18. MATTHEW, A.L.; KUIK, G.A.M.; **The Performance of Wind Turbine Smart Rotor Control Approaches During Extreme Loads,** J. Sol. Energy Eng. 132, 011008 p.8. 2010.
19. WINGERDEN, J. W. V.; **Control of Wind Turbines with 'Smart' Rotors: Proof of Concept & LPV Subspace Identification.** 2008. PhD Thesis. 147 p. ISBN: 978-90-9023583-7.
20. VOUSINAS, S.; RIZIOTIS V.; **Aeroelastic Modelling of The Active Flap Concept For Load Control.** European Wind Energy Conference and Exhibition. Brussels (BE): 2008.
21. ANDERSEN, P. B.; GAUNAA, M.; BAK, C.; HANSEN, M. H.; **A Dynamic Stall Model for Airfoils with Deformable Trailing Edges.** Wind Energy, 2009; **12**: 734-751
22. ANDERSEN, P. B.; GAUNAA, M.; HENRIKSEN, L. C.; BAK, C.; BUHL, T.; **Deformable Trailing Edge Flaps for Modern Mega-Watt Wind Turbine Controllers using Strain Gauge Sensors.** Accepted for publication Wind Energy. p.28.
23. ANDERSEN, P. B.; GAUNAA, M.; BAK, C.; BUHL, T.; HANSEN, P.; ENEVOLDSEN, K. M.; **Wind tunnel test on wind turbine airfoil with closed loop controller for adaptive trailing edge flap.** Risø report. Technical Report. Risø-R-1707(En)

24. BAK, C.; JOHANSEN, J.; ANDERSEN, P. B.; ***Three-dimensional corrections of airfoil characteristics based on pressure distributions.*** European Wind Energy Conference and Exhibition. Athens (GR): 27 Feb - 2 Mar 2006. p. 10.
25. LARSEN, T. J.; HANSEN, A. M.; ***How 2 HAWC2, the user's manual.*** Technical Report. Risø-R-1597(ver. 3-1)(EN). 4000 Roskilde:. 2007. p. 70.
26. ANDERSEN, P. B.; GAUNAA, M.; MADSEN, H. A.; ***A Near Wake Model with Far Wake Effects Implemented in a Multi Body Aero-Servo-Elastic Code.*** Submitted for publication in Wind Energy.
27. THEODORSEN, T. ***General Theory of Aerodynamic Instability and The Mechanism of Flutter.*** NACA Report 496, p. 413-433, 1935.
28. BAK, C.; ANDERSEN, P. B.; MADSEN, A. H.; GAUNAA, M.; FUGLSANG, P.; BOVE, S.; ***Design and verification of airfoils resistant to surface contamination and turbulence intensity.*** 26. AIAA applied aerodynamics conference. Honolulu, HI (US): 18-21 Aug, 2008.
29. GAUNAA, M.; ***Unsteady 2D Potential-flow Forces on a Thin Variable Geometry Airfoil Undergoing Arbitrary Motion.*** Accepted for publication in 'Smart Rotor' special issue Wind Energy.
30. HANSEN, M. H.; GAUNAA, M.; MADSEN, H. A.; ***A Beddoes-Leishman type dynamic stall model in state-space and indicial formulations.*** Technical report. Risø-R-1354, Risø, June 2004.
31. LEISHMAN, J. G.; BEDDOES, T. S.; ***A Generalized Model for Airfoil Unsteady Aerodynamic Behavior and Dynamic Stall Using Indicial Method.*** Proceedings of the 42nd Annual Forum of the American Helicopter Society, Washington D.C, June 1986.
32. KARMAN, T. V.; SEARS, W. R.; ***Airfoil Theory for Non-Uniform Motion.*** Journal of the Aeronautical Sciences, Vol. 5. No. 10, p. 379-390, 1938.
33. JONES, R. T.; ***The Unsteady Lift of a Wing of Finite Aspect Ratio.*** Tech. Rep. 681, NACA Report, 1940.
34. KIRCHHOFF, G.; ***Incompressible Aerodynamics.*** Cambridge University Press, 1961.
35. SNEL, H. S.; ***Survey of induction dynamics modeling within BEM-like codes. Dynamic inflow and yawed flow modeling revisited.*** 20th 2001 ASME Wind Energy Symposium. AIAA Paper 2001-0027.
36. SCHEPERS, J. G.; SNEL, H.; ***Dynamic inflow: yawed conditions and partial span pitch control.*** Technical Report. ECN-C—95-056. 2005.

37. MADSEN, H. A.; RASMUSSEN, F.; ***A Near Wake Model for Trailing Vorticity Compared with the Blade Element Momentum Theory.*** Wind Energy 2004;7:325-341.
38. BEDDOES, T. S.; ***A near wake dynamic model.*** Aerodynamics and Aeroacoustics National Specialist Meeting. 1987. p. 1-9.
39. SØRENSEN, N. N.; MADSEN, H. A.; ***Modelling of transient wind turbine loads during pitch motion.*** European Wind Energy Conference and Exhibition. Athens (GR): 27 Feb -2 Mar 2006.
40. WANG, T.; COTON, F. N.; ***A modified near wake dynamic model for rotor analysis.*** The Aeronautical Journal. 1999. p. 143-146.
41. DANTZIG, G.B.; ***Linear Programming and Extensions.*** Princeton, NJ (Princeton University Press), ISBN: 0-691-08000-3, 1963.
42. HANSEN, M. O. L.; ***Aerodynamics of Wind Turbines.*** James James (Science Publishers) Ltd, ISBN: 1-902916-06-9, 1999.
43. MICHELSEN J. A.; ***Basis3D—a platform for development of multiblock PDE solvers.*** Technical Report AFM 92-05, Technical University of Denmark, 1992.
44. MICHELSEN J. A.; ***Block structured multigrid solution of 2D and 3D elliptic PDEs.*** Technical Report AFM 94-06, Technical University of Denmark, 1994.
45. SØRENSEN N. N.; ***General purpose flow solver applied to flow over hills.*** Technical Report Risø-R-827(EN), Risoe National Laboratory, 1995.
46. VOUTSINAS, S. G.; ***Vortex Methods in Aeronautics: How to make things work.*** Int. Journal of Computational Fluid Dynamics, Vol 20. 2006.
47. HENRIKSEN, L. C.; ***Model predictive control of a wind turbine.*** Master thesis, Technical University of Denmark. DK-2800 Lyngby: 2007.
48. HENRIKSEN, L. C.; ***Model predictive control of a wind turbine with constraints.*** European Wind Energy Conference. Brussels (BE): 2008.
49. ANDERSEN, P. B.; GAUNAA, M.; BAK, C.; BUHL, T.; ***Load alleviation on wind turbine blades using variable airfoil geometry.*** European Wind Energy Conference and Exhibition. Athens (GR): 2006. p. 8.
50. ANDERSEN, P. B.; HENRIKSEN, L. C.; GAUNAA, M.; BAK, C.; BUHL, T.; ***Integrating deformable trailing edge geometry in modern Mega-Watt wind turbine controllers.*** European Wind Energy Conference and Exhibition. Brussels (BE): 2008. p. 15-21.

51. MARKOU, H.; ANDERSEN, P. B.; LARSEN, G.; **Potential of Trailing Edges Flaps Exposed To Wakes Emitted from Upstream Modern Mega-Watt Turbines. Euromech Colloquium.** Madrid (ES): October 2009.
52. GAUNAA, M.; ANDERSEN, P. B.; **Load reduction using pressure difference on airfoil for control of trailing edge flaps.** European Wind Energy Conference and Exhibition. Marseille (FR): 16-19 Mar, 2009. p. 10.
53. JONKMAN, J.; BUTTERFIELD, S.; MUSIAL, W.; SCOTT, G.; **Definition of a 5-MW Reference Wind Turbine for Offshore System Development.** Technical Report NREL/TP-500-38060 Feb. 2009.
54. MATSUISKI, M.; ENDO, T.; **Fatigue of metals subjected to varying stress,** Japan Soc. Mech. Engineering. 1969.
55. PALMGREN, A.; **Durability of Ball Bearings.** ZVDI, Vol. 68, No. 14, pp. 339-341. 1924.
56. MINER, M. A.; **Cumulative Damage in Fatigue.** Journal of Applied Mechanics, Vol. 12, Trans. ASME Vol. 67, pp. A159-A164. 1945.
57. WÖHLER, A.; **Theorie rechteckiger eiserner Brückenbalken mit Gitterwänden und mit Blechwänden,** Zeitschrift für Bauwesen vol. 5 pp121-166. 1855.
58. JONKMAN, J.; BUTTERFIELD, S.; MUSIAL, W.; SCOTT, G.; **Definition of a 5-MW Reference Wind Turbine for Offshore System Development.** 2009.
59. ANDERSEN, P. B.; **Load alleviation on wind turbine blades using variable airfoil geometry (2D and 3D study).** M.Sc. thesis. Technical University of Denmark. MEK-DTU 2800 Lyngby. 2005.
60. HEINZ, J.; **Investigation of Piezoelectric Flaps for Load Alleviation Using CFD.** Risø-R-1702(EN), Risø DTU National Laboratory, 2009
61. MCFADDEN, N. M.; RATHERT, G. A.; BRAY, R. S.; **Flight calibration of angles of attack and sideslip detectors on the fuselage of a 350 swept wing fighter aircraft.** NASA RMA52A04, p. 26, 1952.
62. HANSEN, M. H.; HANSEN, A.; LARSEN, T. J.; ØYE, S.; SØRENSEN, P.; FUGLSANG, P.; **Control design for a pitch-regulated, variable speed wind turbine.** Technical Report. Risø-R-1500(EN). 4000 Roskilde: Januar 2005.
63. BUHL, T.; ANDERSEN, P. B.; **Deformable trailing edge geometries and cyclic pitch controller.** Sandia National Laboratories 20008 wind turbine blade workshop. Presented at: Albuquerque (US): 12-14 May, 2008.

64. MADSEN, H. A.; MIKKELSEN, R.; SØRENSEN, N. N.; HANSEN, M.O.L.; ØYE, S.; JOHANSEN, J.; ***Influence of wind shear on rotor aerodynamics, power and loads.*** part of: Research in aeroelasticity EFP-2006. Technical Report. Risø-R-1611(EN), pages: 101-116, 2007
65. BUHL, T.; GAUNAA, M.; ANDERSEN, P. B.; ***Stability limits for a full wind turbine equipped with trailing edge systems.*** European Wind Energy Conference and Exhibition. Marseille (FR): 16-19 Mar, 2009. p. 48-52.
66. MADSEN, H. A.; LARSEN, G. C.; LARSEN, T. J.; TROLDBORG, N.; ***Calibration and validation of the Dynamic Wake Meandering model implemented in the aeroelastic code HAWC2.*** Journal of Solar Energy Engineering, p. 31, July 2009.
67. FRANDBSEN, S.; ***Turbulence and turbulence generated structural loading in wind turbine clusters.*** Technical Report. Risø-R-1188(EN). 2003.
68. IEC61400-1, E. 3. C. 2. R.; ***Wind Turbines. Part 1: Design requirements.*** 2004.
69. MADSEN, H. A.; LARSEN, G. C.; LARSEN, T. J.; ***Wake deficit- and turbulence simulated with two models compared with inflow measurements on a 2MW turbine in wake conditions.*** Scientific proceedings, p. 48-53-Brussels (2008): European Wind Energy Conference and Exhibition.
70. LARSEN, G. C.; MADSEN, H. A.; THOMSEN, K.; LARSEN, T. J.; ***Wake meandering - a pragmatic approach.*** Wind Energy 2008; vol. 11: p.377–395.
71. AINSLIE, J. F.; ***Calculating the flow field in the wake of wind turbines.*** J. Wind Eng. Ind. Aerodyn. 27 (1988), p. 213–224.
72. MARKOU, H.; ANDERSEN, P. B.; LARSEN, G.; ***Potential Load Reduction on Megawatt Turbines Exposed to Wakes using Individual Pitch Wake Compensator and Trailing Edge Flaps*** (to be submitted)
73. LARSEN, T. J.; HANSEN, A. M.; ***Influence of Blade Pitch Loads by Large Blade Deflections and Pitch Actuator Dynamics Using the New Aeroelastic Code HAWC2.*** EWEC. Athens (GR): 2006.
74. GAUNAA, M.; FUGLSANG, P.; BAK, C.; ANTONIOU, I.; ***Open-Jet Wind Tunnel Validation and Measurements on a NACA 0012 Airfoil.*** Technical Report. Risø-R-1460(EN), Risø National Laboratory, Roskilde, Denmark, 2005.
75. FUGLSANG, P.; ANTONIOU, I.; SØRENSEN, N. N.; MADSEN, H. A.; ***Validation of a Wind Tunnel Testing Facility for Blade Surface Pressure Measurements.*** Technical Report. Risø-R-981(EN), Risø National Laboratory, Denmark, 1998.

76. BUHL, T.; GAUNAA, M.; BAK, C., HANSEN, P.; ***Measurements on the Thunder TH-6R actuator.*** Technical Report. Risø-R-1537(EN). Risø National Laboratory, November 2005.
77. ANDERSEN, P. B.; GAUNAA, M.; BAK, C.; HANSEN, M. H.; ***Implementing a dynamic stall model for airfoils with deformable trailing edges.*** AIAA aerospace sciences meeting and exhibit. Reno (US): 7-10 Jan, 2008.
78. BROWN, E. N.; FRIEHE, C. A.; LENSCHOW, D. H.; ***The Use of Pressure Fluctuations on the Nose of an Aircraft for Measuring Air Motion.*** Research Aviation Facility, National Center for Atmospheric Research. Boulder, CO 80307: April, 1982.
79. BUHL, T.; ANDERSEN, P. B.; BARLAS, T. K.; ***2D numerical comparison of trailing edge flaps.*** Technical Report. Risø-R-1628(EN). ISSN: 0106-2840. ISBN 978-87-550-3647-5. p. 20. 2007.

PHD THESIS SUMMARY:

ADVANCED LOAD ALLEVIATION FOR WIND TURBINES USING ADAPTIVE TRAILING EDGE FLAPS: SENSING AND CONTROL

Peter Bjørn Andersen
PhD. student
Risø DTU, Wind Energy Department

This dissertation compiles the work carried out during the past three years of my PhD. The trailing edge flap applied to wind turbine blades was researched. The deformable trailing edge flaps was analyzed both experimentally and numerically through series of aeroelastic simulations. The conclusion of the studies suggested that adding deformable trailing edge flaps onto wind turbine blades can alleviate fluctuating loads much. The deformable trailing edge flap concept has been found to work both experimentally for 2D wind tunnel experiments and also in 3D aeroelastic simulations. Different combinations of control sensors and controllers were investigated both experimentally and through simulations. Significant load reduction is seen for the investigated combinations of sensors and controllers. Furthermore, to facilitate the numerical simulations aerodynamic models for the deformable trailing edge flap had to be developed.

AVANCERET LAST REDUKTION FOR VINDMØLLER VED BRUG AF ADAPTIVE BAGKANT FLAPPER: SENSORERING OG KONTROL

Peter Bjørn Andersen
PhD. student
Risø DTU, Wind Energy Department

Denne afhandling samler det arbejde jeg har lavet over de sidste tre år i forbindelse med min Ph.d. Bagkant flapper monteret på vindmølle vinger er undersøgt. Den deformerbare bagkant flap blev analyseret både eksperimentelt og numerisk ved at bruge aeroelastiske simuleringer. Konklusionen af mit studie er at man kan fjerne de fluktuerede og ofte skadelige laster ved brug af bagkant flapper på vindmølle vinger. Bagkant konceptet virker både eksperimentelt for 2D vindtunnel målinger og i 3D aeroelastiske simuleringer. Forskellige kombinationer af kontrol sensorer og kontrol algoritmer er blevet undersøgt. Store last reduktioner er set for de undersøgte kombinationer af sensorer og kontrol algoritmer. Ydermere er der blevet udviklet aerodynamiske modeller til den deformerbare bagkant.

Risø DTU is the National Laboratory for Sustainable Energy. Our research focuses on development of energy technologies and systems with minimal effect on climate, and contributes to innovation, education and policy. Risø has large experimental facilities and interdisciplinary research environments, and includes the national centre for nuclear technologies.

Risø DTU
National Laboratory for Sustainable Energy
Technical University of Denmark

Frederiksborgvej 399
PO Box 49
DK-4000 Roskilde
Denmark
Phone +45 4677 4677
Fax +45 4677 5688

www.risoe.dtu.dk